Computational Frameworks for Probabilistic Performance-Based Wind Assessment of Envelope Systems of Engineered Buildings

by

Zhicheng Ouyang

A dissertation submitted in partial fulfillment
of the requirements for the degree of
Doctor of Philosophy
(Civil Engineering and Scientific Computing)
in the University of Michigan
2021

Doctoral Committee:

Associate Professor Seymour M.J. Spence, Chair
Professor Seth Guikema
Associate Professor Jason P. McCormick
Associate Professor Jeff Scruggs

Zhicheng Ouyang

ouyangzc@umich.edu

ORCID iD: 0000-0001-6722-2685

This dissertation is dedicated to my parents, my sister and my friends who understood and supported me on the long and winding road towards a PhD.

ACKNOWLEDGEMENTS

This study was financially supported by the National Science Foundation (NSF). This support is gratefully acknowledged.

I would like to express my sincere gratitude to Prof. Seymour Spence for his guidance at every stage of the process, his continuous encouragement to overcome challenges, and most importantly his understanding for me to explore different disciplines and pursue an industry career. I would like to express my gratitude to Prof. Jason McCormick, Prof. Jeffrey Scruggs, and Prof. Seth Guikema for their support and advice in completing this work. I would like to thank Dr. Arthriya Subgranon, Dr. Wei-Chu Chuang, Ahmed Abdelhady, Bowei Li, Srinivasan Arunachalam, Dr. Jason Martinez, and Alyssa Desimone for all the kind help and happiness they have given me since I joined the lab. I would also like to thank Prof. Jeff Scruggs and Prof. Jason P. McCormick again for advising me during my graduate study and recommending me into the PhD program. In addition, I would like to thank my family and my friends for their constant companionship and encouragement over the past few years.

TABLE OF CONTENTS

LIST OF FIGURES

Figure

LIST OF TABLES

Table

ABSTRACT

The adoption of performance-based wind engineering (PBWE) is rapidly becoming recognized as a fundamental step to reducing the economic losses induced by severe windstorms. A number of PBWE frameworks for the assessment of engineered building systems such as high-rise structures have been introduced. Although these frameworks have resulted in significant progress toward the efficient and effective estimation of performance within a PBWE setting, there is still a significant lack of frameworks that can holistically model the performance of the envelope systems of engineered buildings, notwithstanding how these systems are often critical to the overall performance of engineered buildings. The lack of research on this topic is mainly due to the high complexity of modeling the interdependent physical processes leading to damage. These processes include the 3D turbulent wind flow, wind-driven-rain and rainwater runoff, flying debris, internal/external wind pressures, structural dynamic responses, story drift/net pressure-induced envelope damages, debris impact-induced damages, and water ingress. As analytical solutions do not exist for this type of problem, efficient computational frameworks must be developed. To address this situation, this research presents a performance-based wind engineering framework that integrates system-level structure and envelope performance assessment. In particular, the external surface pressure is generated through a wind tunnel-enabled proper orthogonal decomposition (POD)-based non-Gaussian simulation framework while the stochastic internal pressures at envelope openings are modeled through a nonlinear coupled system of equations derived through the application of the unsteady-isentropic form of the Bernoulli equation and the principle of mass conservation. Linear modal analysis or high-fidelity nonlinear finite element methods (FEM) are used in modeling the dynamic structural responses as well as any subsequent damage. To predict the

envelope component damage, suites of coupled fragility functions are derived to account for the effect of multiple demands acting simultaneously. As a concurrent hazard event, wind-driven rain is modeled in a separate computational fluid dynamics (CFD) domain where the mean wind flow is solved through a 3D Reynolds-averaged Navier-Stokes (RANS) equation with realizable k-epsilon model. Based on this mean wind flow, the wind-driven rain is solved through an Eulerian-multiphase model with turbulent dispersion considered. For efficiently estimating probabilistic performance metrics in terms of the total repair cost and amount of water ingress, the framework is further integrated into a conditional stochastic simulation framework where the uncertainties in the hazard inputs, such as wind speed, stochasticity of the aerodynamic loads, wind direction, and rainfall intensity are propagated to the system responses. Finally, the effect of the hazard duration on the performance metrics is investigated. In this respect, in place of the classic assumption of a nominal wind and rain hazard of 1-hour duration, a synthetic tropical cyclone approach is adopted in which the entire duration of the hurricane is simulated resulting in time-varying inputs of wind speed, wind direction, and rainfall intensity. A comprehensive comparison, in terms of a full range of probabilistic performance metrics, is carried out illustrating the limitations of current practice.

CHAPTER I

Introduction

1.1 Motivation and overview

From the post-hazard survey of extreme wind events, such as hurricanes and tropical storms, the majority of losses to engineered building systems are due to building envelope damages that lead to the exposure of the interior systems to wind and rain, therefore triggering further interior damages. Despite the fundamental role played by the envelope system in dictating the performance of engineered buildings, there is a significant lack of research on frameworks and models that can assess the performance of this system. Indeed, existing PBWE frameworks for assessing damages and losses are mainly focused on the structural system. However, current PBWE research is advancing towards more holistic approaches, where high fidelity damage and loss analysis of envelope system is required. To this end, the development of frameworks for assessing the envelope performance of engineered buildings during extreme wind events is the focus of this research. A brief overview of these areas is presented below.

1.1.1 Performance-based wind engineering

Over the last two decades, a significant amount of research has been focused on the implementation of PBWE for the assessment of engineered building systems (e.g. high-rise buildings) (e.g. *Jain et al.*, 2001; *Ciampoli et al.*, 2011; *Smith and Caracoglia*, 2011; *Petrini,*

F. and Ciampoli, M., 2012; *Chuang and Spence*, 2017; *Cui and Caracoglia*, 2018; *Zheng et al.*, 2019; *Cui and Caracoglia*, 2020; *Petrini et al.*, 2020). Although the importance of damage to the building envelope of engineered systems due to local actions has been documented (e.g. *Pita et al.*, 2012; *Barbato et al.*, 2013; *Baheru et al.*, 2015), the majority of the work in this area has focused on describing performance in terms of the response of the structural system. Other aspects that are generally ignored are the damage and losses generated by the action of local wind pressures, the water ingress, and debris impact. Therefore, the next step towards a more holistic PBWE approach is the development of frameworks that can assess envelope system performance in terms of potential damage and loss due to the site-specific actions of wind, rain, and debris.

1.1.2 Damage mechanisms associated with building envelopes

The risk sources associated with the envelope system can be divided into three types: wind-generated turbulent pressure over the building surface, wind-borne debris flying nearby the building location, and wind-driven rain impinging the building envelope. These sources of risk have the potential to induce damage to the envelope components, and subsequent losses, through the actions of dynamic internal and external wind pressure, dynamic structural responses, debris impact, and rainwater ingress (e.g. *Kareem*, 1986; *Minor*, 2005; *Baheru et al.*, 2015; *Minor*, 1994). Among these actions, significant interaction exists, e.g. dynamic external/internal pressure coupling at the envelope openings, structural/pressure response induced envelope openings, and building specific wind flow altered trajectories of debris and rain (e.g. *Quirouette and Arch*, 2004; *Lin et al.*, 2007; *Choi*, 1993; *Kubilay et al.*, 2013). The presence of multiple actions, or demands, on the envelope components, lead to complex damage mechanisms where coupling effects in the accumulation of damage must be considered due to the often simultaneous application of these actions.

1.2 Research objective

The primary goal of this research is to develop high-fidelity computational frameworks for estimating the performance of envelope systems of engineered buildings within the setting of PBWE. The major objectives are the following:

Objective I: A damage estimation framework for building envelopes of wind-excited structures. Development of an efficient simulation-based framework to model the progressive damage to envelope components during severe wind events that explicitly accounts for damage-coupling due to the simultaneous and interdependent action of dynamic structural responses and internal/external pressures.

Objective II: A nonlinear dynamic analysis framework for structural and envelope damages subjected to hurricane winds. Development of a high-fidelity framework to estimate structural and envelope damages caused by extreme winds through nonlinear structural dynamic analysis carried out within a fiber-based finite element formulation.

Objective III: A water ingress estimation framework for engineered buildings subjected to extreme wind and rain. Development of a computational fluid dynamics (CFD)-enabled computational framework to estimate the stochastic water ingress process through damaged envelope components during extreme wind and concurrent rain events.

Objective IV: A PBWE framework for building envelope systems subjected to directional wind and rain. Development of a computational framework to estimate building envelope performance in terms of total repair costs and volume of water ingress during extreme wind and rain events that are characterized through a joint probabilistic hazard model.

Objective V: A PBWE framework for building envelope systems subjected

to synthetic tropical cyclones. Investigation into the effects on building envelope performance of wind and rain event evolution through the integration of the PBWE framework of Objective IV with synthetic tropical cyclone wind and rain simulation models.

1.3 Organization of the dissertation

In accordance with the University of Michigan's doctoral degree requirements, this dissertation is presented as a series of journal papers. The papers comprising chapters 2-5 are first-authored by the candidate and co-authored by Dr. Seymour M.J. Spence. The dissertation is organized as follows.

Chapter 2 [1] presents a computational framework that can holistically treat multiple damage mechanisms during the performance assessment of building envelopes of wind-excited engineered systems. In particular, interdependent envelope damage states driven by dynamic internal/external wind pressures and structural responses are modeled through multiple dependent fragility functions. Consequences are modeled in terms of the envelope components' final damage states as well as the ingress of wind-driven rain. By setting the framework in a simulation environment, probabilistic estimates of the performance metrics are provided as output. A full-scale application is also presented illustrating the proposed framework.

Chapter 3 [2] presents a PBWE framework focused on the performance assessment of the envelope system. This framework is based on integrating the building envelope damage framework of Chapter 2 into a conditional stochastic simulation framework in which the directional wind and concurrent rain hazard are explicitly modeled together with the stochastic nature of the local wind pressure. By incorporating loss models, performance estimates are

[1] Ouyang, Z., & Spence, S. M. (2019). A performance-based damage estimation framework for the building envelope of wind-excited engineered structures. *Journal of Wind Engineering and Industrial Aerodynamics, 186*, 139-154.

[2] Ouyang, Z., & Spence, S. M. (2020).A Performance-Based Wind Engineering Framework for Envelope Systems of Engineered Buildings Subject to Directional Wind and Rain Hazards. *Journal of Structural Engineering, 146*, 04020049.

provided in terms of annual exceedance rates of system-level metrics such as repair cost. The practicability of the proposed PBWE framework is illustrated through a full-scale archetype building example.

Chapter 4 [3] presents work that fills the knowledge gap concerning the relative severity, dependency, and rate of occurrence of structural and envelope damage in extreme wind events. In particular, envelope damage is estimated through the PBWE framework presented in Chapter 2. Structural damage is estimated through both fragility analysis and as well as material yielding/hysteresis modeled through the adoption of a nonlinear fiber-based finite element formulation. Structural responses include the effects of large deformations through solving the finite element model in a corotational environment. To investigate the relative severity and dependency between the damages, a carefully calibrated archetype 45-story steel building located in Miami, FL, and subject to hurricane winds is studied. Probabilistic damage metrics are estimated for both the envelope and structural systems.

Chapter 5 [4] investigates the effects of hurricane event duration on the envelope performance through the integration of the PBWE framework of Chapter 4 with models that characterize the full evolution of wind and rain fields during tropical cyclones. In particular, synthetic tropical cyclone models are used to probabilistically model both the expected horizontal rainfall intensity and storm track with associated wind field, therefore providing continuously varying probabilistically consistent records of wind speed, wind direction, and expected rainfall intensity over the lifetime of the tropical cyclone. To simulate the full evolution of the hurricane induced aerodynamic loads, a computational framework for simulating the non-stationary/-straight/-Gaussian wind pressure processes was developed. Through the implementation of a set of computational models and a novel conditional stochastic simulation algorithm, the probabilistic distributions associated with water ingress and total repair cost

[3] Ouyang, Z., & Spence, S. M. (2021).Performance-based wind-induced structural and envelope damage assessment of engineered buildings through nonlinear dynamic analysis. *Journal of Wind Engineering and Industrial Aerodynamics, 208*, 104452.

[4] Ouyang, Z., & Spence, S. M. (2021). A Performance-Based Wind Engineering Framework for Engineered Structures subject to Hurricanes. Draft manuscript submitted for publication.

are generated. To generate insightful comparisons, a carefully calibrated full-scale archetype building located in Miami, FL was studied. Performance results are compared with those obtained from current state-of-the-art wind engineering practice in which nominal one-hour wind/rain events are used in estimating building performance.

Finally, Chapter 6 presents the general summary and conclusions, together with key findings and future research directions in the area of performance-based assessment of engineered buildings.

CHAPTER II

A Performance-Based Damage Estimation Framework for the Building Envelope of Wind-Excited Engineered Structures[1]

Abstract

The performance assessment of wind-excited multi-story building systems is undergoing a period of rapid change with a number of performance assessment frameworks being proposed that are based on the principles of performance-based design. Having said this, there is still a significant lack of computational frameworks that can holistically treat the building envelope of this class of building systems. Indeed, the majority of research in this direction has focused on estimating damages and losses due to excessive structural response, notwithstanding the important role played by other damage mechanisms, such as those driven by excessive dynamic pressures. This paper introduces a computational framework that can holistically treat multiple damage mechanisms during the performance assessment of building envelopes of wind-excited engineered systems. In particular, interdependent envelope damage states driven by dynamic internal/external wind pressures and structural responses are modeled through multiple dependent fragility functions. Consequences are modeled in

[1]Ouyang, Z., & Spence, S. M. (2019). A performance-based damage estimation framework for the building envelope of wind-excited engineered structures. *Journal of Wind Engineering and Industrial Aerodynamics, 186*, 139-154.

terms of the envelope components' final damage states as well as the ingress of wind driven rain. By setting the framework in a simulation environment, probabilistic estimates of the performance metrics are provided as output. A full scale application is presented illustrating the proposed framework.

2.1 Introduction

Recent trends in the performance assessment of wind-excited building systems have seen the introduction of a number of frameworks based on the principles of performance-based design (PBD). In particular, methodologies for both engineered structures (e.g. *Ciampoli et al.*, 2011; *Smith and Caracoglia*, 2011; *Seo and Caracoglia*, 2013; *Bernardini et al.*, 2013; *Caracoglia*, 2014; *Bernardini et al.*, 2015; *Chuang and Spence*, 2017; *Cui and Caracoglia*, 2018), as well as residential buildings (e.g. *Barbato et al.*, 2013; *Pita et al.*, 2012; *Unnikrishnan and Barbato*, 2016) have been proposed. While for low-rise residential buildings the important role played by the building envelope in dictating performance is well understood (*Pita et al.*, 2012; *Barbato et al.*, 2013; *Baheru et al.*, 2015), the same cannot be said for engineered structures, e.g. multistory buildings. For these systems, with the exception of the recent extension of the Florida Public Hurricane Loss Model (FPHLM) to high-rise residential buildings (*Pita et al.*, 2016), the focus has been primarily on describing damage and losses due to excessive structural response (e.g. peak inter-story drifts or floor accelerations). However, there is a growing realization that the performance of engineered structures during severe wind events, such as hurricanes, can only be fully achieved through the development of holistic frameworks that model not only damage due to excessive structural response, but also damage to the building envelope due to excessive internal/external pressures, wind borne debris impact, as well as the subsequent ingress of wind driven rain, which can lead to significant damage to the internal components of the building system. The main challenge in developing such a framework can be traced back to the complexity of the physical phenomena leading to damage (e.g. wake induced turbulent external wind pressure fields, dynamic

internal pressures, wind flow dispersed impinging rain fields, and the dynamic response of the structural system) as well as the interdependency of the various damage mechanisms (e.g. envelope damage at one point will in general lead to significant internal pressure changes at other points of the building envelope, potentially leading to a progressive damage mechanism). If it is also recognized that significant uncertainty will inevitably affect the capacity of the system to withstand the aforementioned damage mechanisms, as well as the intensity of the external wind, rain and wind borne debris hazards, then the need to treat the problem in a probabilistic setting is clear.

This work is focused on the development of a framework that can begin to tackle this problem within a data-driven computational environment. Attention is placed on modeling the performance of the envelop system while considering damage driven by the dynamic response of the structural system to wind tunnel estimated time history loading and the dynamic internal and external wind pressures (with the extension to wind borne debris damage a natural progression). Ingress of wind driven rain through the building envelope is modeled through computational fluid dynamics (CFD) and treated as a consequence of the dynamic pressure/response induced damages. To model the multiple damage states of each envelope component, the concept of fragility (*Moehle and Deierlein*, 2004; *Yang et al.*, 2009; *Federal Emergency Management Agency (FEMA)*, 2012a) is adopted with discussion on approaches for modeling the interdependencies between damage states originating from different failure mechanisms. For estimating the effects of uncertainty, which inevitably exists in describing the system, a Monte Carlo simulation framework is outlined.

2.2 The problem setting

Recent advances in the performance-based assessment of wind-excited buildings are centered on the use of fragility functions for probabilistically modeling the multiple damage states that each building component can assume given a demand level. Mathematically, fragility, F_{DS_j}, can be defined as the conditional probability of assuming a damage state DS_j

conditional on a value of an engineering demand parameter (edp):

$$F_{DS^j}(edp) = P(DS^j|edp) \quad \text{for} \quad j = 1, ..., N_{edp} \tag{2.1}$$

where in writing Eq. (2.1) it has been recognized that for a given component, e.g. cladding element, and demand, e.g. dynamic internal/external wind pressures, N_{edp} possible damage states will exist for a given demand parameter. Equation (2.1) represents the definition of fragility assumed in modern performance-based seismic engineering frameworks (*Moehle and Deierlein*, 2004; *Yang et al.*, 2009; *Federal Emergency Management Agency (FEMA)*, 2012a), as well as in their recent extensions to wind engineering (*Chuang and Spence*, 2017). In this work, this definition is adopted for describing the susceptibility of each component of a building envelope to damage induced by excessive dynamic internal/external wind pressures and structural responses. In particular, while in applying Eq. (2.1) to seismic engineering problems each component can be considered dependent on a single demand parameter edp (*Yang et al.*, 2009; *Federal Emergency Management Agency (FEMA)*, 2012a), the same cannot be assumed in the damage assessment of envelope systems of wind-excited structures, for which multiple sets of possible damage states (i.e. fragility functions) will exist, with each set associated with a different engineering demand parameter, e.g. internal/external pressures and peak drifts. In general, and as illustrated in Fig. 2.1, interdependencies will also exist between each set of damage states. For example, the occurrence of a drift induced damage state is likely to affect the probability of occurrence of a pressure induced damage state and vice versa. In general, there will also exist coupling between the damage states and the demand parameters, i.e. the edps. For example, the occurrence of damage to an envelope component will in general lead to air infiltration that will affect the dynamic internal pressures therefore changing the net pressure demand on the envelope component as well as any nearby envelope components. This interdependency between demands and damage states, as well as between the sets of fragility functions associated with a given component, leads to a time dependent problem. In other words, the final damage state of a given envelope component can only be

determined by simulating over, i.e. time stepping through, the entire windstorm. Indeed, only by following an approach of this type will the interdependencies outlined above be fully modeled and the progressive nature of wind driven damage be captured.

This work is focused on developing a data-driven computational framework for solving the problem outlined above and schematically represented in Fig. 2.1. The framework is based on combining wind tunnel data for modeling the external dynamic wind loads and pressure coefficients with CFD models for estimating the wind driven rain impacting the building envelope. This combined approach enables established experimental approaches to be used to characterize the external wind loads and pressures, together with CFD models for the estimation of the wind driven rain which have been carefully validated on full scale data collected on both low- and high-rise structures (*Kubilay et al.*, 2013, 2014, 2015b,a). This gives confidence to the applicability of the proposed framework to problems of practical interest. It should also be observed that, in alternative to CFD, the wind driven rain could also be estimated directly from specialized wind tunnel tests, e.g. (*Baheru et al.*, 2014b,a). By developing a Monte Carlo simulation framework around the model, probabilistic estimation of the performance is enabled, as is the probabilistic deaggregation of the results.

2.3 Demand and damage models for consequence estimation

This section introduces the set of models that will be used in the probabilistic damage estimation model of Sec. 2.4. In defining these models, it is assumed that: 1) all the structure–fluid interactions have negligible aeroelastic effects; and 2) all the fluid–fluid interactions (i.e. air flow/rain phase interactions) present a one-way air flow to rain phase coupling. With respect to the second point, this implies that, in all air flow/rain phase interactions, the dynamics of the wind flow will influence the dynamics of wind driven rain but not vice versa. This assumption is reasonable, as the volume of the rain phase is negligible compared with the volume of the air, even in the case of a severe windstorm, in which case the volumetric ratio of rain to air is below 10^{-2} (*Kubilay et al.*, 2015a). With a further

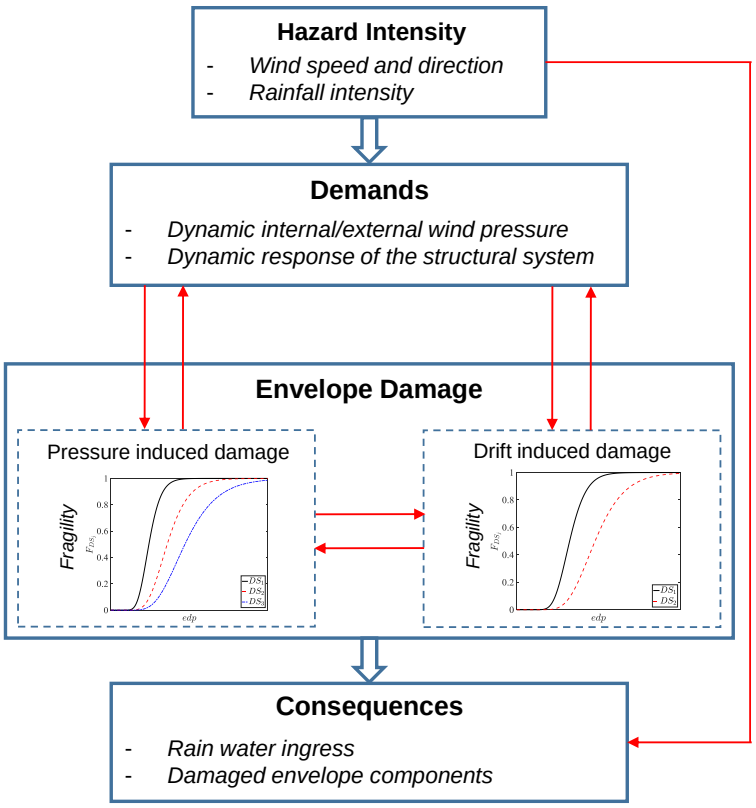

Figure 2.1: Schematic representation of the interdependencies that exist between the different damage states and demands in the performance estimation of an envelope system of a wind-excited structure.

assumption that the transient load on the building due to the impinging rain is negligible, then, given consistent boundary conditions (i.e. consistent mean wind speed profiles over the height of the building), the simulation of the dynamic response of the building system can be decoupled from the simulation of the wind driven rain. This decoupling enables the simulation of the dynamic response of the structural system to the external wind pressures to be carried out independently from the simulation of the wind driven rain field surrounding the building.

Under the assumptions outlined above, the following models can be used to estimate the demands, damages, and consequences following the interactions identified in Sec. 2.2 and illustrated in Fig. 2.1.

2.3.1 Structural response model

As outlined above, in the presence of negligible aeroelastic and impinging rain loads, the dynamic response of the structural system can be directly solved in terms of the external aerodynamic loads $\mathbf{f}$, and therefore through solving the following equations of motion:

$$\mathbf{M}\ddot{\mathbf{x}}(t) + \mathbf{C}\dot{\mathbf{x}}(t) + \mathbf{K}\mathbf{x}(t) = \mathbf{f}(t, \bar{V}_H, \alpha) \tag{2.2}$$

where: $\mathbf{M}$, $\mathbf{C}$, and $\mathbf{K}$ are the mass, damping and stiffness matrices respectively; $\mathbf{x}(t)$, $\dot{\mathbf{x}}(t)$, and $\ddot{\mathbf{x}}(t)$ are the displacement, velocity and acceleration response vectors; while $\mathbf{f}(t, \bar{V}_H, \alpha)$ is the vector of external aerodynamic loads evaluated for a mean wind speed at the building top of $\bar{V}_H$ and wind direction α. In writing Eq. (2.2), it has been assumed that the structural system responds elastically to the wind loads $\mathbf{f}(t)$, as, in general, life safety design requirements for high-rise structures require an essentially elastic response of the structural system under extreme wind events, e.g. 1700- to 3000-year events. However, it should be observed that all the following developments are not limited to this assumption. Therefore, Eq. (2.2) can be directly replaced by a fully non-linear system of equations.

Instead of directly solving Eq. (2.2), it is computationally far more convenient to find the

solutions to Eq. (2.2) by solving the following associated modal equations:

$$\ddot{q}_i(t) + 2\omega_i \xi_i \dot{q}_i(t) + \omega_i^2 q_i(t) = Q_i(t, \bar{V}_H, \alpha) \tag{2.3}$$

where ω_i, $\boldsymbol{\phi}_i$ and ξ_i are the circular frequency, mode shape, and damping ratio of the ith vibration mode, $q_i(t)$, $\dot{q}_i(t)$, and $\ddot{q}_i(t)$ are the displacement, velocity and acceleration responses of the ith mode, while $Q_i(t)$ is the generalized force of the ith mode given by:

$$Q_i(t, \bar{V}_H, \alpha) = \frac{\boldsymbol{\phi}_i{}^T}{\boldsymbol{\phi}_i{}^T \mathbf{M} \boldsymbol{\phi}_i} \mathbf{f}(t, \bar{V}_H, \alpha) \tag{2.4}$$

Once solutions to the first N_m modal equations are found, the dynamic response of the building system can then be estimated in physical coordinates as:

$$\mathbf{x}(t) \approx \sum_{i=1}^{N_m} \boldsymbol{\phi}_i \, q_i(t) \tag{2.5}$$

where the approximation in Eq. (2.5) is due solely to modal truncation. In particular, the N_m independent modal equations can be solved extremely efficiently in the time domain through the use of digital filters (*Spence and Kareem*, 2013; *Spence et al.*, 2016).

From the knowledge of $\mathbf{x}(t)$, any displacement response of interest, Dr, can be directly estimated as:

$$Dr(t) = \boldsymbol{\Lambda}_{Dr}^T \mathbf{x}(t) \tag{2.6}$$

where $\boldsymbol{\Lambda}_{Dr}$ is a vector of constants extracting the displacement (or combination of displacements, e.g. inter-story drift) of interest.

2.3.1.1 Dynamic wind loads

To solve Eq. (2.3), and therefore Eq. (2.2), estimates of the aerodynamic loads $\mathbf{f}$ are required. To ensure an adequate description of the typically complex aerodynamic response of the multi-story structures of interest to this work (e.g. acrosswind wake-induced vortex

shedding), wind tunnel data consisting of synchronously measured external pressures, associated with a mean wind speed profile modeling the boundary layer for the terrain conditions of interest, are considered for characterizing $\mathbf{f}$. Following this approach, the dynamic external pressure coefficients at K points of a rigid scale model of the building are measured in a wind tunnel test. Through an appropriate interpolation/extrapolation scheme, this set of modal scale pressure coefficients can be used to estimate dynamic external pressure coefficients at full scale as:

$$C_{p,e}(t;\boldsymbol{\zeta}) = \Gamma[C_{p,e}^{(1)}(t_w), ..., C_{p,e}^{(K)}(t_w); \boldsymbol{\zeta}] \text{ for } \boldsymbol{\zeta} \in E \tag{2.7}$$

where $C_{p,e}^{(k)}$ for $k = 1, ..., K$ are the wind tunnel estimated dynamic external pressure coefficients, Γ is an appropriate interpolation function with extrapolation to the edges of the building envelope (e.g. a cubic spline interpolation of the points $C_{p,e}^{(k)}(t_w)$ with linear extrapolation), $\boldsymbol{\zeta}$ is a coordinate pair identifying the point of interest on the surface E (i.e. a point of interest of the building envelope), while t_w and t are the wind tunnel and scaled times that are related by (similitude of the Strouhal number):

$$t = \left(\frac{\bar{V}_{H_w} L_p}{\bar{V}_H L_w}\right) t_w \tag{2.8}$$

where L_w is the characteristic length at wind tunnel scale, L_p is the corresponding length at full scale, $\bar{V}_{H_w}$ is the wind speed in the wind tunnel at the top of the model, while $\bar{V}_H$ is the wind speed at which the full scale performance assessment will occur.

Equation (2.7) provides an estimate of the dynamic external pressure coefficients at any point on the building envelope, and can therefore be used to estimate the dynamic external pressure field as:

$$p(t;\boldsymbol{\zeta}) = \frac{1}{2}\rho \bar{V}_H^2 C_{p,e}(t;\boldsymbol{\zeta}) \tag{2.9}$$

where ρ is the density of air. From Eq. (2.9), the aerodynamic wind loads $\mathbf{f}(t, \bar{V}_H, \alpha)$ can be estimated by integrating $p(t;\boldsymbol{\zeta})$ over the tributary area associated with each degree of freedom of the structural system.

2.3.2 Aerodynamic models

2.3.2.1 Wind pressure

Each envelope component will be subject to the net pressure p_n, i.e. the difference between the external and internal pressure, acting across the component:

$$p_n(t) = \frac{1}{2}\rho \bar{V}_H^2 \left[\bar{C}_{p,e}(t) - C_{p,i}(t)\right] \tag{2.10}$$

where, to estimate p_n, not only are the mean (i.e. averaged over the area of the envelope component) time varying external pressure coefficient $\bar{C}_{p,e}(t)$ required, but also the time varying internal pressure coefficients $C_{p,i}(t)$. While $\bar{C}_{p,e}(t)$ can be estimated by averaging $C_p(t;\boldsymbol{\zeta})$ over the area of the component of interest, the estimation of $C_{p,i}(t)$ requires a dynamic internal pressure model that can be updated if the number of external envelope openings change (i.e. due to damage) during the wind event.

To accomplish this, a dynamic internal pressure model suitable for general envelope shapes and composition of internal compartments is here proposed. In developing the model, it is assumed that the opening size is small as compared to the dimensions of the rigid internal space, thus the internal air can be considered as stagnant even though air is flowing through the openings. Under this assumption, a general building can be schematized as a system of $\mathcal{N}_i$ rigid interconnected air spaces which are excited by the external pressure field through $\mathcal{N}_e$ potential openings in the building envelope, which are evolving in time due to damage. Figure 2.2 illustrates the situation for a simple floor plan composed of $\mathcal{N}_i = 4$ compartments, internally connected through three openings and potentially excited by $\mathcal{N}_e = 6$ damageable envelope components. By describing the transient air flow at each opening (including the internal openings) through the unsteady-isentropic form of the Bernoulli equation (*Vickery and Bloxham*, 1992; *Guha et al.*, 2011; *Yu et al.*, 2008), the transient internal pressure variation can be estimated from the principle of mass conservation. This leads to the following system of non-linear and coupled equations that can be solved for the unknown vector of

internal pressure coefficients $\mathbf{C}_{p,i}(t) = \{C_{p,i}^{(1)}(t), ..., C_{p,i}^{(\mathcal{N}_i)}(t)\}^T$:

$$\dot{\mathbf{V}}_f(t) = \frac{1}{2}\mathcal{I}[V_H^2 \mathbf{\Theta} \mathbf{C}_p(t) - \mathbf{C}_L |\hat{\mathbf{V}}_f(t)| \mathbf{V}_f(t)] \tag{2.11}$$

$$\dot{\mathbf{C}}_{p,i}(t) = \mathbf{\Delta}^{-1} \mathbf{\Upsilon}_w \mathcal{A}_w(t) \mathbf{V}_f(t) \tag{2.12}$$

where: $\mathcal{I}$ is a diagonal matrix with kth diagonal term:

$$\mathcal{I}_{k,k} = \begin{cases} C_I^{-1}\sqrt{A_{w,k}(t)}, & \text{if } A_{w,k}(t) > 0 \\ 0, & \text{otherwise} \end{cases} \tag{2.13}$$

with C_I an inertia coefficient, and $A_{w,k}(t)$ the time varying areas of the kth opening which are also collected in the diagonal matrix $\mathcal{A}_w(t)$; $\mathbf{C}_L$ is the diagonal matrix collecting the loss coefficients of the air slugs of each opening; $\hat{\mathbf{V}}_f$ the diagonal matrix collecting the air velocities through each opening with $\mathbf{V}_f$ their vector; $\mathbf{\Delta}$ is a diagonal matrix collecting the volume of each internal compartment; $\mathbf{\Theta}$ is a connectivity matrix that identifies the nominal external and internal pressure coefficients for each opening; $\mathbf{C}_p(t)$ is the vector collecting both the external and internal pressure coefficients; while $\mathbf{\Upsilon}_w$ is given by:

$$\mathbf{\Upsilon}_w = -\frac{2\gamma P_a}{\rho V_H^2} \mathbf{\Theta}_i^T \tag{2.14}$$

where γ is the specific heart ratio for air (i.e 1.4), P_a is the barometric pressure (i.e 101300 Pa), and $\mathbf{\Theta}_i$ is the submatrix of $\mathbf{\Theta}$ associated with the unknown internal pressure coefficients.

To solve the nonlinear and coupled system of Eqs. (2.11)–(2.12) while accounting for how the damage state of each envelope component can vary during the evolution of the windstorm, numerical methods are required. In this work, the explicit Runge-Kutta method with 4th order accuracy is adopted due to its stability and computational efficiency.

If the building is considered enclosed, e.g. before any damage is considered to have

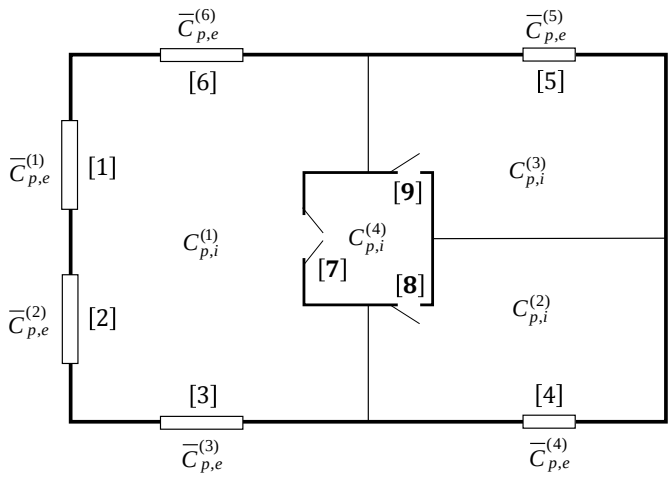

Figure 2.2: Illustration of the internal pressure model for a system with $\mathcal{N}_i = 4$ compartments, three internal openings and $\mathcal{N}_e = 6$ potential openings to the exterior of the building through the building envelope.

occurred to the building envelope, then the internal pressure coefficients are assumed to follow a normal distribution with mean:

$$\mu_{C_{p,i}} = -0.15 + 0.3\frac{A^+}{A} \tag{2.15}$$

where A^+ is the exposure area with positive mean pressure while A is the total exposed area of the building envelope, and standard deviation of 0.05 (*Ellingwood and Tekie*, 1999). The initial internal pressure is simplified to be statically maintained until a window becomes open, then the dynamic internal pressure model is implemented.

2.3.2.2 Wind Driven Rain

One of the more important consequences of building envelope damage is the potential for water ingress, as many severe wind events are accompanied by a concurrent rain event that can cause significant amounts of water to impact the building envelope and therefore enter the building through any drift/pressure induced breaches. To estimate the amount of water ingressed, a wind driven rain (WDR) model is required for translating the horizontal rainfall intensity, R_h, into impinging rain on the building envelope. In this work, a steady-state

Eulerian multiphase model with turbulent dispersion (*Choi*, 1994; *Blocken and Carmeliet*, 2002, 2007; *Kubilay et al.*, 2013) is considered. The choice to consider a steady state model with turbulent dispersion, as opposed to a fully transient simulation (e.g. *Huang and Li*, 2012), for the WDR was made in light of how the consequence of interest to this work is the total water ingressed at each breach in the building envelope over the duration of the event. Therefore, any transient effects in the WDR will tend to be averaged out in calculating the consequences.

Governing equations In a multiphase setting, rain is decomposed into N phases, with the kth phase defined by raindrops with diameter d in the interval $[d_k-(\Delta d/2), d_k+(\Delta d/2)]$ with Δd the diameter range and $k = 1, ..., N$. The volume fraction of the kth phase is indicated with α_k and represents the fraction of the totality of rain drops in $[d_k-(\Delta d/2), d_k+(\Delta d/2)]$. The distribution of raindrops over all phases will in general depend on the rainfall intensity R_h and is here modeled through the widely adopted distribution proposed by *Best* (1950):

$$f_h(d, R_h) = n \left(\frac{d}{a(R_h)}\right)^{n-1} \exp\left[-\left(\frac{d}{a(R_h)}\right)^{n}\right] \tag{2.16}$$

where $a = A(R_h)^p$ with A, p, and n constants with expected values 1.30, 0.232, and 2.25 respectively.

As outlined in (*Kubilay et al.*, 2015a; *Huang and Li*, 2010), under these conditions, the governing equations for each incompressible rain phase can be written in terms of the equations of mass and momentum conservation as:

$$\frac{\partial(\alpha_k \bar{u}_{k,j})}{\partial x_j} + \frac{\partial \alpha_k}{\partial t} = 0 \tag{2.17}$$

$$\begin{aligned} \frac{\partial(\alpha_k \bar{u}_{k,i})}{\partial t} + \frac{\partial(\alpha_k \bar{u}_{k,i} \bar{u}_{k,j})}{\partial x_j} + \frac{\partial(\alpha_k \overline{u'_{k,i} u'_{k,j}})}{\partial x_j} = \\ \alpha_k g + \alpha_k \frac{3\mu_a}{\rho_w d^2} \frac{C_d Re_R}{4} (\bar{u}_i - \bar{u}_{k,i}) \end{aligned} \tag{2.18}$$

where $\bar{u}_{k,i}$ is the steady-state (i.e. time averaged) velocity of the kth rain phase in the ith direction, $\bar{u}_i$ is the steady-state velocity of the air phase in the ith direction, g is the gravitational acceleration, μ_a is the dynamic air viscosity, ρ_w is the density of water, C_d is the drag coefficient, Re_R the Reynolds number relative to the wind flow, while $\overline{u'_{k,i}u'_{k,j}}$ is the turbulent dispersion term.

To solve Eqs. (2.17) and (2.18) for α_k and $\bar{u}_{k,i}$, the velocity of the wind phase $\bar{u}_i$ is required. Under the assumption of one way coupling between the rain phase and the air phase (i.e. the air phase influences the rain phase, but not the other way around which, as outlined in Sec. 4.2, is generally reasonable), the steady-state velocity of the air phase around the building can be estimated independently of Eqs. (2.17) and (2.18). In particular, because only the steady-state velocity of the air is required, efficient 3D steady Reynolds-averaged Navier–Stokes (RANS) solutions can be used to estimate $\bar{u}_i$. In this work the 3D steady RANS with realizable k-ϵ model (*Shih et al.*, 1995) is used.

To estimate the turbulent dispersion term $\overline{u'_{k,i}u'_{k,j}}$, the model outlined in (*Kubilay et al.*, 2015a, 2017) is adopted. The model is based on relating the velocity fluctuations in the wind flow to the fluctuations in the rain phases through a response coefficient C_t, as:

$$C_t^2 = \frac{\overline{u'_{k,i}u'_{k,j}}}{\overline{u'_i u'_j}} = \frac{1}{1+\frac{t_p}{t_{fl}}} \tag{2.19}$$

where $\overline{u'_i u'_j}$ is the turbulent dispersion term of the air phase while t_p and t_{fl} are the particle relaxation time and characteristic large eddy lifetime, respectively. In particular, the ratio of $\frac{t_p}{t_{fl}}$ reflects the relative inertial effect of the rain phase with respect to the air phase, where a smaller ratio represents a smaller inertial effect of the rain phase, and thus a stronger dispersion effect of the turbulent air phase. To estimate t_p and t_{fl}, the following relationships

can be used (*Kubilay et al.*, 2015a; *Shirolkar et al.*, 1996):

$$t_p = \frac{4\rho_w {d_k}^2}{3\mu_a C_d Re_R} \tag{2.20}$$

$$t_{fl} \cong 0.2\frac{k}{\epsilon} \tag{2.21}$$

where k and ϵ are the turbulence kinetic energy and turbulence dissipation rate respectively.

In solving Eqs. (2.17) and (2.18), it should be observed that the same computational domain as used to solve for $\bar{u}_i$ can be adopted. The boundary conditions for each rain phase will consist in imposing the rain phase's terminal velocity for a vertical inlet, while, for a horizontal inlet, the rain phase's velocity is set equal to that of the air phase. Also, to ensure consistency between the steady-state air flows predicted by the RANS model and the mean wind profiles considered in the wind tunnel, the boundary layer of the RANS model should be similar to that of the wind tunnel.

WDR intensity From the solutions of Eqs. (2.17) and (2.18), the WDR impacting the building envelope can be characterized through the specific catch ratio η_{d_k}, representing the fractional amount of WDR impacting the envelope for a specific rain phase, and the catch ratio η that measures the WDR impacting the envelope over all rain phases (i.e. all raindrop diameters). The estimation of η_{d_k} and η can be achieved through the relationships (*Choi*, 1994; *Blocken and Carmeliet*, 2002, 2007; *Kubilay et al.*, 2013):

$$\eta_{d_k}(\boldsymbol{\zeta}) = \frac{\alpha_k |V_n(d_k;\boldsymbol{\zeta})|}{R_h f_h(d_k, R_h)\Delta d_k} \tag{2.22}$$

$$\eta(\boldsymbol{\zeta}) = \int_d f_h(d, R_h)\eta_d(\boldsymbol{\zeta})\mathrm{d}d \approx \sum_{k=1}^{N} f_h(d_k, R_h)\eta_{d_k}(\boldsymbol{\zeta})\Delta d \tag{2.23}$$

where $V_n(d_k;\boldsymbol{\zeta})$ is the normal component to the building envelope of the kth rain phase velocity at $\boldsymbol{\zeta}$. From η, the WDR intensity at any point on the building envelope can be

estimated as:

$$R_{wdr}(\boldsymbol{\zeta}) = \eta(\boldsymbol{\zeta}) R_h \tag{2.24}$$

Rainwater runoff Alongside WDR, rainwater runoff on the building envelope is an important source of water ingress through any damaged envelope components. If an envelope component is damaged, not only will water directly enter due to the impinging rain (i.e. R_{wdr}), but any rainwater runoff belonging to a stream directly above the damaged component will also enter. To model this aspect, the simplified but robust rainwater runoff model outlined in (*Blocken and Carmeliet*, 2012; *Blocken et al.*, 2013) is adopted in this work. The model is based on neglecting the spanwise gradients of the runoff film. This enables the problem to be treated as a 2D problem with primary variable the film thickness h. By assuming the runoff stream to instantaneously follow the Nusselt's velocity profile (*Blocken and Carmeliet*, 2012), the evolution of h can then be described through the following hyperbolic partial differential equation:

$$\frac{\partial h(x,t)}{\partial t} + \frac{g(h(x,t))^2}{\nu} \frac{\partial h(x,t)}{\partial x} = R_{wdr}(x) - R_{abs}(x) \tag{2.25}$$

where g is the gravitational acceleration, ν the kinematic viscosity of water, x the distance from the beginning of the runoff stream, and R_{abs} the absorption rate.

In the case of steady-state rainwater runoff and non-absorption of the undamaged building envelope (i.e. the case of interest for calculating the consequences considered in this work), the previous model admits the solution:

$$\frac{g(\bar{h}(x))^2}{\nu} \frac{\partial \bar{h}(x)}{\partial x} = R_{wdr}(x) \tag{2.26}$$

with the rainwater runoff rate through a unit span width of wall at x given by:

$$q_r(x) = \frac{g(\bar{h}(x))^3}{3\nu} \tag{2.27}$$

where $\bar{h}$ is the film thickness in steady state that can be estimated as:

$$\bar{h}(x) = \left(\frac{3\nu}{g} \int_{x_0}^{x} R_{wdr}(x)dx + (\bar{h}(x_0))^3) \right)^{1/3} \tag{2.28}$$

with x_0 the start point of the rainwater runoff stream.

While simple, this model has been quite carefully validated by *Blocken and Carmeliet* (2012) for the case of modeling rainwater runoff on smooth building facades and is therefore adopted in this work.

2.3.3 Damage models

As outlined in Sec. 2.2, in this work, the susceptibility of each building envelope component to N damage states is modeled through fragility functions. In particular, the damage states are divided into those that are induced by net pressure and those that are induced by inter-story drift.

2.3.3.1 Drift induced damage

For a given envelope component, it is here assumed that damage due to excessive inter-story drift can be modeled by $j = 1, ..., N_{Dr}$ sequential damage states. The term sequential indicates that the occurrence of the jth damage state implies the occurrence of the damage states $j-1, j-2, ..., 1$, and is a widely accepted hypothesis in damage estimation based on fragility functions (*Federal Emergency Management Agency (FEMA)*, 2012a). Due to the coupled nature of wind damage, the time of occurrence of each damage is important. Therefore, unlike in seismic engineering where the peak demands are used to directly identify the most severe damage state, the engineering demand parameters (*edp*'s) are assumed as the instantaneous drifts occurring over the duration of the event, i.e. $edp = Dr(t)$ for $t \in [0, T]$ with $Dr(t)$ evaluated as outlined in Sec. 2.3.1.

To evaluate the evolution of drift induced damage over the duration of the wind event

for a given suite of sequential fragility functions, F_{Dr_j} for $j = 1, ..., N_{Dr}$, it is first necessary to generate a set of thresholds associated with the fragility functions. This can be achieved through the following two-step procedure:

1. generate a realization, u, of a uniform random number in $[0, 1]$
2. estimate the damage threshold, C_{Dr_j}, for each fragility function as $C_{Dr_j} = F^{-1}_{Dr_j}(u)$

Because of the sequential nature of the damage states, the following will hold: $C_{Dr_1} \leq C_{Dr_2} \leq , ..., \leq C_{Dr_{N_{Dr}}}$. To evaluate the drift-based damage state of a given envelope component at $t = \tilde{t}$, it is therefore simply necessary to identify the highest ranked threshold that is smaller than $Dr(\tilde{t})$. This threshold will correspond to the current drift induced damage state of the envelope component.

2.3.3.2 Pressure induced damage

Pressure induced damage can be treated in an analogous fashion to drift induced damage. Therefore, each envelope component is associated with a suite of N_{Pr} sequential fragility functions that can be evaluated over the duration of the event through the initial generation of N_{Pr} pressure thresholds ($C_{Pr_1} \leq C_{Pr_2} \leq , ..., \leq C_{Dr_{P r_N}}$), which are successively compared to the pressure demand in $[0, T]$. Because one of the more vulnerable components of a cladding system to pressure damage are the glass panels, focus is here placed on modeling the pressure induced damage of these elements. In particular, failure of glass during severe wind events is generally due to static fatigue/delayed failure, which cannot be directly evaluated from the peak net pressures. To account for this, the demand parameter for pressure induced damage of glass panels is here taken as the time evolution of the equivalent pressure, and therefore as (*Brown*, 1974; *Beason and Morgan*, 1984; *Calderone and Melbourne*, 1993; *Gavanski and Kopp*, 2011):

$$P_{eq}(t) = \left(\frac{1}{t_{ref}} \int_0^t [p_n(t)]^s dt \right)^{1/s} \tag{2.29}$$

where s is a constant and t_{ref} is a reference time duration which is commonly taken as 60 s or 3 s.

The fragility functions for glass panels that are in terms of this demand parameter can be inferred from experimental work reported in the literature (e.g. *Behr et al.*, 1991).

2.3.3.3 Damage coupling

As discussed in Sec. 2.2, interdependencies will generally exist between the drift and pressure induced damage states (e.g. the occurrence of a drift-based damage state is likely to affect the occurrence of a pressure induced damage state and vice versa). To model this interdependency, the vectors of damage thresholds of a given envelope component, e.g. $\{C_{Dr_1}, C_{Dr_2}, ..., C_{Dr_{N_{Dr}}}\}^T$ for drift and $\{C_{Pr_1}, C_{Pr_2}, ..., C_{Pr_{N_{Pr}}}\}^T$ for pressure, can be related through coupling matrices. Following this approach, each group of thresholds is associated with a matrix of coefficients $c_{ij} \in [0, 1]$ with i the index over the damage states of the group and j the index indicating the group of thresholds to be reduced through multiplication with c_{ij} due to the occurrence of damage state i. In practice, the approach is based on degenerating the thresholds of dependent damage states on the occurrence of damage state i and vice versa. If any two damage states are to be considered independent, then the coupling coefficient is set to one indicating no degeneration. If, on the other hand, the occurrence of a limit state is to be considered terminal, i.e. the component is lost after its occurrence, all coupling coefficients are set to zero. To model uncertainty in the degeneration process, the coefficients c_{ij} can be taken as random, as illustrated in the case study.

2.3.4 Consequences

The consequences considered in this framework are the final damage states of each envelope component and the total volume of ingressed rainwater due to the progressive damage to the building envelope. In the following, these consequences will be indicated as:

1. $\mathbf{N}_{DS_{Dr}}$ = vector collecting the total number of envelope components in each drift in-

duced damage state.

2. $\mathbf{N}_{DS_{Pr}}$ = vector collecting the total number of envelope components in each pressure induced damage state.

3. V_w = total volume of ingressed water.

Obviously, the choice of consequences is by no means limited to those indicated above and any parameter generated during the analysis can be considered as a consequence. Therefore, the set outlined here should be considered as illustrative.

2.4 Simulation Strategy

To estimate the consequences of Sec. 2.3.4 for a windstorm of given intensity (measured in terms of the mean wind speed at the building top $\bar{V}_H$ and concurrent rainfall intensity R_h) while accounting for uncertainties in the capacities of the envelope components, the Monte Carlo algorithm of Fig. 2.3 is adopted. The algorithm is based on stepping through each event, with time step Δt, and evaluating, at each time step, the models of Sec. 4.2. Efficiency is achieved by recognizing how the steady state simulation of the wind driven rain can be separated from the transient simulation of the structural dynamics and internal pressures. The uncertainties, modeled by the fragility functions, in the capacities of the envelope components can be accounted for by firstly generating, for each storm of the simulation, a realization of a uniform random vector $\mathbf{N}_u$ in $[0, 1]$. The components of $\mathbf{N}_u$ can then be used to identify (through the two-step procedure of Sec. 2.3.3.1), sets of thresholds for each set of fragility functions. As outlined in Fig. 2.3, by simulating over $m = 1, ..., N_s$ samples, N_s realizations of the consequences will be obtained and can be used to probabilistically characterize the consequences. It is important to observe that, because the algorithm of Fig. 2.3 is based on Monte Carlo simulation, together with the uncertainties in the capacity of the components, any other source of uncertainty can be directly included. For example, in the case study of Sec. 4.7, record-to-record variability in the external pressure traces is treated

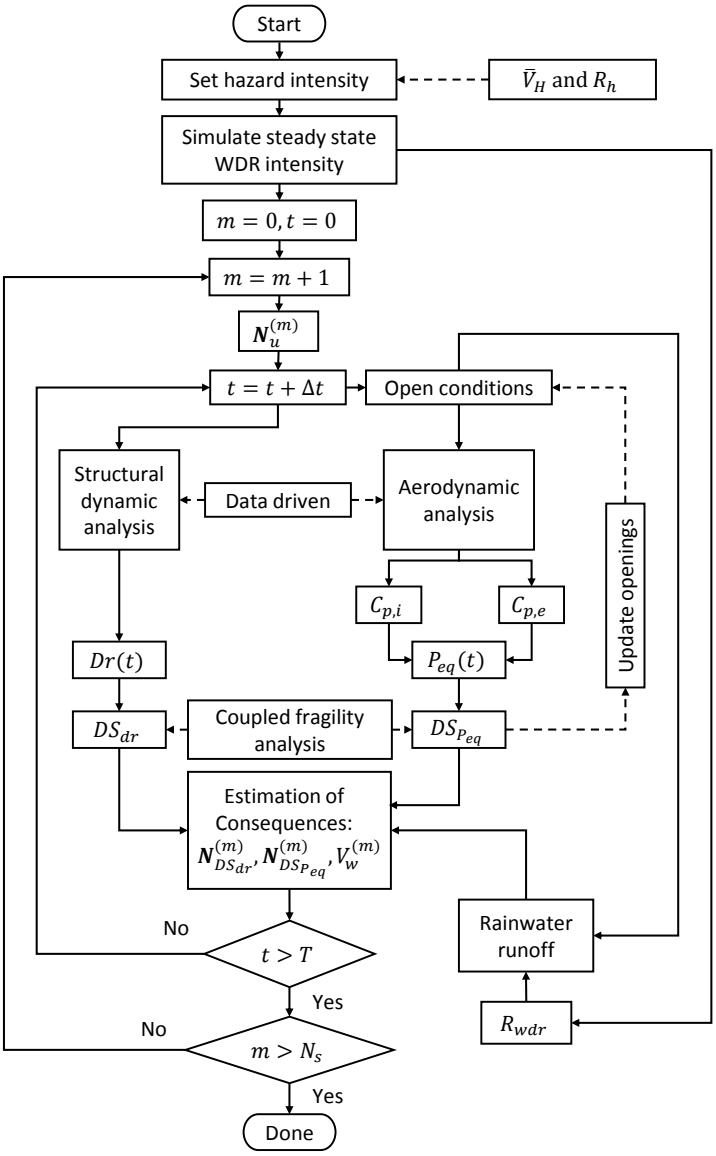

Figure 2.3: Flowchart of the proposed simulation strategy.

through calibrating a stochastic model to the external pressure data, and then generating a realization of the external pressure coefficients at each point, m, of the simulation.

2.5 Case study

2.5.1 Building system

2.5.1.1 Structural system

The building system analyzed in this case study is a 45-story steel building. The geometry of the building is shown in Fig. 2.4. The structural system consists in box section columns that are grouped in plan as indicated in Fig. 2.5(b) (C1-C18). In particular, the mid-line widths, D_i, of the box sections are required to belong to the set {0.2 m,0.25 m,...,3 m} with web thickness given by $D_i/20$. The beams are standard AISC (American Institute of Steel Construction) W24 steel profiles and are grouped from B1 to B6 following the scheme outlined in Fig. 2.4(b). Both columns and beams are grouped three floors at a time. The diagonals are also required to belong to the AISC W24 steel profiles and are grouped as symmetric pairs over the height of the building. The above outlined grouping led to 375 independent design groups. To estimate the response of the structural system, a finite element model was developed in OpenSees (*McKenna et al.*, 2013) using "elasticBeamColumn" element objects for each column, beam and bracing element. The steel was assumed to have a Young's modulus of 200 GPa while each floor was considered rigid in its plane, with area density of 0.38 t/m^2. The contribution of the cladding system to the lateral stiffness of the building system was assumed negligible. The first 10 vibration modes were extracted and used during the direct integration of Eqs. (2.3). The modal damping ratios were taken to be equal to 1.4% as suggested in (*Satake et al.*, 2003; *Spence and Kareem*, 2014b) for steel frame structures at the vibration levels of interest to this work. The integration of Eqs. (2.3) was carried out through the Laplace scheme outlined in (*Spence and Kareem*, 2013). The sections of each design group were assigned to ensure the satisfaction of a limit on the peak inter-story drift ratio of 1/400 under dynamic wind loads calibrated to a 50-year mean recurrence interval (MRI) wind speed, as well as an essentially elastic member behavior under a 3000-year MRI wind speed (for estimation of these wind speeds, see Sec. 2.5.2.1). A list of final sections sizes

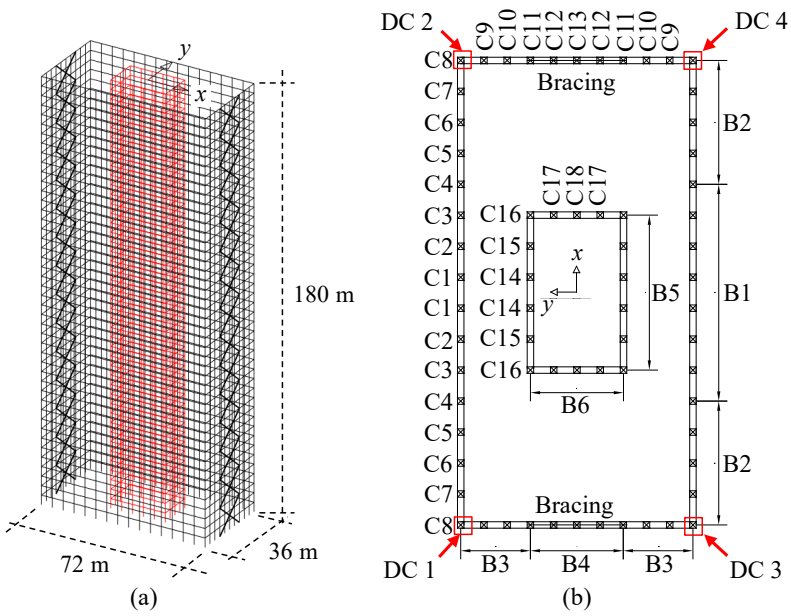

Figure 2.4: (a) 3D view of the 45-story building and (b) typical floor layout with the four design columns (DC) highlighted.

can be found in 4.10. The resulting first three natural frequencies were 0.2568 Hz, 0.3083 Hz and 0.4568 Hz. The distribution of the expected peak inter-story drift ratios for y-direction wind at each floor of the four design columns of Fig. 2.4 are shown in Fig. 2.5, where the slight difference between the peaks of design columns 1 and 3, as compared to design columns 2 and 4, was due to a moderate misalignment of the wind tunnel model, i.e. the wind was not blowing exactly parallel to the y axis.

2.5.1.2 Envelope and interior space of the building

The cladding system of the building was considered composed by 1.2×2 m^2 dual-panel laminated glass cladding components with the outer glass panel thickness of 13 mm and inner glass panel thickness of 6 mm. Each glazed cladding component was considered mounted 1.5 m above the lower floor and 0.5 m below the upper floor, as illustrated in Fig. 2.6. Only the glazed cladding components were considered damageable during a severe wind event. In total, 2700 glazing components belonged to each x direction face while 1350 belonged to each y direction face.

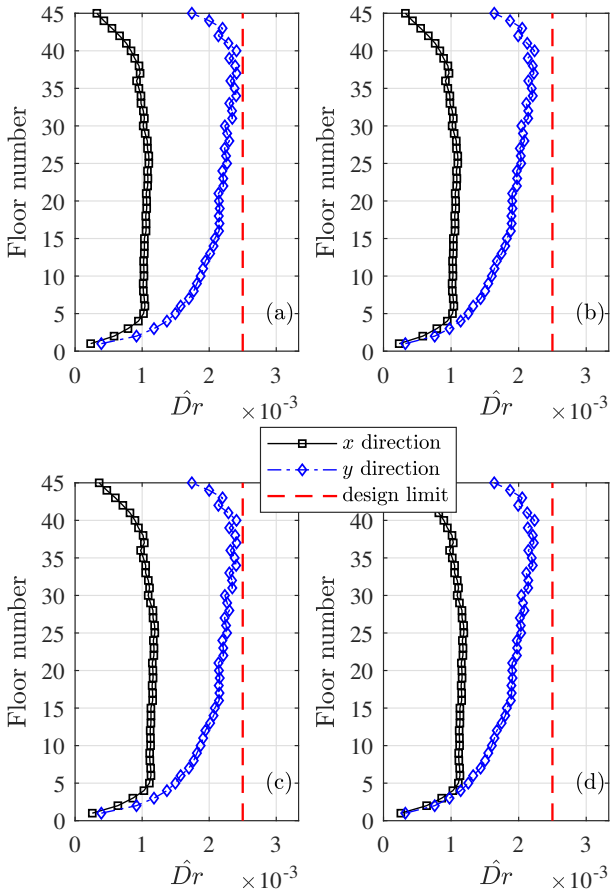

Figure 2.5: Expected peak drift ratio response, $\hat{Dr}$, in the x and y direction for a y-direction 50-year MRI wind speed: (a) Design Column 1; (b) Design Column 2; (c) Design Column 3; (d) Design Column 4.

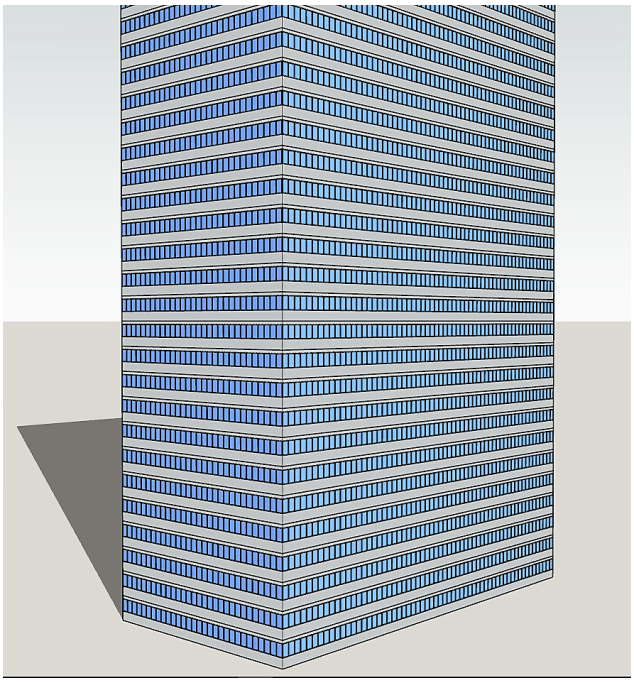

Figure 2.6: Illustration of the envelope system.

Each floor of the building is assumed to be composed of open office space. Therefore, in calibrating the internal pressure model of Sec. 2.3.2.1, a single compartment was considered for each floor. For simplicity, the floors were considered isolated from one another, i.e. no internal openings were considered between two successive floors.

2.5.2 Hazard intensity

2.5.2.1 Wind event

The building system was considered to be located in Miami, Florida and therefore subject to the Miami hurricane climate. In particular, the building is considered located at a site of roughness length $z_0 = 1.28$ m. To estimate the wind speeds with specified MRIs for this site, the data-driven hazard model outlined in (*Spence and Kareem*, 2014a) was considered. To calibrate the hazard model, milepost 1450 of the simulated hurricane database of the National Institute for Standards and Technology (NIST) was considered. This led to a site specific mean hourly 50-year MRI wind speed of $\bar{V}_H = 46.0$ m/s (used to assess the serviceability limit state of Sec. 4.7.1.1) and a site specific mean hourly 3000-year MRI wind speed of $\bar{V}_H = 66.77$

m/s. Because wind effects are traditionally estimated over a duration of one hour, the length of the windstorm was set as $T = 1$ h. A wind direction parallel to the y axis (see Fig. 2.4) was considered, as this was seen to be the most severe in terms of building response. The wind tunnel estimated dynamic external pressure coefficients, $C_{p,e}^{(1)}(t), ..., C_{p,e}^{(K)}(t)$, were derived from wind tunnel data collected on a 1/360 rigid scale model of the building. The data was part of the Tokyo Polytechnic University's (TPU) aerodynamic database (*Tokyo Polytechnic University*, 2008) and was measured considering a sampling frequency of 1000 Hz and wind speed at the building top of 11 m/s. A total of $K = 512$ pressure taps were used for 32 s of recorded data. To enable the implementation of the Monte Carlo simulation scheme of Sec. 2.4 while accounting for the record-to-record variability in the vector of external pressure coefficients, $\mathbf{C}_{p,e}(t) = \{C_{p,e}^{(1)}(t), ..., C_{p,e}^{(K)}(t)\}^T$, a proper orthogonal decomposition stochastic simulation model was adopted (*Chen and Kareem*, 2005). The first 10 spectral modes where used in simulating $\mathbf{C}_{p,e}(t)$ with a sampling frequency of 2 Hz. Details of the model can be found in 2.8. In interpolating the data, i.e. in defining the function Γ of Eq. (2.7), a bilinear scheme was adopted with linear extrapolation to the edges of each building face.

2.5.2.2 Concurrent rain event

The concurrent rain event was taken to have a rainfall intensity of $R_h = 45.0$ mm/h. This value is an estimation, from the data provided by the United States Weather Bureau in (*Bureau*, 1957-1960), of the expected rainfall intensity during a hurricane event occurring in Miami. In particular, the expected value was considered, as the limited available data would seem to suggest statistical independence between the concurrent rainfall intensity and the maximum hurricane wind speed (*Rappaport*, 1999; *Dong et al.*, 2017). For estimating the catch ratio η over the building envelope, the steady state wind field around the building was solved in OpenFoam (*Weller et al.*, 1998) using a steady RANS with realizable k-ϵ model. The boundary layer was calibrated to coincide with that of the wind tunnel tests of Sec. 2.5.2.1, while the rain event was characterized by 17 rain phases with diameters

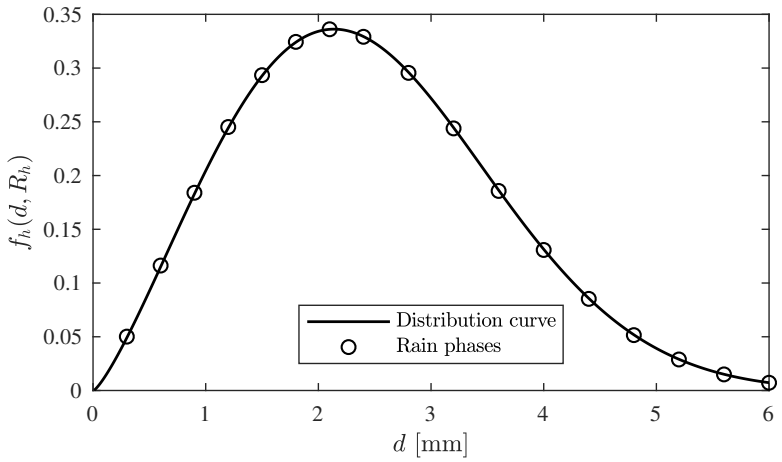

Figure 2.7: Rain drop diameter distribution for $R_h = 45.0$ mm/h (*Best*, 1950).

$\{0.3, 0.6, 0.9, ..., 5.6, 6.0\}$ mm that followed the distribution suggested in (*Best*, 1950) and shown in Fig. 2.7. The computational domain consisted of a $3636 \times 1872 \times 1080$ m^3 tank with mesh density $100 \times 90 \times 155$. The resulting mesh around the building is illustrated in Fig. 2.8. The boundary faces, inlet face, side faces and top face were set as $5H$ (with H building height) from the building while the outlet face was set at $15H$ from the building, as illustrated in Fig. 3.10. The boundary conditions for the wind and rain fields were based on the suggestions outlined in (*Kubilay et al.*, 2015a, 2013, 2017). In particular, the boundary conditions for each rain phase were based on the terminal velocities shown in Fig. 2.10. In solving Eqs. (2.17) and (2.18), the model settings suggested in (*Kubilay et al.*, 2015a; *Huang and Li*, 2010) were considered and the solver reported in (*Kubilay et al.*, 2013) was implemented.

2.5.3 Calibration of the damage model

A set of three sequential drift induced damage states were considered for each cladding element. The associated fragility functions are shown in Fig. 2.11 together with the descriptions of the damage states. The fragility functions were derived from the P-58 fragility database (*Federal Emergency Management Agency (FEMA)*, 2012a). The adequacy of using seismic fragilities in this case can be traced back to how the demand parameters are the same

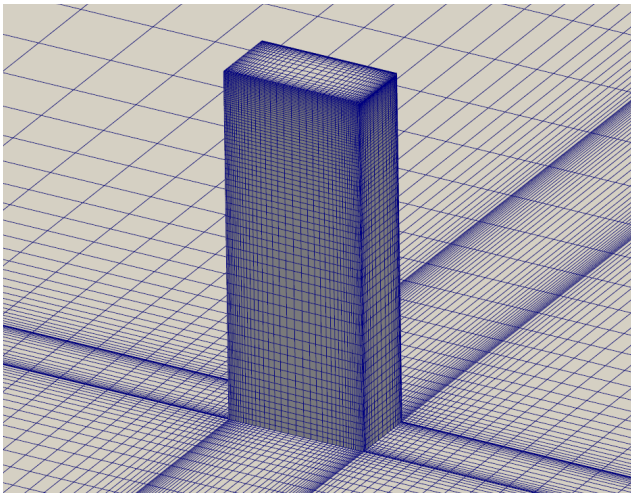

Figure 2.8: Computational mesh around the building.

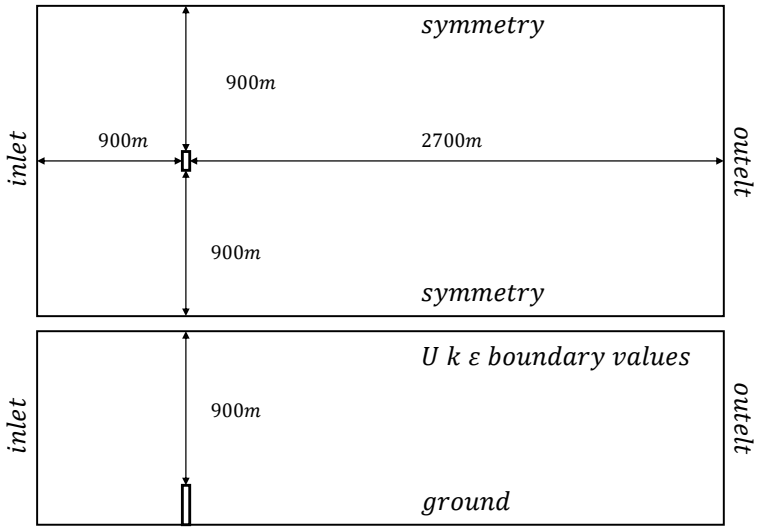

Figure 2.9: Sketch of computational domain.

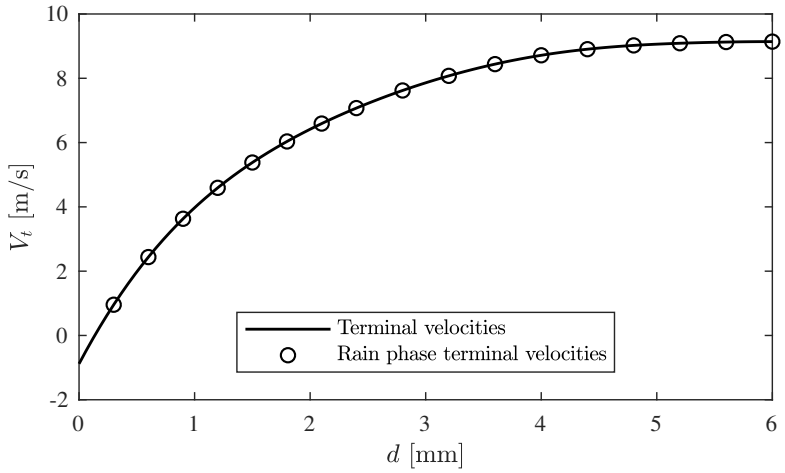

Figure 2.10: Rain drop terminal velocities (*Gunn and Kinzer*, 1949).

for both wind and seismic applications, i.e. dynamic inter-story drift ratio. The initiation mechanism of the damage states should therefore be similar. Also, the structure can be seen as a filter suppressing, to a certain extent, the differences between the dynamic characteristics of the demand parameters. Having said this, the fragilities of the P-58 database can only be considered a first approximation of the actual wind fragilities. To account for this, their dispersions were increased to the upper bound suggested in (*Federal Emergency Management Agency (FEMA)*, 2012a) for applications where significant differences exist between the test conditions under which the fragilities were derived and the actual loading conditions to which the component will be subject. This led to the lognormal distributions with parameters as reported in Table 3.1. Alongside the drift-based damage states, pressure-based damage states are considered for the outer and inner glass panels of the cladding element. One damage state for each panel is considered that corresponds to the loss of the glass panel. The demand is taken as the evolution of the 60 s equivalent pressure $P_{60} = P_{eq}$, i.e. Eq. (2.29) with $t_{ref} = 60$ s. The fragility functions associated with this damage state for the inner and outer glass panels are shown in Fig. 2.12 and are based on the experimental data reported in (*Behr et al.*, 1991). As suggested in (*Behr et al.*, 1991), the fragility functions were taken as normally distributed with parameters as reported in Table 3.1. It should be observed that the two fragility functions for the glass panels should be considered as separate

fragility sets as they have different demands. This is because, under the assumption that the pressure between the inner and outer glass panels can be taken as the internal pressure until the loss of the outer panel, P_{60} will be different for the two panels. This implies that a total of three fragility sets are considered in this example.

To model the dependency between the damage states of the three fragility sets, the coupling matrices of Sec. 2.3.3.3 were defined as:

$$\mathbf{C}_{Dr} = \begin{bmatrix} 1 & 1 \\ 0.9 & 0.9 \\ 0.1 & 0.1 \end{bmatrix}, \quad \mathbf{C}_{Pr_1} = \begin{bmatrix} 1 & 1 \end{bmatrix}, \quad \mathbf{C}_{Pr_2} = \begin{bmatrix} 0 & 0 \end{bmatrix}$$

where $\mathbf{C}_{Dr}$ defines the coupling between the three drift induced damage states (rows of $\mathbf{C}_{Dr}$) and the two pressure induced damage states (columns of $\mathbf{C}_{Dr}$), $\mathbf{C}_{Pr_1}$ defines the coupling between damage state of the outer panel of the cladding element and the drift induced damage states (column one of $\mathbf{C}_{Pr_1}$) as well as pressure induced damage state of the inner panel (column two of $\mathbf{C}_{Pr_1}$), while $\mathbf{C}_{Pr_2}$ defines the analogous quantities for the damage state of the inner panel. In defining the coupling matrices, it was assumed that the occurrence of the first drift induced damage states does not affect the strength of the glass, while the cracking of the glass will reduce the strength of the glass panels. Because the inner glass panel is not subject to demand until the loss of the external glass panel, the loss of this last was assumed to not affect the possibility of drift induced damage that could still affect the inner glass panel, hence the coupling coefficients were taken as one. The loss of the inner glass panel, on the other hand, indicates the complete loss of functionality of the cladding element (i.e. pressure induced loss of the inner panel implies the loss of the outer panel, otherwise there would be no pressure demand on the inner panel), therefore the coupling coefficients were taken as zero. To model the significant uncertainty that will inevitably affect the coupling coefficients, they were taken as truncated (in $[0, 1]$) normal random variables with means as indicated in the matrices and standard deviations of 0.1. Finally, for the estimation of the

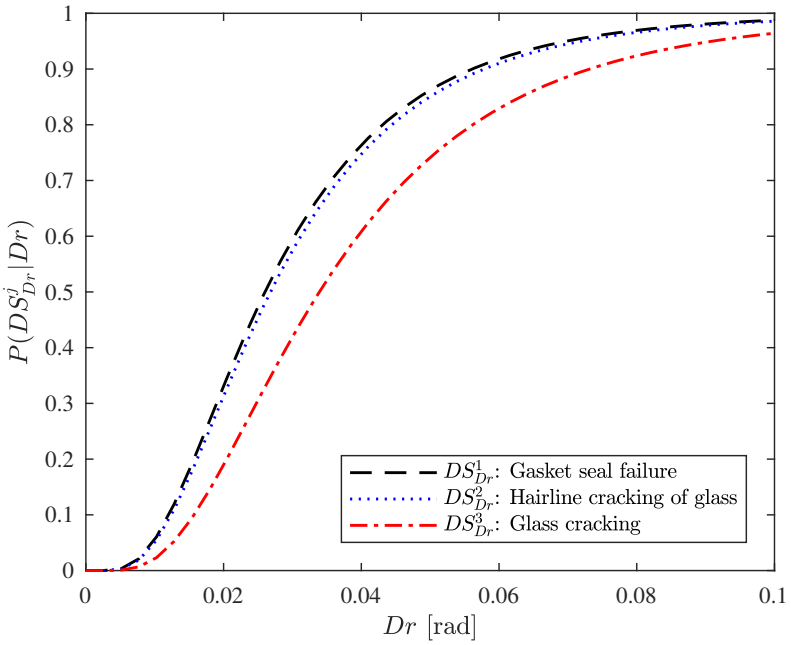

Figure 2.11: Fragility functions associated with drift induced damage.

Table 2.1: Description and parameters of the fragility functions.

Affected element	Demand (edp)	Label	Median	Dispersion	Mean	Std	Units
Cladding component	Story drift (Dr)	DS^1_{Dr}	0.026	0.6	-	-	rad
Cladding component	Story drift (Dr)	DS^2_{Dr}	0.0268	0.6	-	-	rad
Cladding component	Story drift (Dr)	DS^3_{Dr}	0.0339	0.6	-	-	rad
Outer glass panel	Net pressure (P_{60})	$DS^1_{P_{60}}$	-	-	11.37	2.09	kPa
Inner glass panel	Net pressure (P_{60})	$DS^2_{P_{60}}$	-	-	5.29	0.91	kPa

ingressed water after the loss of both glass panels of the cladding element, an opening area of $A_w = 2.4$ m^2 was considered.

2.5.4 Results

To illustrate the proposed framework, two cases are discussed below. The first focuses on the presentation of the method for a single realization of the stochastic wind loads, coupling matrices, initial internal pressure of Eq. (2.15), and $\mathbf{N}_u$. The second case focuses on the results obtained from the Monte Carlo strategy of Sec. 2.4 run for $N_s = 2000$.

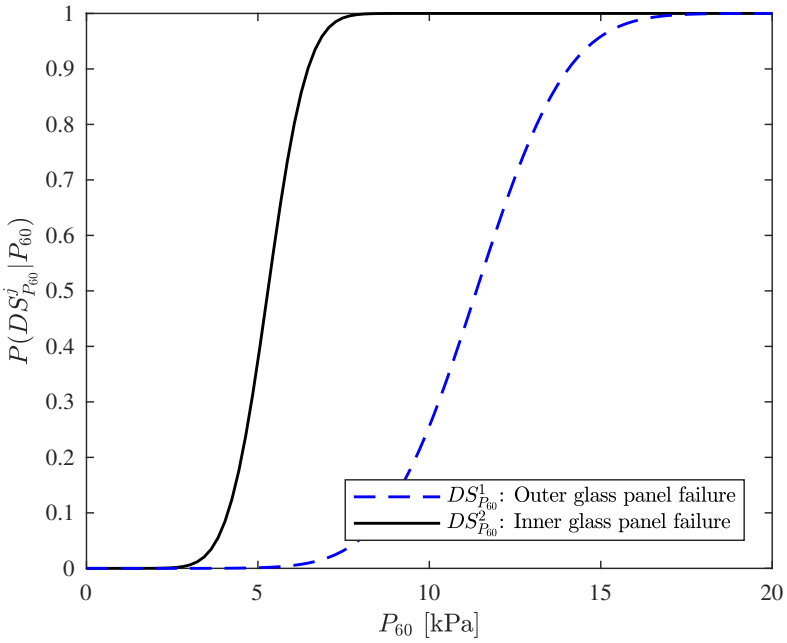

Figure 2.12: Fragility functions associated with pressure induced damage.

2.5.4.1 Single realization

Damage The maps associated with the occurrence, as a final damage state, of the three drift induced damage states are shown in Fig. 2.13. From this figure, it can be seen that damage occurs on all four faces of the building. This can be traced back to how the building has been designed to meet a common drift limit in both the x and y directions (see Fig. 2.4). It is interesting to see that only one window experienced DS^3_{Dr} (i.e. glass cracking) due to drift. This illustrates how buildings designed to meet typical drift limits under serviceability loads are unlikely to suffer severe drift-based damage at ultimate load levels. The maps of final damage states due to the net wind pressure are shown in Fig. 2.14. As can be seen, most of the damaged glass panes are on the windward and the side faces. This distribution of damage is due to the aerodynamic response of the building, for which the largest pressures tend to occur around the edge regions of the right and left faces. It is also interesting to observe how some damage occurred in windward cladding components. This can be attributed to the negative internal pressure variations caused by the initial loss of cladding components on the side faces of the building.

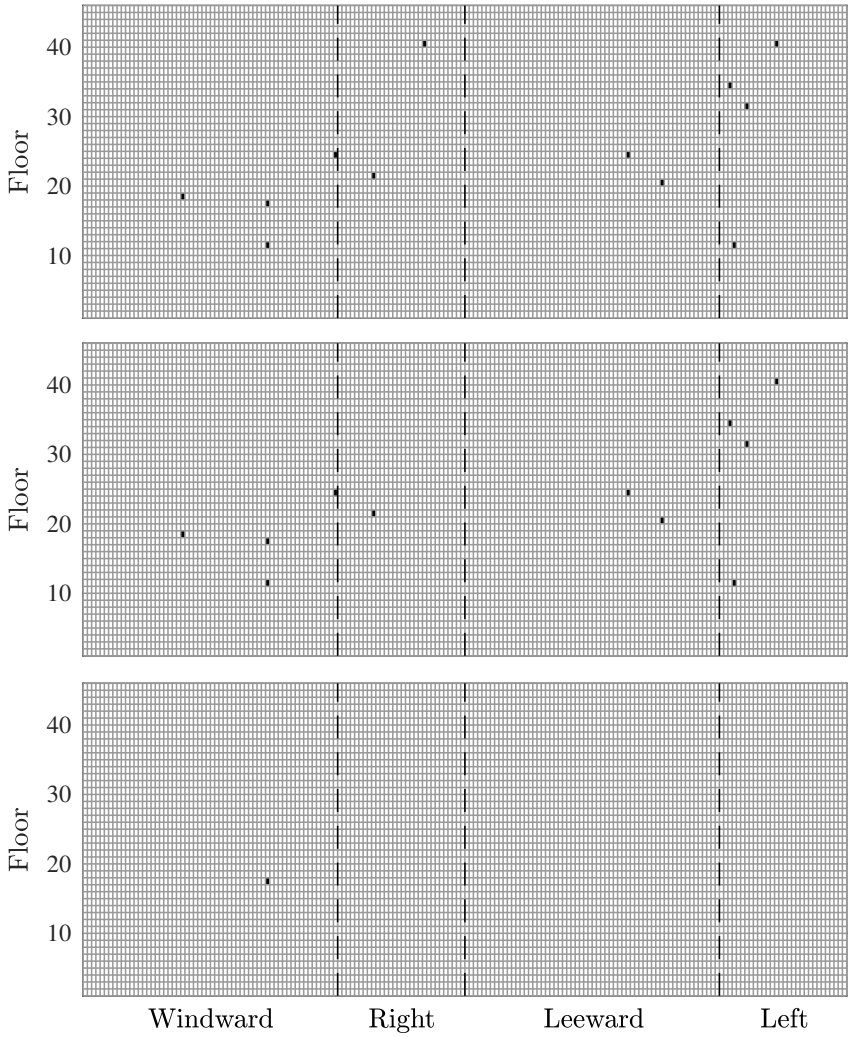

Figure 2.13: Building envelope damage due to story drift: DS^1_{Dr} top, DS^2_{Dr} middle, and DS^3_{Dr} bottom. The map is constructed by continuously connecting the windward face, right face, leeward face, and left face.

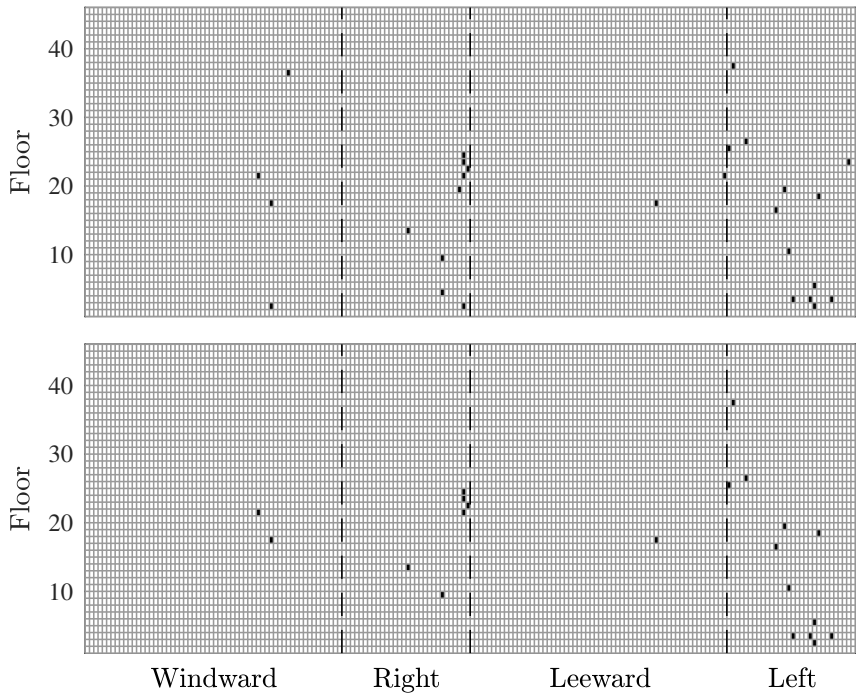

Figure 2.14: Building envelope damage due to net pressure: DS^1_{p60} (outer glass panel) top and DS^2_{p60} (inner glass panel) bottom.

To illustrate the evolution and interdependency of the damage to the envelope, Fig. 2.15 shows the dynamic internal pressure history for the 29th cladding element of the right face (counted from left to right) at the 21st floor. As can be seen, after the occurrence of $DS^2_{P_{60}}$ in this cladding element, the negative external pressure at this location quickly causes the internal pressure to drop. This increase in negative internal pressure then caused the 41st cladding element of the windward floor to failure due to pressure, i.e. $DS^2_{P_{60}}$ occurred, which, due to the positive external pressure on the windward face, caused a quick increase in internal pressure. This illustrates both the progressive nature of wind damage as well as the significant coupling that exists between the demands and the damage states. From Fig. 2.15 it is interesting to observe how the internal pressures remain relatively constant once the effects of an opening have attenuated. This suggests the possibility of approximating the dynamic internal pressures as a series of constant pressures that are updated at each new opening. While this would avoid having to solve the non-linear system defined by Eqs. (2.11)–(2.12), the identification of the constant value to assign to the internal pressure at each new opening

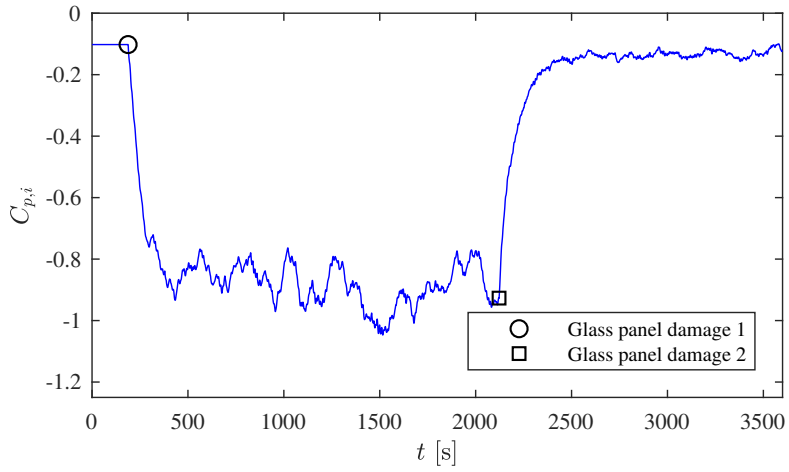

Figure 2.15: Dynamic internal pressure history for the 29th cladding element of the right face (counted from left to right) of the 21st floor, $(29, 21)$. "Glass panel damage 1" indicates the occurrence of $DS^2_{P_{60}}$ on the right face at $(29, 21)$ while "Glass panel damage 2" indicates the occurrence of $DS^2_{P_{60}}$ on the windward face at $(41, 21)$.

is not trivial, due to its dependency on the failure sequence of the envelope components. An approach of this kind would also neglect the dynamic fluctuations in the internal pressures, which, as can be seen from Fig. 2.15 after the first opening, can be relatively large. However, the successful identification of such a simplified model would increase both the computational efficiency and simplicity of the proposed approach and will be investigated in future research efforts.

To further illustrate the coupling between the damage states, Fig. 2.16 reports the first 300 seconds of the absolute drift ratio demand associated with the 44th cladding component of the windward face of the 17th floor, which was the first (and only) cladding element to suffer DS^3_{Dr}, i.e. glass panel cracking due to drift. As can be seen from Fig. 2.16, DS^3_{Dr} occurs at 195 s and was preceded by the occurrence of DS^1_{Dr} and DS^2_{Dr}. The occurrence of DS^3_{Dr} caused the capacity of the glass panels, $C^1_{p_{60}}$ and $C^2_{p_{60}}$, to drop by 87.4%, therefore leading to pressure induced failure of the external glass panel, as illustrated in Fig. 2.17(a), which quickly led to failure of the inner glass panel due to excessive equivalent pressure, Fig. 2.17(b).

Finally, Table 2.2 reports the final damage states of the cladding elements of each face

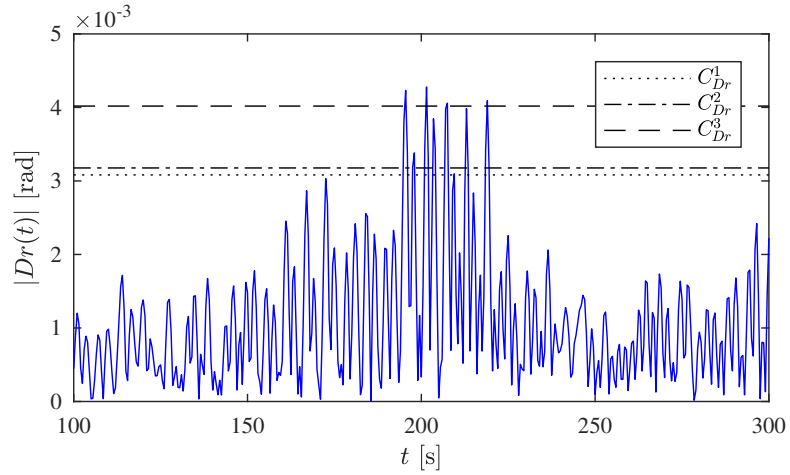

Figure 2.16: First 300 s of the absolute drift ratio demand associated with the 29th cladding component of the windward face of the 21st floor.

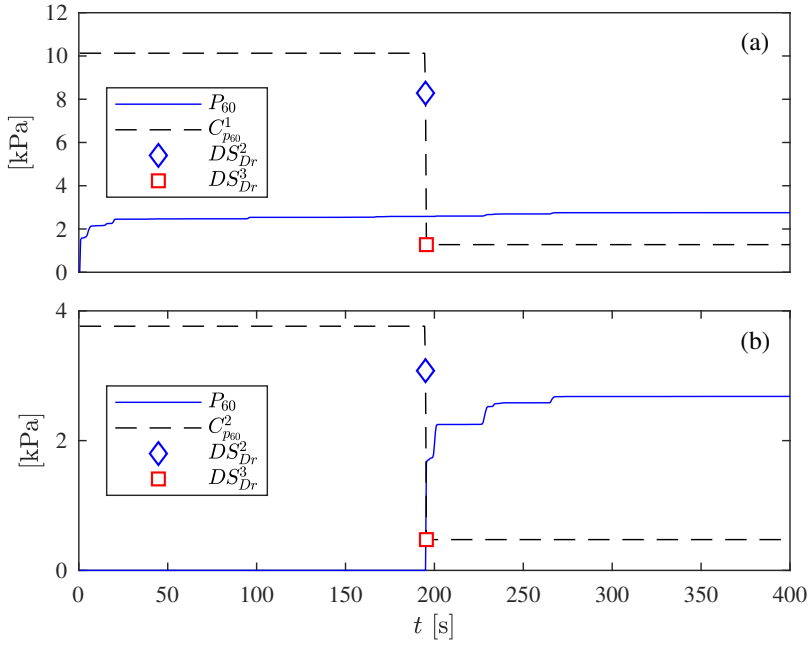

Figure 2.17: Equivalent pressure demands and capacities of the glass panels associated with the 29th cladding component of the windward face of the 21st floor: (a) outer glass panel; (b) inner glass panel.

Table 2.2: Final damage states for the cladding elements on each face of the building.

Consequence	Windward face	Right face	Leeward face	Left face	Total
$N_{DS^1_{Dr}}$	0	1	0	0	1
$N_{DS^2_{Dr}}$	3	1	2	4	10
$N_{DS^3_{Dr}}$	1	0	0	0	1
$N_{DS^1_{P_{60}}}$	2	3	1	1	7
$N_{DS^2_{P_{60}}}$	2	6	0	12	21

of the building. As can be seen, damage is concentrated on the left and right face of the building, with a predominance of pressure induced damage, indicating how it is the local pressures that govern damage to the envelope system of a well designed structural system.

Rainwater ingress The estimated wind driven rain intensity R_{wdr} over the four faces of the building is shown in Fig. 2.18, where the dependency of the wind driven rain distribution on the steady state wind field that forms around the building can be seen from, for example, the classic ring of large wind driven rain intensities on the top edges of the windward face. The rate, q_{wdr}, and the total amount of rainwater ingressed into the building due to envelope damage are shown in Fig. 2.19. From Fig. 2.19, the progressive nature of the wind induced damage to the building envelope can be seen from how the rate of total ingressed water, Fig. 2.19(a), increases as the number of lost cladding elements increases. This leads to the time dependent total volume of ingressed water of Fig. 2.19(b).

Figure 2.20 shows how the results of the analysis can be deaggregated and presented in terms of water ingressed at each floor. In particular, Fig. 2.20 reports the total volume of water entering each floor as a function of time. This deaggregated result shows how the water ingressed towards the top of the building is relatively moderate, with most rainwater entering near the middle and the bottom of the building. This result is a direct consequence of the distribution of damaged cladding elements, as reported in Fig. 2.14, as well as the effects of the rainwater runoff. With respect to this last, this occurs due to the fact that longer streams above the damaged cladding component lead to a greater volume of water

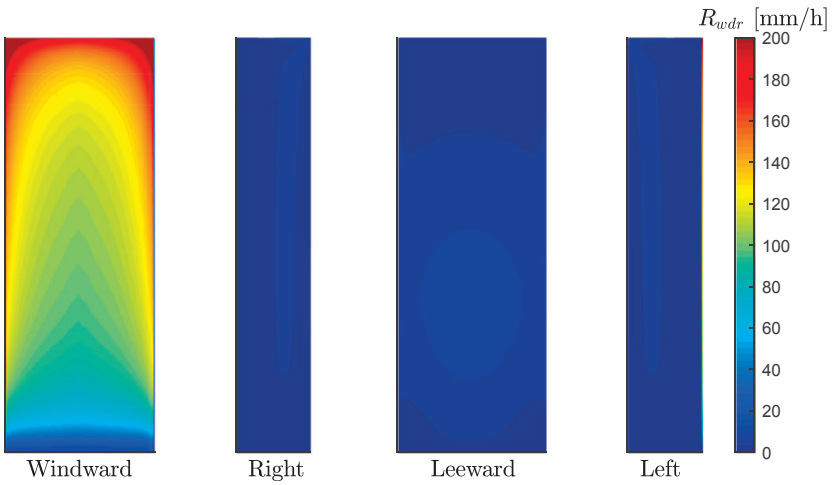

Figure 2.18: Distributions of the wind driven rain intensity R_{wdr} on the four faces of the building.

entering the breach.

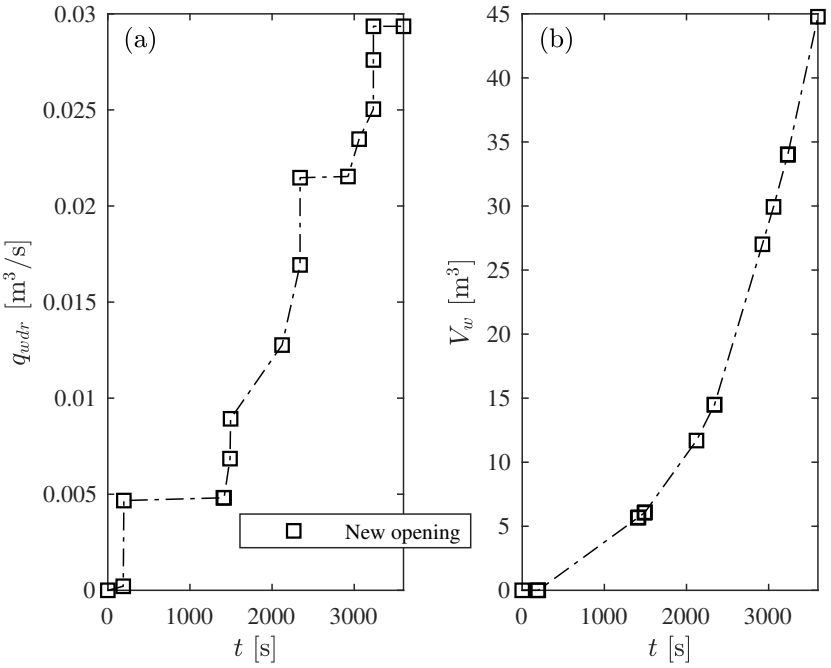

Figure 2.19: Total rainwater ingress: (a) rate of rainwater ingress, q_{wdr}, through the openings in the building envelope; (b) total volume of rainwater ingressed into the building.

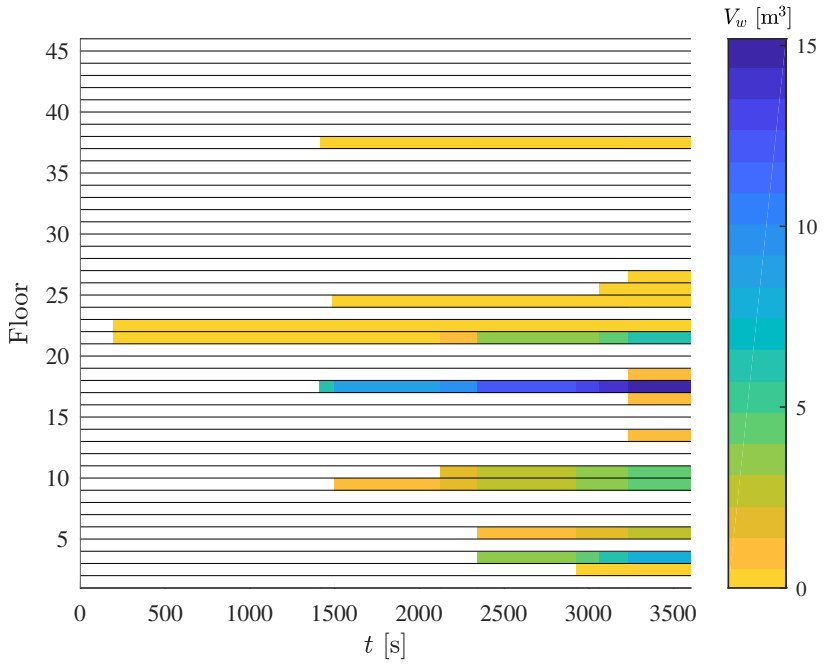

Figure 2.20: Volume of rainwater ingressed into each floor of the building over time.

2.5.4.2 Monte Carlo simulation

To probabilistically characterize the performance of the cladding system, the Monte Carlo strategy of Sec. 2.4 was carried out with $N_s = 2000$. To model the inevitable uncertainty in the damping ratios, these were taken as lognormal random variables with mean 1.4% and coefficient of variation 0.3, as suggested in (*Bashor et al.*, 2005; *Bernardini et al.*, 2015). Figures 2.21 and 2.22 report the maps associated with the probability of each cladding element assuming one of the drift induced damage states (i.e. DS^1_{Dr}, DS^2_{Dr}, or DS^3_{Dr}), or pressure induced damage states (i.e. $DS^1_{P_{60}}$ or $DS^2_{P_{60}}$) at the end of the windstorm.

From Fig. 2.21, the relatively greater sensitivity of the system to y direction drift can seen. By comparing Fig. 2.21 with Fig. 2.22, the dominance of local pressure induced damage as the mechanism leading to loss of glass panels can be observed by recognizing how only the third drift induced damage state, i.e. DS^3_{Dr}, produces glass cracking that directly leads to glass panel loss. However, as can be seen in Fig. 2.21, this damage state has a negligible probability of occurrence (maximum probability of occurrence over an order of magnitude less than that seen for $DS^1_{P_{60}}$ or $DS^2_{P_{60}}$). This illustrates how, for a structural system designed to meet typical drift ratio limits under serviceability load considerations, drift is unlikely to cause glass panel loss. Having said this, Fig. 2.21 shows that under ultimate load levels, i.e. 3000-year wind event, some cracking and gasket damage could occur, leading, in general, to a greater probability of pressure damage due to coupling, i.e. reduction in the capacity of the glass panels to resist pressure. It is also interesting to observe that, for this event, non-negligible pressure induced failure probability was observed not only on the right and left faces of the building, but also on the windward face. This was in part due to the internal pressure variations occurring after the loss of one of the lateral cladding elements.

Figures 2.23 and 2.24 report the histograms, with means and standard deviations, associated with the total number of cladding elements to assume one of the five possible damage states. Significant deviations around the means are seen for all final damage states, which illustrates the important role played by the uncertainty in the system.

With respect to rainwater ingress, Fig. 2.25 reports the histogram of the total volume of water ingressed over the duration of the wind event. As can be seen, the uncertainty in the system has a significant effect on the amount of rainwater entering the building with a coefficient of variation of 0.40. Figure 2.26, reports the deaggregation of the total ingressed water at each floor in terms of the mean and standard deviation. As can be seen, the cladding system shows particular sensitivity to damage over the first 35 floors. This can be traced back to the significant probability of pressure induced loss of a glass panel on the right and left face over these floors, as illustrated in Fig. 2.22.

Finally, notwithstanding the full scale of the case study, it should be observed that the results of this section were generated in around 5 to 6 hours through a non-optimal code developed in MATLAB and running on a standard four-core desktop computer with 48 Gigabytes of RAM. From a licensing standpoint, apart from MATLAB, all software used in the code is open source, i.e. OpenSees and OpenFOAM for structural/CFD analysis. This shows the potential of the framework for rapidly providing detailed information on the performance of building envelopes of engineered wind-excited systems.

2.6 Summary and Conclusions

A computational framework is proposed in this paper for the probabilistic damage assessment of building envelopes of wind-excited engineered structures. The framework integrates, within a Monte Carlo simulation environment, wind tunnel driven dynamic response analyses, CFD-based wind driven rain models, wind tunnel informed dynamic internal pressure models, and fragility-based damage analyses. In developing the framework, focus was placed on modeling the interdependencies between damage states induced by excessive dynamic response of the structural system and damage states induced by excessive net pressure on the building envelope components, as well as the interdependencies between damage states and demand parameters. By wrapping the framework around the concept of fragility, the uncertainty in the capacity of the envelope components is modeled in terms of familiar quantities

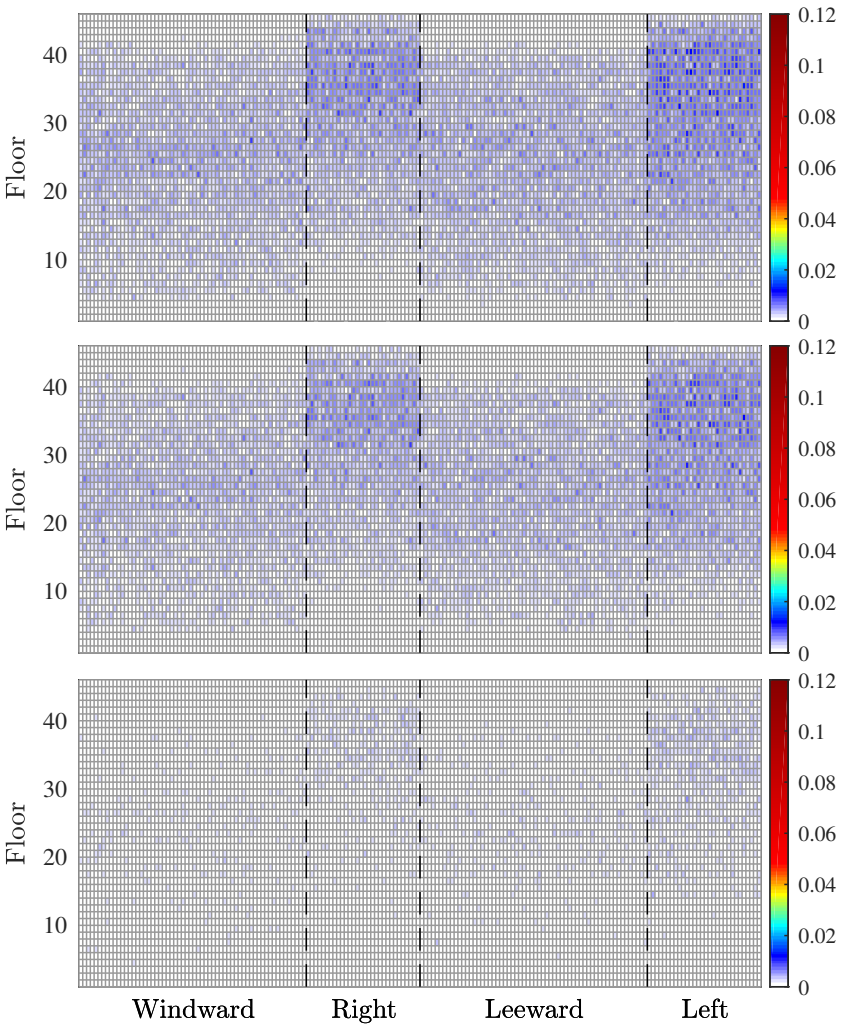

Figure 2.21: Probability of a cladding element assuming as a final damage state DS^1_{Dr} top, DS^2_{Dr} middle, or DS^3_{Dr} bottom.

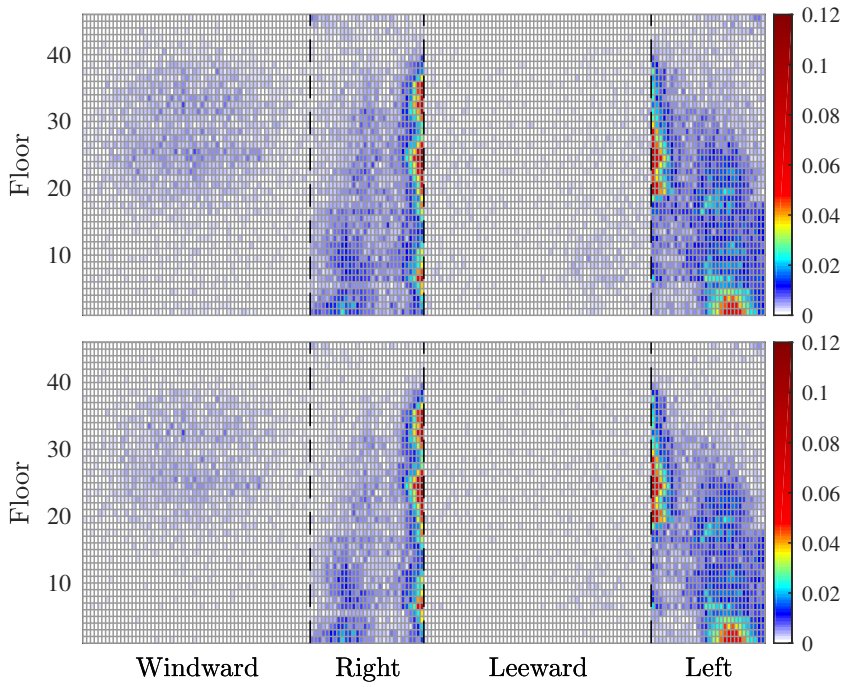

Figure 2.22: Probability of a cladding element assuming as a final damage state $DS^1_{P_{60}}$ top, or $DS^2_{p_{60}}$ bottom.

that can be calibrated, or at least informed, by existing fragility databases and literature results. By taking advantage of how wind driven rain on building envelopes can be effectively estimated through steady-state models, an efficient Monte Carlo simulation framework is proposed for probabilistically estimating the damage to the building envelope, as well as consequent rainwater ingress, for storms of given wind and rain intensity.

To illustrate the framework, a full scale case study is presented consisting of a 45-story steel structure equipped with a cladding system with damageable laminated glass panels. The results of the case study clearly illustrated the progressive time dependent nature of envelope damage and the importance of modeling the interdependencies between demand and damage. The effects of the uncertainties in the system on the final number of damaged components, and consequent ingressed rainwater, was clearly seen and illustrates the need to account for uncertainty when estimating the performance of building envelopes of wind-excited systems. It is believed that the type of results output by the proposed framework, as well as the possibility to deaggregate the results, could be of particular interest to the

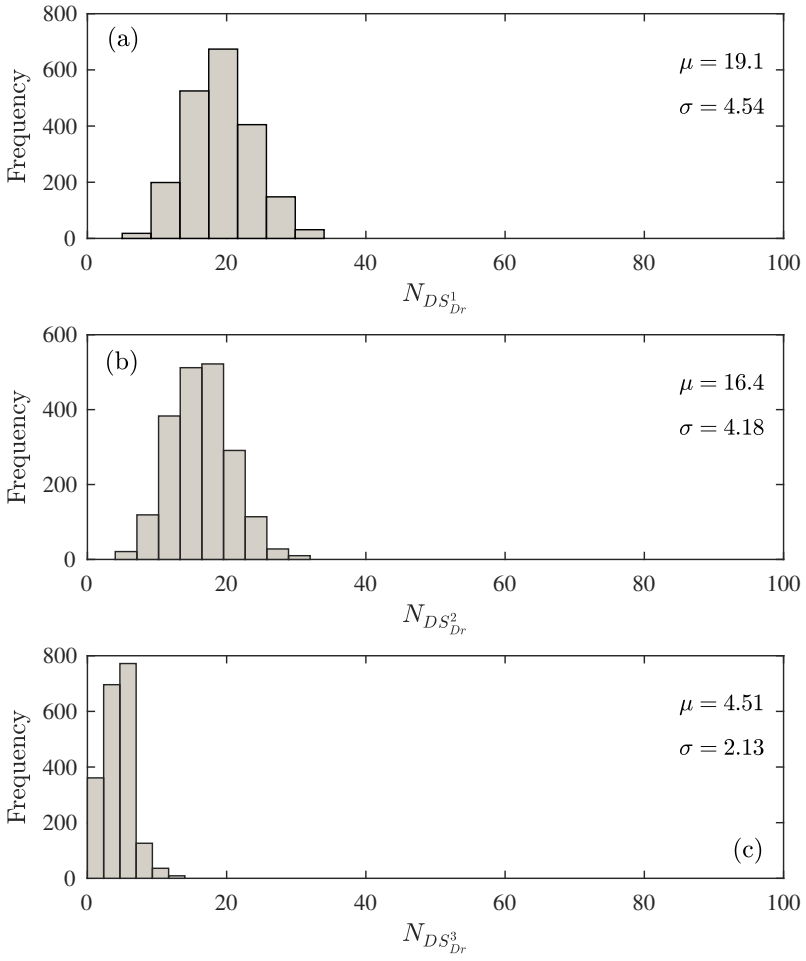

Figure 2.23: Histograms of the total number of cladding elements assuming a final damage state of: (a) DS^1_{Dr}; (b) DS^2_{Dr}; or (b) DS^3_{Dr}.

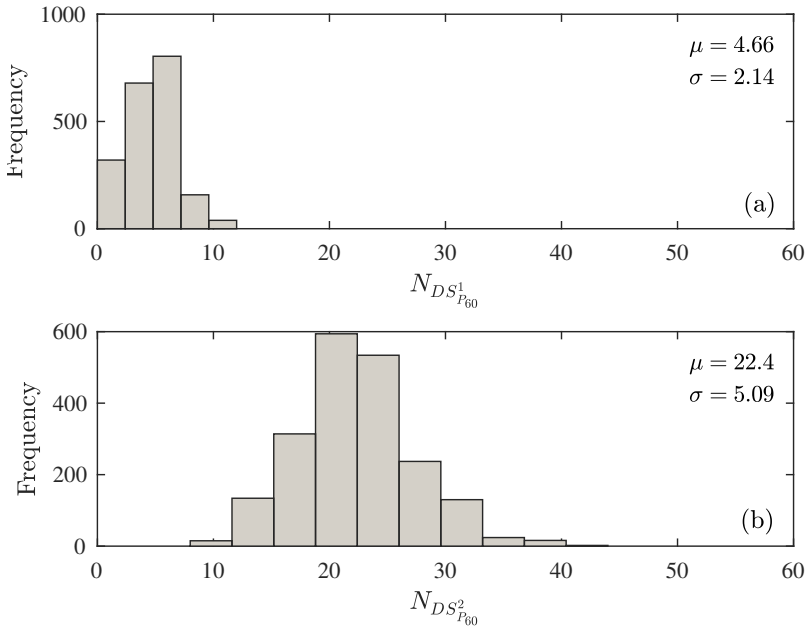

Figure 2.24: Histograms of the total number of cladding elements assuming a final damage state of: (a) $DS^1_{P_{60}}$; or (b) DS^2_{p60}.

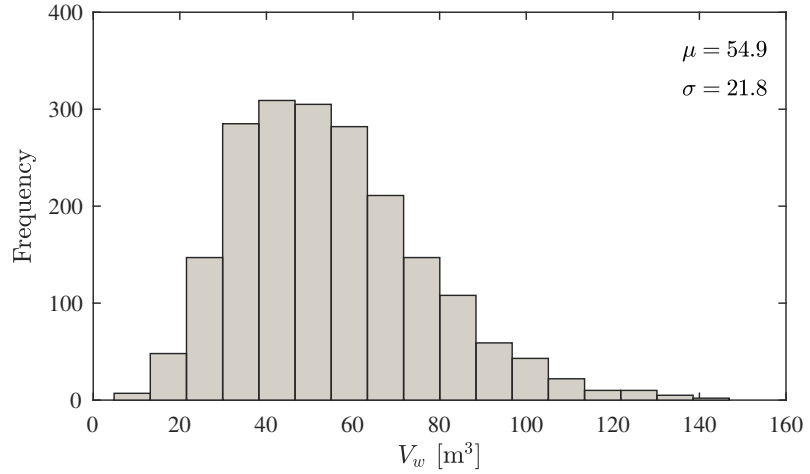

Figure 2.25: Histogram of the total volume of rainwater ingressed into the building during the windstorm.

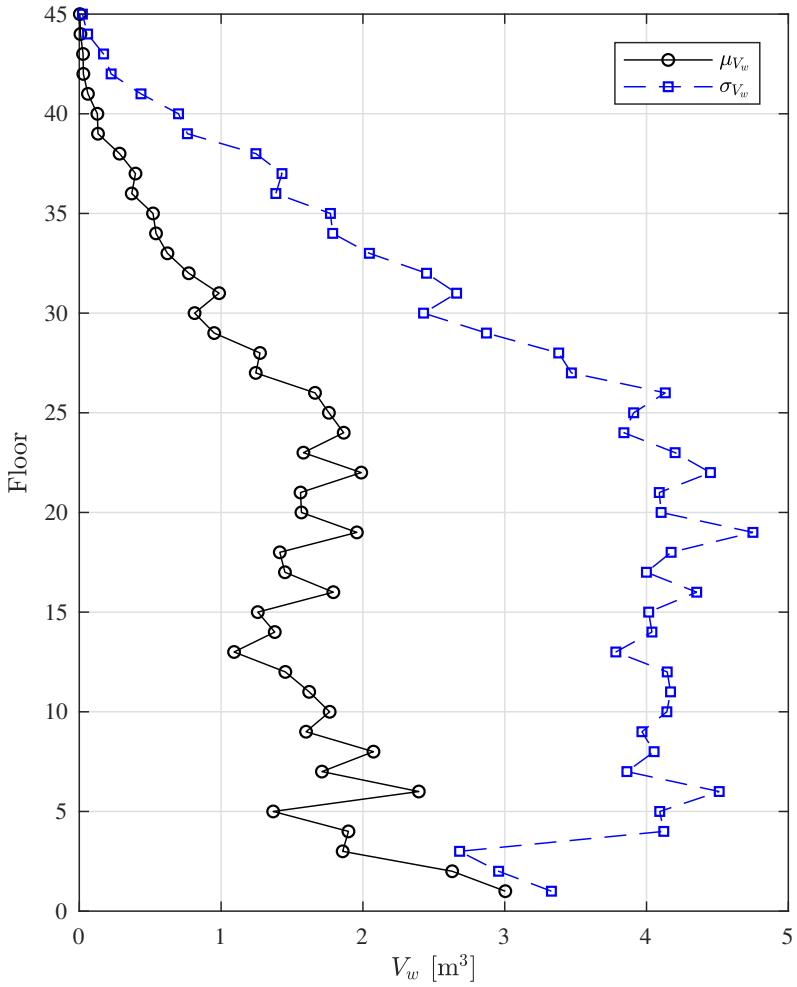

Figure 2.26: Floor by floor deaggregation of the total volume of rainwater entering the building.

Table 2.1: Member section assignments for the steel structure of the case study. W24 sections are identified through their weight per unit length using imperial units. Box sections are identified in terms of their mid-line width in cm.

Group	Floor Number														
Number	1-3	4-6	7-9	10-12	13-15	16-18	19-21	22-24	25-27	28-30	31-33	34-36	37-39	40-42	43-45
B1	176	207	207	207	207	207	192	192	192	162	162	131	104	104	104
B2	207	408	408	450	492	492	450	408	335	408	306	279	176	94	94
B3	492	492	492	492	492	492	492	492	492	492	408	335	229	207	162
B4	492	492	492	492	492	492	492	492	492	492	450	408	279	229	162
B5	207	408	450	408	306	279	279	207	176	146	146	146	146	146	131
B6	492	492	492	492	306	279	250	229	207	192	192	162	146	146	146
B7	146	162	131	131	131	131	162	146	146	146	146	117	103	76	55
C1	55	60	60	60	60	55	55	55	55	50	45	45	45	45	45
C2	60	60	60	60	60	55	55	55	55	50	50	45	45	45	45
C3	60	55	60	60	60	55	55	55	55	55	50	50	45	45	45
C4	65	55	60	60	60	60	60	60	55	55	55	50	45	45	45
C5	65	60	65	60	60	60	60	60	60	60	55	55	45	45	45
C6	70	65	70	65	65	65	60	60	60	60	60	55	50	45	45
C7	75	70	75	70	70	65	65	65	65	60	60	60	50	50	45
C8	215	160	130	115	105	95	85	70	60	65	60	60	55	55	45
C9	110	105	100	105	105	100	95	90	80	70	55	60	60	55	50
C10	110	100	100	100	100	95	95	90	85	80	75	65	65	55	50
C11	135	100	90	90	90	90	85	85	85	80	75	70	60	55	45
C12	75	85	85	85	85	85	85	85	80	75	75	70	65	50	45
C13	65	80	80	80	85	85	85	80	80	75	75	65	65	60	55
C14	80	70	70	70	70	65	65	60	55	50	45	45	45	45	45
C15	80	75	75	75	70	70	65	60	55	50	50	45	45	45	45
C16	195	145	115	105	90	80	70	60	60	55	50	50	45	45	45
C17	95	95	95	90	85	75	75	70	60	50	50	45	45	45	45
C18	80	85	80	80	80	70	70	65	60	60	55	55	50	50	50

designers and analysts of wind-excited engineered structures.

2.7 Acknowledgment

The research effort was supported in part by the National Science Foundation (NSF) under Grant No. CMMI-1562388. This support is gratefully acknowledged.

2.8 Appendices

Appendix A.1. Member sizes for the case study structure

The member assignments for each of the 375 design groups defined in Sec. 4.7.1.1 and Fig. 2.4(b) are reported in Table 2.1. In particular, group B7 of Table 2.1 is associated with the bracings of the left and right face of the building.

Appendix A.2. Stochastic model for the external pressure coefficients

If the common assumption of stationarity and ergodicity of the vector valued stochastic process $\mathbf{C}_{p,e}(t) = \{C_{p,e}^{(1)}(t), ..., C_{p,e}^{(K)}(t)\}^T$ is made, the wind tunnel realization of $\mathbf{C}_{p,e}(t)$ can be used to estimate the spectral proper orthogonal decomposition eigenvalues and eigenvectors of $\mathbf{C}_{p,e}(t)$ through solving the following frequency dependent eigenvalue/eigenvector problem:

$$[\mathbf{S}_{\mathbf{C}_{p,e}}(\omega; \bar{V}_H, \alpha) - \Lambda_i(\omega; \bar{V}_H, \alpha)\mathbf{I}]\mathbf{\Psi}_i(\omega; \alpha) = 0 \tag{2.30}$$

where: ω is the circular frequency, $\mathbf{I}$ is the identity matrix, $\mathbf{S}_{\mathbf{C}_{p,e}}$ is the cross power spectral density matrix of the wind tunnel realization of $\mathbf{C}_{p,e}(t)$, Λ_i and $\mathbf{\Psi}_i$ are the ith frequency dependent eigenvalue and eigenvector of $\mathbf{C}_{p,e}(t)$, while $\bar{V}_H$ and α are the wind speed and direction for which Λ_i and $\mathbf{\Psi}_i$ are estimated. The knowledge of Λ_i and $\mathbf{\Psi}_i$ can be used to decompose $\mathbf{C}_{p,e}(t)$ into N_m independent subprocesses as:

$$\mathbf{C}_{p,e}(t) \approx \tilde{\mathbf{C}}_{p,e}(t) = \sum_{i=1}^{N_m} \tilde{\mathbf{C}}_{p,e}^{(i)}(t) + \bar{\mathbf{C}}_{p,e} \tag{2.31}$$

where $\bar{\mathbf{C}}_{p,e}$ is the mean pressure coefficient (estimated directly from the wind tunnel data), while $\tilde{\mathbf{C}}_{p,e}^{(i)}(t)$ is the ith zero mean subprocesses given by:

$$\tilde{\mathbf{C}}_{p,e}^{(i)}(t) = \sum_{j=0}^{N_\omega - 1} |\mathbf{\Psi}_i(\omega_j)| \sqrt{2\Lambda_i(\omega_j)\Delta\omega} \cos(\omega_j t + \boldsymbol{\vartheta}_j(\omega_j) + \theta_{ij}) \tag{2.32}$$

where $\Delta\omega$ is the frequency increment with a Nyquist (cutoff) frequency $N_i\Delta\omega/2$ with N_ω the total number of discrete frequencies and $\omega_j = j\Delta\omega$; θ_{ij} is an independent random variable characterizing the stochastic nature of the pressure coefficient, uniformly distributed over $[0, 2\pi]$; while $\boldsymbol{\vartheta}_j(\omega_j) = \tan^{-1}(\mathrm{Im}(\mathbf{\Psi}_i(\omega_j))/\mathrm{Re}(\mathbf{\Psi}_i(\omega_j)))$.

To account for the generally non-Gaussian nature of $\mathbf{C}_{p,e}(t)$, a translation model can be

adopted (*Gioffrè and Gusella*, 2007). Under this assumption, the kth component of the vector valued stochastic process $\mathbf{C}_{p,e}(t)$ is modeled as:

$$C_{p,e}^{(k)}(t) = F_{C_{p,e}^{(k)}}^{-1} \left\{ \Phi \left[\frac{\tilde{C}_{p,e}^{(k)}(t) - \mu_{C_{p,e}^{(k)}}}{\sigma_{C_{p,e}^{(k)}}} \right] \right\} \quad \text{for} \quad k = 1, ..., K \tag{2.33}$$

where Φ is the standard normal distribution function, $\mu_{C_{p,e}^{(k)}}$ and $\sigma_{C_{p,e}^{(k)}}$ are the mean and standard deviation of the kth component of $\mathbf{C}_{p,e}(t)$, while $F_{C_{p,e}^{(k)}}$ is the marginal distribution of kth component of $\mathbf{C}_{p,e}(t)$. In particular, the marginal distributions $F_{C_{p,e}^{(k)}}$ can be estimated directly from the wind tunnel data through, for example, kernel density estimation.

CHAPTER III

A Performance-Based Wind Engineering Framework for Envelope Systems of Engineered Buildings Subject to Directional Wind and Rain Hazards[1]

Abstract

The adoption of performance-based wind engineering (PBWE) is rapidly becoming recognized as a fundamental step to reducing the huge economic losses caused by severe windstorms. This has led to the recent introduction of a number of PBWE frameworks for the assessment of engineered building systems such as high-rise structures. While these frameworks have resulted in significant progress towards the efficient and effective estimation of performance within a PBWE setting, there is still a significant lack of frameworks that can holistically model the performance of the envelope system of engineered buildings. Recognizing how accurate prediction of losses occurring during severe windstorms, such as hurricanes, cannot be made without detailed modeling of the losses caused by damage to the envelope system, this paper introduces a new PBWE framework that is focused on the performance assessment of the envelope system. The proposed framework is based on integrating a recently proposed building envelope damage model into a conditional stochastic simulation framework

[1]Ouyang, Z., & Spence, S. M. (2020). A Performance-Based wind engineering framework for envelope systems of engineered buildings subject to directional wind and rain hazards. *Journal of Structural Engineering, 146*, 04020049.

in which the directional wind and concurrent rain hazard is explicitly modeled together with the stochastic nature of the local wind pressure. By incorporating loss models, performance estimates are provided in terms of annual exceedance rates of system-level metrics such as repair costs. A full scale building example is presented to illustrate the practicality of the proposed PBWE framework.

3.1 Introduction

Over the last two decades, a significant amount of research has been focused on the development of performance-based wind engineering (PBWE). This has led to the introduction of a number of frameworks for the implementation of PBWE in the assessment of both engineered building systems (e.g. high-rise buildings) (*Jain et al.*, 2001; *Ciampoli et al.*, 2011; *Smith and Caracoglia*, 2011; *Petrini, F. and Ciampoli, M.*, 2012; *Chuang and Spence*, 2017; *Cui and Caracoglia*, 2018; *Ierimonti et al.*, 2019) as well as non-engineered building systems (e.g. low-rise residential buildings) (*Rosowsky and Ellingwood*, 2002; *Barbato et al.*, 2013; *Baheru et al.*, 2015; *Peng et al.*, 2016; *Unnikrishnan and Barbato*, 2017). While the importance of damage to the building envelope of engineered systems due to local actions has been documented (e.g. *Williams and Kareem*, 2003; *Vega and Koke*, 2008; *Beers*, 2011), the majority of work in the area of PBWE frameworks for engineered systems has focused on describing structural and non-structural performance in terms of the response of the structural system, i.e. damage and losses generated by the action of local wind pressures and debris impact are not generally modeled. Another aspect that is generally ignored is the consequent water ingress through the damaged envelope due to the rain event that often accompanies severe windstorms such as hurricanes and can cause significant losses due to damage to the interior non-structural components of the building. Although recent extensions of the Florida Public Hurricane Loss Model (FPHLM) (*Pita et al.*, 2012) to mid-rise residential buildings have considered, to a certain extent, these aspects (*Pita et al.*, 2016), the intent of the FPHLM is the performance assessment of portfolios containing hundreds of buildings. The detail with

which each building is modeled is not therefore at the level of PBWE where the focus is on the performance assessment of individual buildings. With the aim of beginning to overcome these limitations, the authors have recently introduced a performance-based damage estimation framework for engineered high-rise buildings (*Ouyang and Spence*, 2019). In particular, a model is established in which each component of the envelope system is modeled as susceptible to both drift and pressure induced damage characterized through multiple fragility functions. The progressive and coupled nature of wind damage, as well as potential water ingress, is explicitly modeled by stepping through the wind event and solving at each time step the structural dynamic equilibrium problem, internal/external pressure equilibrium problem, and wind driven rain water ingress problem. This leads to detailed information on the damage status of each envelope component at the end of a wind and concurrent rain event of given intensity.

This work is focused on integrating the aforementioned damage model within a fully PBWE setting in which performance is defined in terms of the mean annual rate of exceeding system-level decision variable thresholds associated with metrics such as repair costs and total water ingress through the damaged building envelope. To this end, a conditional stochastic simulation-based framework is introduced in which directional wind hazard models are integrated with non-Gaussian stochastic models for representing the external wind pressures, computational fluid dynamics (CDF) based directional wind driven rain models for describing the concurrent rain hazard, and consequence models for transforming damages into losses. The performance of a full scale case study consisting of a 45-story building clad with a typical dual-pane envelope system and subject to the directional Miami hurricane and concurrent rain hazard is presented to illustrate the potential of the proposed PBWE framework.

3.2 The performance-based wind engineering setting

A widely accepted framework for performance-based seismic engineering is the methodology developed by the Pacific Earthquake Engineering Research (PEER) Center (*Porter*, 2003). The versatility of this framework has led to its formulation for a number of other hazards, including wind (*Ciampoli et al.*, 2011; *Smith and Caracoglia*, 2011; *Petrini, F. and Ciampoli, M.*, 2012; *Chuang and Spence*, 2017; *Cui and Caracoglia*, 2018). However, with respect to wind hazards, there is still a lack of PBWE frameworks that can handle the coupled and progressive nature of damage to the building envelope as well as the consequent water ingress due to the inevitable concurrent rain event. This work is focused on proposing a PBWE framework to this end that is based on the models recently proposed in (*Ouyang and Spence*, 2019). In particular, following the ideas introduced by the PEER center, the framework is based on describing performance in terms of the mean annual rate, λ, of exceeding a decision variable threshold, dv, associated with performance metrics such as repair costs and water ingress. Within this context, the process of estimating performance can be formulated in terms of the following probabilistic integral:

$$\lambda(dv) = \iiiint G(dv|sm)|\mathrm{d}G(sm|R_T, \alpha, \bar{v}_H)||\mathrm{d}G(R_T|\alpha, \bar{v}_H)||\mathrm{d}G(\alpha|\bar{v}_H)||\mathrm{d}\lambda(\bar{v}_H)| \qquad (3.1)$$

where: $G(dv|sm)$ is the complementary cumulative distribution function (CCDF) of dv conditioned on sm, with sm being a measure of system response (e.g. final damage states at end of the wind event); $\mathrm{d}G(sm|R_T, \alpha, \bar{v}_H)$ is the derivative of the CCDF of the system measure sm conditional on the intensity of the wind event measured through the maximum mean wind speed $\bar{v}_H$ at the building top, the direction of the wind event α, and the maximum intensity of the concurrent rain event R_T; $G(R_T|\alpha, \bar{v}_H)$ is the CCDF of R_T conditioned on $\bar{v}_H$ and α; $G(\alpha|\bar{v}_H)$ is the CCDF of α conditioned on $\bar{v}_H$; while $\lambda(\bar{v}_H)$ is the hazard curve here defined as the mean annual rate of exceeding the $\bar{v}_H$.

In practice, Eq. (3.1) decomposes–through the application of the total probability theorem–

the process of estimating performance of the envelope system into the following fundamental steps:

1. Hazard analysis: in which the terms $G(R_T|\alpha, \bar{v}_H)$, $G(\alpha|\bar{v}_H)$ and $\lambda(\bar{v}_H)$ are estimated for characterizing the intensity of the rain event, the directional effects, and intensity of the wind event.

2. Response analysis: in which the response of the envelope system is characterized for a given event intensity through the estimation of $G(sm|R_T, \alpha, \bar{v}_H)$. In particular, implicit to the estimation of $G(sm|R_T, \alpha, \bar{v}_H)$, is the aerodynamic response of the system.

3. Loss and consequence analysis: in which the system responses, sm, are translated into loss and consequence measures through the estimation of the term $G(dv|sm)$.

By then integrating over all event intensities and system responses through Eq. (3.1), system-level performance estimates of the envelope system are obtained. In the following, analysis models will be presented for estimating each of the terms identified above, as will a stochastic simulation model for efficiently solving the probabilistic integral of Eq. (3.1).

3.3 Hazard analysis

The intensity of a wind event at a location of interest can be characterized from data collected at nearby meteorological stations. To provide statistically meaningful predictions, this data generally requires augmentation through Monte Carlo simulations. Within this context, this work assumes that data is available in terms not only of the maximum wind speeds to occur during a set of historical events, but also of the direction of the event, as well as the intensity of the concurrent rain event. In the following, models will be discussed for calibrating the terms $G(R_T|\alpha, \bar{v}_H)$, $G(\alpha|\bar{v}_H)$ and $\lambda(\bar{v}_H)$ when varying amounts of data is available.

3.3.1 Hazard curve

The overall intensity of the wind event is defined in this work in terms of the following site-specific non-directional hazard curve:

$$\lambda(\bar{v}_H) = \lambda_e(1 - F_{\bar{V}_H}(\bar{v}_H)) \tag{3.2}$$

where λ_e is the arrival rate of the extreme wind events while $F_{\bar{V}_H}$ is the cumulative distribution function (CDF) of the largest wind speeds, irrespective of direction, to occur during a given wind event. While λ_e can be estimated directly from the data collected at the meteorological station, the estimation of the hazard curve of Eq. (3.2) generally requires a transformation of the raw wind speed data. This can be carried out through, for example, the following probabilistic transformation (*Minciarelli et al.*, 2001; *Diniz et al.*, 2004):

$$\bar{v}_H(T, z_0, H) = e_1 e_2 e_3(T, \tau_1) \left(\frac{e_5 z_0}{e_6 z_{01}}\right)^{e_4 \delta} \frac{\ln\left[H/(e_5 z_0)\right]}{\ln\left[H_{met}/(e_6 z_{01})\right]} e_7 \bar{v}_{H_{met}}(\tau_1, z_{01}, H_{met}) \tag{3.3}$$

where: $\bar{v}_{H_{met}}$ is the maximum wind speed to occur at the meteorological station; τ_1 is the averaging time used in generating the data at the meteorological station; H_{met} and z_{01} are the height and roughness length at the meteorological station; T is the averaging time of interest to the performance analysis (e.g. an hour); H is the height to which the data point $\bar{v}_{H_{met}}$ are to be transformed; z_0 is the roughness length at the site of interest; δ is an empirical constant that can be taken as 0.0706; e_1 and e_2 are random variables accounting for the observational and sampling errors in $\bar{v}_{H_{met}}$; e_3 is the conversion factor accounting for the effects of transforming between different averaging times; e_5 and e_6 are random variables modeling the uncertainties in the estimation of the terrain roughness lengths; while e_7 is a random variable modeling the uncertainty in using the model of Eq. (3.3) in the case of hurricane events. A detailed discussion on the transformation of Eq. (3.3) can be found in (*Diniz et al.*, 2004), together with distributions for characterizing the uncertain parameters

e_1 to e_7.

The transformation of Eq. (3.3) allows for the wind speed data collected at the meteorological station to be transformed into site-specific wind speed data. The transformed data can then be used to estimate the marginal distribution, $F_{\bar{V}_H}$, of the site-specific wind speed $\bar{v}_H$ through fitting an appropriate extreme distribution, e.g. a Weibull or Type I distribution. To account for the uncertainty modeled by the parameters e_1 to e_7, the wind speed data, $\bar{v}_{H_{met}}^{(i)}$ for $i = 1, ..., N_{met}$, collected at the meteorological station can be transformed to the site of interest considering a realization of e_1 to e_7. This will result in N_{met} site-specific wind speeds that can be used to estimate (through fitting) the distribution, $\tilde{F}_{\bar{v}_H}$, associated with the realization of e_1 to e_7. By repeating this operation for N_e realizations of e_1 to e_7, the site-specific distribution, $F_{\bar{V}_H}$, can be estimated through expectation as:

$$F_{\bar{V}_H}(\bar{v}_H) = E\big[\tilde{F}_{\bar{v}_H}(\bar{v}_H)\big] = \frac{1}{N_e}\sum_{j=1}^{N_e} \tilde{F}_{\bar{v}_H}^{(j)}(\bar{v}_H) \tag{3.4}$$

where $\tilde{F}_{\bar{v}_H}^{(j)}$ is the distribution associated with the jth realization of e_1 to e_7.

3.3.2 Wind directionality

The direction with which the wind speed $\bar{v}_H$ occurs at the site of interest plays a fundamental role in deciding the aerodynamic response of the system. As outlined in Sec. 5.2, this effect can be modeled through the directional term of Eq. (3.1), which can be estimated from the following site-specific conditional CCDF of the wind direction, α, given the site-specific wind speed $\bar{v}_H$:

$$G(\alpha|\bar{v}_H) = \int_{\alpha}^{+\infty} \frac{f_{\alpha,\bar{v}_H}(\alpha, \bar{v}_H)}{\left.\frac{\mathrm{d}F_{\bar{v}_H}}{\mathrm{d}\bar{v}_H}\right|_{\bar{v}_H}} \mathrm{d}\alpha \tag{3.5}$$

where $f_{\alpha,\bar{v}_H}$ is the joint probability density function (pdf) between the site-specific wind speed and direction. The approach proposed in this work to estimate $f_{\alpha,\bar{v}_H}$ is introduced in the following section. Important simplifications occur if it is assumed that the direction of

the event is independent of the wind speed. In this case, $G(\alpha|\bar{v}_H) = G(\alpha)$, which can be estimated directly by fitting a circular distribution function, e.g. the generalized von Mises or circular kernel density, to the site-specific directional data. Finally, in the case of missing directional wind data, a uniform distribution can be considered for $G(\alpha)$ therefore defining a non-directional wind climate.

3.3.2.1 Bivariate copula

To estimate the joint distribution between the extreme wind speed $\bar{v}_H$ and direction α, the following bivariate copula function can be adopted:

$$f_{\alpha,\bar{v}_H}(\alpha,\bar{v}_H) = c_{\alpha,\bar{v}_H}\left(F_\alpha(\alpha), F_{\bar{v}_H}(\bar{v}_H)\right) \frac{\mathrm{d}F_\alpha}{\mathrm{d}\alpha}\Big|_\alpha \frac{\mathrm{d}F_{\bar{v}_H}}{\mathrm{d}\bar{v}_H}\Big|_{\bar{v}_H} \tag{3.6}$$

where $c_{\alpha,\bar{v}_H}$ is the bivarate copula, $F_{\bar{v}_H}$ is the site-specific distribution function of Eq. (3.4), while $F_\alpha(\alpha)$ is the site-specific marginal distribution function of wind direction. In particular, the estimation of $c_{\alpha,\bar{v}_H}$ and $F_\alpha(\alpha)$ requires the availability of directional wind speed data sets at the meteorological station, i.e. of paired samples of wind speed and direction of the type $\{\bar{v}^{(i)}_{met}, \alpha^{(i)}_{met}\}$. As for the wind speed samples of Sec. 3.3.1, the wind direction samples can be transferred to the site of interest through a probabilistic transformation and used to calibrate the expected site-specific wind direction marginal distribution as: $F_\alpha(\alpha) = E[\tilde{F}_\alpha(\alpha)]$. Similarly, the expected site-specific copula can be expressed as:

$$\begin{aligned} c_{\alpha,\bar{v}_H}\big(F_\alpha(\alpha), F_{\bar{v}_H}(\bar{v}_H)\big) &= E\big[\tilde{c}_{\alpha,\bar{v}_H}\big(\tilde{F}_\alpha(\alpha), \tilde{F}_{\bar{v}_H}(\bar{v}_H)\big)\big] \\ &= \frac{1}{N_e}\sum_{i=1}^{N_e} \tilde{c}^{(i)}_{\alpha,\bar{v}_H}\big(\tilde{F}^{(i)}_\alpha(\alpha), \tilde{F}^{(i)}_{\bar{v}_H}(\bar{v}_H)\big) \end{aligned} \tag{3.7}$$

where $\tilde{c}^{(i)}_{\alpha,\bar{v}_H}$ is the fitted copula density of the ith transformed data point. In general, in choosing an appropriate copula, it should be observed that the dependency between α and $\bar{v}_H$ is nonlinear due to how $\bar{v}_H$ follows an unbounded extreme distribution while α obeys

a circular distribution, i.e. bounded distribution. Thus, popular parametric copulas, such as the Archimedean copulas or the Gaussian copula, are not suitable. For this reason, a nonparametric kernel estimated copula (*Kie et al.*, 2010) is adopted in this work.

3.3.3 Concurrent rainfall intensity

The intensity of the concurrent rain event can be estimated using an analogous approach as outlined above for wind direction. Indeed, if it is assumed that the concurrent rain intensities measured at the meteorological station are representative of the rain intensities at the site of interest, then the term $G(R_T|\alpha, \bar{v}_H)$ of Eq. (3.1) can be estimated from the following conditional CCDF of rain fall intensity given wind direction and speed:

$$G(R_T|\alpha, \bar{v}_H) = \int_{R_T}^{+\infty} \frac{f_{R_T,\alpha,\bar{v}_{H_{met}}}(R_T, \alpha, \bar{v}_{H_{met}})}{f_{\alpha,\bar{v}_{H_{met}}}(\alpha, \bar{v}_{H_{met}})} \mathrm{d}R_T \tag{3.8}$$

where $f_{R_T,\alpha,\bar{v}_{H_{met}}}$ is the joint pdf between the rain fall intensity, wind direction, and speed at the meteorological station. In general, the direct estimation of Eq. (3.8) is not straightforward due to the need to estimate the joint pdfs $f_{R_T,\alpha,\bar{v}_{H_{met}}}$ and $f_{\alpha,\bar{v}_{H_{met}}}$. However, recent studies have indicated that, for data collected for a given location and event type (e.g. hurricanes), the dependency between wind speed/direction and rainfall intensity would seem negligible (*Rappaport*, 1999; *Dong et al.*, 2017). This simplifies the estimation of $G(R_T|\alpha, \bar{v}_H)$, which can now be estimated directly by fitting a univariate CCDF to the concurrent rainfall data collected at the meteorological station.

3.4 Response analysis: envelope actions

As discussed in Sec. 5.2, inherent to the estimation of the system measures (sm) for an event of given intensity is the knowledge of envelope actions, i.e. the external dynamic wind pressure and deposit of wind-driven rain on the building envelope for a given wind speed, direction and concurrent rainfall intensity.

3.4.1 External pressure coefficients

To characterize the external wind pressures, wind tunnel tests can be carried out. These generally consist in simultaneously measuring pressures at a number of taps located on the surface of a rigid scale model of the building. These pressures can be used to estimate an experimental realization of the vector collecting the external dynamic pressure coefficients at the tap locations, indicated in the following as $\mathbf{C}_{p,e}(t)$. Time/frequency scaling of $\mathbf{C}_{p,e}(t)$ can then be achieved through imposing similitude between the Strouhal number at model and full scale.

Under the common assumption of stationarity and ergodicity of the vector-valued stochastic process $\mathbf{C}_{p,e}(t)$, the wind tunnel realization of $\mathbf{C}_{p,e}(t)$ can be used to calibrate an appropriate non-Gaussian stochastic simulation model. To this end, a translation model is considered in this work. The model is based on first approximating $\mathbf{C}_{p,e}(t)$ through a Gaussian process, $\mathbf{C}_{p,e}^{\mathcal{GP}}(t)$, whose second order properties match those of the original process, and, secondly, using $\mathbf{C}_{p,e}^{\mathcal{GP}}(t)$ as input to a translation process whose marginal distributions match those of the non-Gaussian process $\mathbf{C}_{p,e}(t)$.

To simulate random realizations of $\mathbf{C}_{p,e}^{\mathcal{GP}}(t)$, a proper orthogonal decomposition (POD) based spectral representation model is adopted (*Chen and Letchford*, 2005; *Peng et al.*, 2017). In particular, to estimate the frequency dependent eigenvalues and eigenvectors of $\mathbf{C}_{p,e}(t)$, the following spectral eigenvalue problem can be solved:

$$[\mathbf{S}_{\mathbf{C}_{p,e}}(\omega;\alpha) - \Lambda_i(\omega;\alpha)\mathbf{I}]\mathbf{\Psi}_i(\omega;\alpha) = 0 \tag{3.9}$$

where ω is the circular frequency, $\mathbf{I}$ is the identity matrix, $\mathbf{S}_{\mathbf{C}_{p,e}}$ is the double-sided cross power spectral density matrix estimated from the wind tunnel realization of $\mathbf{C}_{p,e}(t)$, while Λ_i and $\mathbf{\Psi}_i$ are the ith frequency dependent eigenvalue and eigenvector of $\mathbf{C}_{p,e}(t)$. The knowledge

of Λ_i and $\mathbf{\Psi}_i$ can be used to give $\mathbf{C}_{p,e}^{\mathcal{GP}}(t)$ the following truncated representation of order N_m:

$$\mathbf{C}_{p,e}^{\mathcal{GP}}(t) \approx \tilde{\mathbf{C}}_{p,e}^{\mathcal{GP}}(t) = \bar{\mathbf{C}}_{p,e} + \sum_{i=1}^{N_m} \tilde{\mathbf{C}}_{p,e}^{(i)}(t) \tag{3.10}$$

where $\bar{\mathbf{C}}_{p,e}$ is the mean pressure coefficient (estimated directly from the wind tunnel data), while $\tilde{\mathbf{C}}_{p,e}^{(i)}(t)$ are N_m zero mean independent subprocesses which can be given the following spectral representation:

$$\tilde{\mathbf{C}}_{p,e}^{(i)}(t) = \sum_{j=0}^{N_\omega - 1} 2|\mathbf{\Psi}_i(\omega_j)|\sqrt{\Lambda_i(\omega_j)\Delta\omega}\cos(\omega_j t + \boldsymbol{\vartheta}_j(\omega_j) + \theta_{ij}) \tag{3.11}$$

where: $\Delta\omega$ is the frequency increment with $\omega_j = j\Delta\omega$; N_ω is the total number of discrete frequencies therefore leading to a Nyquist (cutoff) frequency of $N_\omega\Delta\omega/2$; θ_{ij} is an independent random variable characterizing the stochastic nature of the pressure coefficients and uniformly distributed over $[0, 2\pi]$; while $\boldsymbol{\vartheta}_j(\omega_j) = \tan^{-1}(\mathrm{Im}(\mathbf{\Psi}_i(\omega_j))/\mathrm{Re}(\mathbf{\Psi}_i(\omega_j)))$.

To capture the non-Gaussian nature of $\mathbf{C}_{p,e}(t)$, the Gaussian process $\tilde{\mathbf{C}}_{p,e}(t)$ can be used as input to a translation model (*Gioffrè et al.*, 2001; *Liu et al.*, 2017). Under this assumption, the nth component of $\mathbf{C}_{p,e}(t)$ is given by:

$$C_{p,e}^{(n)}(t;\alpha) = F_{C_{p,e}^{(n)}}^{-1}\left\{\Phi\left[\frac{\tilde{C}_{p,e}^{\mathcal{GP}(n)}(t;\alpha) - \mu_{C_{p,e}^{(n)}}(\alpha)}{\sigma_{C_{p,e}^{(n)}}(\alpha)}\right]\right\} \tag{3.12}$$

where Φ is the standard normal distribution function, $\mu_{C_{p,e}^{(n)}}$ and $\sigma_{C_{p,e}^{(n)}}$ are the mean and standard deviation of $C_{p,e}^{(n)}(t)$ while $F_{C_{p,e}^{(n)}}$ is the corresponding non-Gaussian marginal distribution. To estimate $F_{C_{p,e}^{(n)}}$, the wind tunnel data can be used to calibrate a kernel-Pareto mixture model (*Zhao et al.*, 2019). In this approach, the possible values that can be assumed by $C_{p,e}^{(n)}$ are divided into the following mutually exclusive regions: 1) a lower tail region, defined as $C_{p,e}^{(n)} \leq v_l$ with v_l the lower tail threshold; 2) a central region, defined as $v_l < C_{p,e}^{(n)} < v_u$ with v_u the upper tail threshold; and 3) an upper tail region, defined as $C_{p,e}^{(n)} \geq v_u$. By recognizing that the majority of of the experimental data will be in the central region, the marginal

distribution function is fitted here using kernel density. By then observing how the tail regions are populated by extreme values, the marginal distribution functions of these regions are assumed to follow an extreme Pareto distribution. Within this context, the following mixture model can be defined for the pdf of $C_{p,e}^{(n)}$:

$$f_{C_{p,e}^{(n)}}(C_{p,e}^{(n)}) = 1_{\{C_{p,e}^{(n)} \leq v_l\}} f_{P,l}(C_{p,e}^{(n)}) + 1_{\{v_l < C_{p,e}^{(n)} < v_u\}} f_{kde}(C_{p,e}^{(n)}) + 1_{\{C_{p,e}^{(n)} \geq v_u\}} f_{P,u}(C_{p,e}^{(n)}) \tag{3.13}$$

where $1_{\{*\}}$ is the indicator function, $f_{P,l}$ and $f_{P,u}$ are the Pareto fitted pdfs at the lower and upper tails, while f_{kde} is the estimated kernel density in the middle region. As outlined in (*Zhao et al.*, 2019), this model not only is well suited for capturing the generally non-Gaussian features seen in pressure coefficients, but can also be calibrated (including the identification of the bounds v_l and v_u) in a semi-automated fashion directly from classic wind tunnel data.

The representation of $\mathbf{C}_{p,e}(t)$ defined by Eqs. (3.10) to (3.13) is convenient from a simulation standpoint as: 1) the subprocesses of Eq. (3.11) are independent and can therefore be simulated individually using efficient algorithms based on the Fast Fourier Transform (*Deodatis*, 1996); and 2) only the first few subprocesses are generally required for accurately representing $\mathbf{C}_{p,e}(t)$.

3.4.2 Wind driven rain

For a given hazard intensity, and so wind speed $\bar{v}_H$, direction α and concurrent rainfall intensity R_T, the spatial distribution of the steady state turbulent dispersed wind driven rain on the building envelope can be numerically estimated through a Reynolds-averaged Navier-Stokes (RANS) based CFD multiphase model (*Huang and Li*, 2010; *Kubilay et al.*, 2015a, 2017). In particular, an approach of this type involves two steps. In the first step, the time-averaged wind field, $\mathbf{U}_w(x, y, z)$, is estimated in a computational domain around the building through solving the RANS equations with appropriate turbulence model (e.g.

realizable $k-\epsilon$), and therefore as:

$$\mathbf{U}_w(x,y,z) = \mathcal{CFD}_{wind}\left(\bar{v}_H, z_0, \alpha\right) \tag{3.14}$$

where, in writing Eq. (3.14), the dependency of the simulation on the wind speed $\bar{v}_H$, direction α, site roughness length z_0 has been explicitly highlighted. Based on the simulated wind field $\mathbf{U}_w$, the wind driven rain field can then be modeled in a second step through a Eulerian multiphase framework. In this approach, the rain field is decomposed into N_{wdr} rain phases, i.e. divided into N_{wdr} non-overlapping intervals based on the raindrop diameter sizes d_k for $k = 1, ..., N_{wdr}$. For each rain phase and point on the envelope ξ_{xyz}, the following normalized specific catch ratios $\bar{\eta}_k$ can be defined:

$$\bar{\eta}_k(\xi_{xyz}) = \frac{|\mathbf{v}_{n,k}(\xi_{xyz}, \mathbf{U}_w)|}{v_{t,k}} \bar{\alpha}_k(\xi_{xyz}, \mathbf{U}_w) \tag{3.15}$$

where $|\mathbf{v}_{n,k}|$ is the velocity magnitude of the kth rain phase in the direction normal to the building envelope, $v_{t,k}$ is the terminal velocity of the raindrops of diameter d_k, while $\bar{\alpha}_k$ is the local volume fraction normalized by considering all rain drops belonging to the kth rain phase, i.e. a unit volume fraction is considered for the kth rain phase.

To estimate Eq. (3.15) in a steady state, the computational domain developed for the simulation of the $\mathbf{U}_w$ can be reused while capturing the turbulent dispersion of the rain phases through the models outlined in (*Kubilay et al.*, 2015a, 2017). In particular, from a computational standpoint, it is important to observe that Eq. (3.15) can be solved simultaneously for all rain phases therefore yielding the following vector of normalized specific catch ratios: $\bar{\boldsymbol{\eta}}(\xi_{xyz}) = \{\bar{\eta}_1(\xi_{xyz}), ..., \bar{\eta}_k(\xi_{xyz}), ..., \bar{\eta}_{N_{wdr}}(\xi_{xyz})\}^T$. From the knowledge of $\bar{\boldsymbol{\eta}}$, the impinging wind driven rain intensity R_{wdr} at each point of the envelope can be estimated for a given horizontal rainfall intensity and R_T and associated horizontal raindrop size distribution,

$f_h(d|R_T)$, through the transformation:

$$R_{wdr}(\xi_{xyz}; R_T, \bar{v}_H, \alpha) = \boldsymbol{\phi}^T(R_T)\bar{\boldsymbol{\eta}}(\xi_{xyz}; \bar{v}_H, \alpha) \tag{3.16}$$

where $\boldsymbol{\phi}$ is a weighting vector estimated from $f_h(d|R_T)$ as:

$$\boldsymbol{\phi}(R_T) = R_T \cdot \begin{bmatrix} \Delta d_1 & 0 & \dots & 0 \\ 0 & \Delta d_2 & \dots & 0 \\ \vdots & \vdots & \ddots & \vdots \\ 0 & 0 & \dots & \Delta d_{N_{wdr}} \end{bmatrix} \begin{Bmatrix} f_h(d_1|R_T) \\ f_h(d_2|R_T) \\ \vdots \\ f_h(d_{N_{wdr}}|R_T) \end{Bmatrix} \tag{3.17}$$

where Δd_k is the discrete diameter range associated with the kth rain phase. In particular, $f_h(d_k|R_T)$ is often given the following form (*Best*, 1950):

$$f_h(d_k|R_T) = \frac{n d_k^{n-1}}{a^n} \exp\left(-\frac{d_k^n}{a^n}\right) \tag{3.18}$$

where n and a are model parameters with a generally depending on the horizontal rainfall intensity R_T.

Before closing this section, it is important to observe for the developments of Sec. 4.6 that $\bar{\boldsymbol{\eta}}$ depends only on $\bar{v}_H$ and α, and not R_T or $f_h(d|R_T)$. Therefore, as long as $\bar{v}_H$ and α are held constant, the evaluation of R_{wdr} can be rapidly updated for any rainfall intensity of interest. For problems involving changes in $\bar{v}_H$ and α, i.e. the problems of Sec. 4.6, it should be observed that the effects of these changes can be efficiently treated through interpolating $\bar{\boldsymbol{\eta}}$ for a limited number of predefined wind directions and speeds. The effectiveness of interpolation for estimating steady state wind driven rain fields on bluff bodies for different wind speeds and directions has been demonstrated in (*Kubilay et al.*, 2014, 2015a, 2017).

3.5 Response analysis: system measures

The knowledge of the envelope actions (i.e. external pressures and wind driven rain) for a given hazard intensity (i.e. wind speed $\bar{v}_H$, direction α and concurrent rainfall intensity

R_T), enables the use of the models outlined in (*Ouyang and Spence*, 2019) to estimate the following system measures:

1. Final damage states of all damageable envelope components;

2. Total volume of water to ingress at each damaged component.

In particular, the use of the models described in (*Ouyang and Spence*, 2019) ensures that the progressive and coupled nature of wind induced envelope damage is fully captured. The rest of this section will provide a brief overview of the models and damage philosophy introduced in (*Ouyang and Spence*, 2019) and used in this work.

3.5.1 Demands

Each damageable envelope component will be subject to demands in the form of local net pressure, interstory drift ratio and depositation of rain water that can enter through the envelope component in the case of damage. In the following, models will be outlined for estimating these demands for a wind event of given intensity.

3.5.1.1 Pressure

In general, each envelope component will be subject to the following local dynamic pressure:

$$p_n(t;\bar{\xi}_{xyz}) = \frac{1}{2}\rho\bar{v}_H^2\left[C_{p,e}(t;\bar{\xi}_{xyz}) - C_{p,i}(t;\bar{\xi}_{xyz})\right] \tag{3.19}$$

where p_n is the dynamic net pressure acting at the centroid, $\bar{\xi}_{xyz}$, of the envelope component, $C_{p,e}$ is the external time varying pressure coefficient at $\bar{\xi}_{xyz}$ (estimated from the external coefficients of Sec. 3.4.1 through interpolation), ρ is the air density, while $C_{p,i}(t)$ is the dynamic time varying internal pressure coefficient at $\bar{\xi}_{xyz}$. As outlined in (*Ouyang and Spence*, 2019), for general layout of interconnected compartments, $C_{p,i}(t)$ can be estimated by modeling the transient air flow at each opening (including the internal openings) through the unsteady-isentropic form of the Bernoulli equation (*Vickery and Bloxham*, 1992; *Guha*

et al., 2011). This leads to a set of non-linear equations that can be efficiently solved at each time step through a 4th order Runge-Kutta scheme. The fundamental aspect to observe is that at each time step the current damage status, i.e. opening status, of all damageable envelope components is required in order to model the air flow at each opening. This couples the damage analysis with the net pressure demand analysis.

3.5.1.2 Drift

Envelope components of multi-story buildings are, in general, susceptible not only to net pressure but also dynamic interstory drift ratio, $Dr(t;\bar{\xi}_{xyz})$. The estimation of this demand parameter can be carried out through solving the dynamic equilibrium equations of the structural system. In particular, because wind excited structural systems are generally designed to remain elastic for wind effects with mean recurrence intervals (MRIs) between 1700 and 3000 years, it is here assumed that the dynamic interstory drift, $Dr(t;\bar{\xi}_{xyz})$, can be estimated from solving a classic linear elastic dynamic equilibrium problem through, for example, the integration of the generalized model coordinates.

3.5.1.3 Rain water depositation

Given a wind direction and rainfall intensity R_T, the demand on each envelope component in terms of rain water depositation can be estimated as the sum of the directly impinging rain water, estimated from $R_{wdr}(\xi_{xyz})$, and the water runoff coming from the stream of water directly above the envelope component. In particular, consistently with $R_{wdr}(\xi_{xyz})$, this last can be estimated from the steady-state rainwater runoff model outlined in (*Ouyang and Spence*, 2019). It is important to observe that, as in the case of the pressure demands of Sec. 3.5.1.1, the rain water depositation demand is in general dependent on the current damage state of the building envelope. Indeed, for any given envelope component, the loss of another component can alter the length of the runoff stream directly above the component under consideration therefore altering the rain water depositation demand.

3.5.2 System measures

To estimate the final damage state, and potential water ingress, for each envelope component during a wind event of given intensity, a progressive damage model is required that accounts not only for the interdependencies outlined in Sec. 3.5.1.1 between demands and damage, but also the coupling that will in general exist between the occurrence of, for example, a drift induced damage state and the capacity of the component to resist local wind pressure. Following the framework outlined in (*Ouyang and Spence*, 2019),the susceptibility to pressure and drift induced damage of each component is modeled through two sets of sequential damage thresholds: $\mathbf{C}_{Dr} = \{C_{Dr_1} \leq C_{Dr_1} \leq ... \leq C_{Dr_{N_{Dr}}}\}$ and $\mathbf{C}_p = \{C_{p_1} \leq C_{p_1} \leq ... \leq C_{Dr_{N_p}}\}$ where N_{Dr} and N_p are the total number of possible pressure and drift damage states for the component. The exceedance of any one of the damage thresholds during the wind event indicates the occurrence of the associated damage state. To ensure a sequential damage logic (i.e. the occurrence of a given damage state implies that all less severe damage states have occurred), the damage state associated with the largest damage threshold to be exceeded at any given time during the event is identified as the current damage state for the component. The uncertainty in the thresholds is modeled through corresponding sets of sequential fragility functions while coupling between the pressure and drift damage states is modeled by degenerating, upon, for example, the occurrence of a drift damage state, the set of pressure thresholds or vice versa. Following this damage philosophy, Fig. 3.1 reports the time stepping progressive damage algorithm adopted in this work for estimating the alphanumeric vector, **DS**, of final damage states together with the vector, $\mathbf{V}_w$, of associated total water ingress.

3.6 Loss and consequence analysis

To convert the final damage states of the system measure, **DS**, into losses measured in terms of repair costs (or time), the concept of unit loss function (ULF) can be used

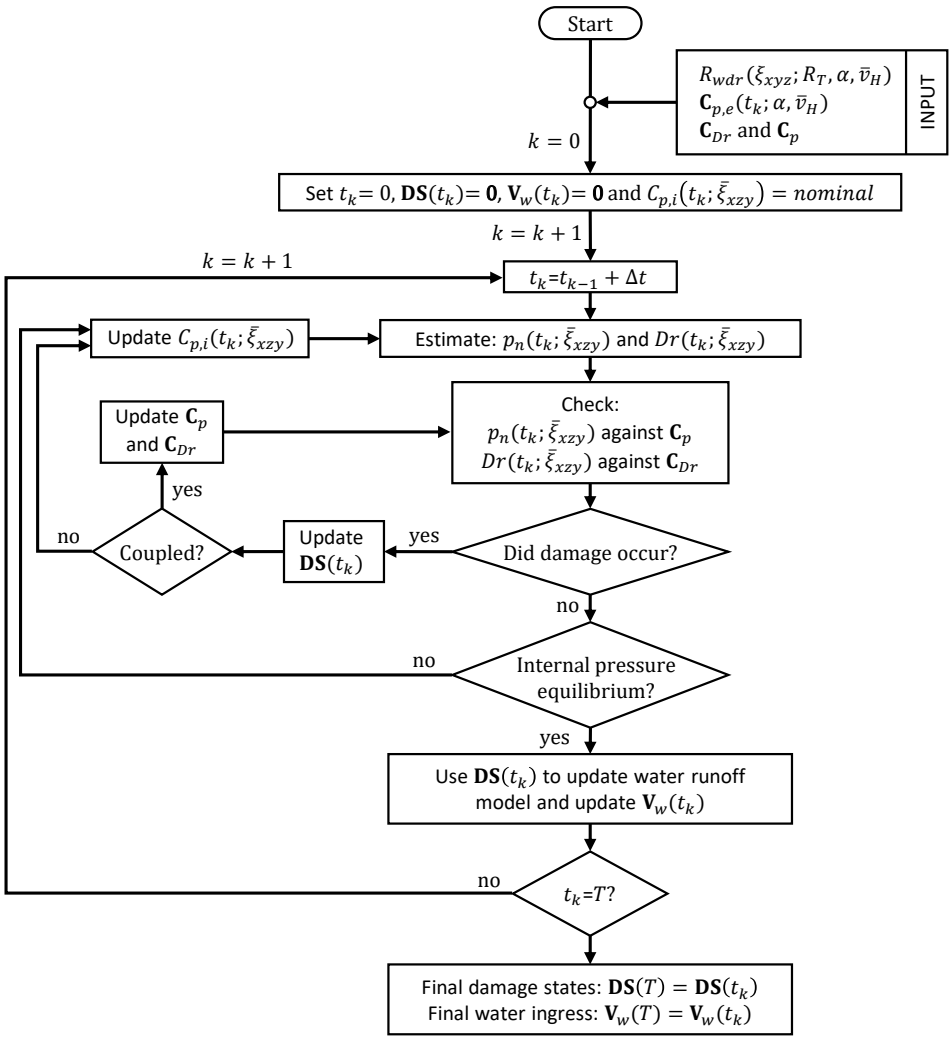

Figure 3.1: Flowchart of the progressive damage algorithm.

where, following the definition outlined in (*Federal Emergency Management Agency (FEMA)*, 2012b), a ULF is defined as a function that relates the cost (or time) necessary to restore a component in a given damage state to its pre-hazard condition. To include the economies scale (i.e. unit discounts that will in general occur due to efficiencies in construction operation when the same damage state is repaired multiple times), ULFs are generally defined as monotonically decreasing functions with respect to the quantity of components to be repaired, where a minimum quantity $Q_{\min}$ is specified as the lower bound, below which no scale effect would exist, and a maximum quantity $Q_{\max}$ as the upper bound, above which no increase in the scale effect would be considered. To include uncertainty, each ULF can be taken as the

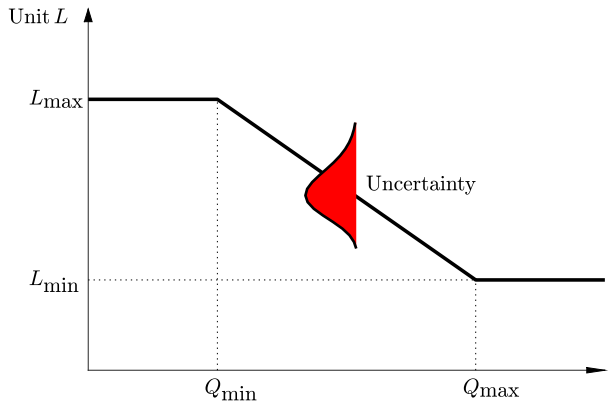

Figure 3.2: Example of an uncertain ULF.

expected (or median) unit loss with uncertainty modeled by including a measure of dispersion with associated distribution (e.g. log-normal). The general form of a typical uncertain ULF is illustrated in Fig. 3.2, where $L_{\min}$ and $L_{\max}$ denote the minimum and the maximum unit loss.

Once the ULFs are defined for each damage state of each damageable envelope component, the translation of the system measure, **DS**, into losses is straightforward. In particular, if the decision variable (dv) of interest is the system-level loss, it is simply necessary to sum the component losses while, if dv is repair time, the schemes outlined in (*Federal Emergency Management Agency (FEMA)*, 2012b) can be directly adopted. Together with losses, it is often of interest to estimate dvs that are related to the consequences of envelope damage. A common example of this type of dv is total system-level water ingress, which can be estimated by directly summing the elements of the system measure $\mathbf{V}_w$.

3.7 Stochastic simulation strategy

3.7.1 Preamble

The ultimate goal of this work is to solve the integral of Eq. (3.1) and therefore describe the performance of the envelope system in terms of the annual rate of exceeding threshold values of the system-level decision variables dv. From a theoretical standpoint, this could be

achieved through Monte Carlo simulation. However, while direct, an approach of this type would fast become computationally unfeasible due to the need to repeatedly evaluate R_{wdr} through the CFD-based models of Sec. 5.4.2 as well as the system measures, **DS** and $\mathbf{V}_w$, through the models of Sec. 3.5. This is especially true if it is kept in mind that the rates, $\lambda(dv)$, of interest to decision makers are in the tails of the distributions, i.e. are associated with rare events, and would therefore require very large sample sizes to be used if reasonable accuracy is to be achieved in the estimates of $\lambda(dv)$.

3.7.2 Proposed algorithm

With the aim of defining a stochastic simulation scheme to overcome the difficulties outlined above, a conditional simulation strategy is developed in this section. In particular, the approach is based on partitioning the sample space of $\bar{v}_H$ into a set of $N_{\bar{v}_H}$ mutually exclusive and collectively exhaustive events $E_{\bar{v}_{H,k}}$ for $k = 1, ..., N_{\bar{v}_H}$. Through the law of total probability, Eq. (3.1) can then be written as follows:

$$\lambda(dv) = \lambda_e \sum_{k=1}^{N_{\bar{v}_H}} \Bigg[\iiint G(dv|sm)|\mathrm{d}G(sm|R_T, \alpha, E_{\bar{v}_{H,k}})| \cdot |\mathrm{d}G(R_T|\alpha, E_{\bar{v}_{H,k}})||\mathrm{d}G(\alpha|E_{\bar{v}_{H,k}})| \Bigg] P(E_{\bar{v}_{H,k}}) \tag{3.20}$$

where $E_{\bar{v}_{H,k}}$ is the kth event defined as $\bar{v}_H \in [\bar{v}^L_{H,k}, \bar{v}^U_{H,k})$ with $\bar{v}^L_{H,k}$ and $\bar{v}^U_{H,k}$ the lower and upper bound wind speed of the kth event, while $P(E_{\bar{v}_{H,k}})$ is the probability of $E_{\bar{v}_{H,k}}$ that can be directly estimated from $F_{\bar{V}_H}$. To ensure $E_{\bar{v}_{H,k}}$ defines a mutually exclusive partition of the sample space of $\bar{v}_H$, the upper bound defining the kth event is taken as the lower bound defining the $(k+1)$th event. To ensure the collectively exhaustive nature of the partition, the lower bound of the first event, $E_{\bar{v}_{H,1}}$, is taken as zero while the last event, $E_{\bar{v}_{H,N_{\bar{v}_H}}}$, is taken as unbounded.

Through the partitioning of Eq. (3.20), the problem becomes one of estimating the term in square brackets that can be recognized as the conditional exceedance probability $G(dv|E_{\bar{v}_{H,k}})$.

In particular, $G(dv|E_{\bar{v}_{H,k}})$ can be efficiently estimated through Monte Carlo simulation as:

$$G(dv|E_{\bar{v}_{H,k}}) \approx \frac{1}{N_k} \sum_{m=1}^{N_k} 1_{\{dv^{(m)} \geq dv|E_{\bar{v}_{H,k}}\}} \tag{3.21}$$

where N_k is the number of samples used to estimate $G(dv|E_{\bar{v}_{H,k}})$ while $1_{\{*\}}$ is the indicator function. To ensure greater accuracy in the estimation of rates associated with rare events when using Eq. (3.21) with a constant N_k, it can be observed that wind pressure, and therefore wind force, is closely related to the square of wind speed. Therefore, the intervals associated with each event, $E_{\bar{v}_{H,k}}$, can be defined by imposing an equal squared wind velocity difference. This results in smaller wind speed intervals in the tail regions of the hazard curve.

The computational effort necessary to estimate Eq. (3.20) through solving $N_{\bar{v}_H}$ problems of the type shown in Eq. (3.21) is considerably reduced as compared to direct MC simulation, as the conditioning on $E_{\bar{v}_{H,k}}$ ensures that: 1) the samples used to estimate $\lambda(dv)$ are evenly spread between frequent and rare events, therefore avoiding the need to generate extremely large sample sets in order to adequately sample the space of rare events; and 2) R_{wdr} can be evaluated for each event $E_{\bar{v}_{H,k}}$ through interpolation of a limited set of precalculated vectors of normalized specific catch ratios.

3.8 Case study

3.8.1 Building system

3.8.1.1 Structural system

A 45-story steel building located in Miami Florida was considered as a case study to illustrate the proposed framework. The layout of the structural system is shown in Fig. 5.2(a). The beams and columns are grouped in plan as shown in Fig. 5.2(b), with each group spanning three consecutive floors of height 4 m. The diagonal braces are grouped as pairs over the height of the building. The beams and bracing elements are assigned sections

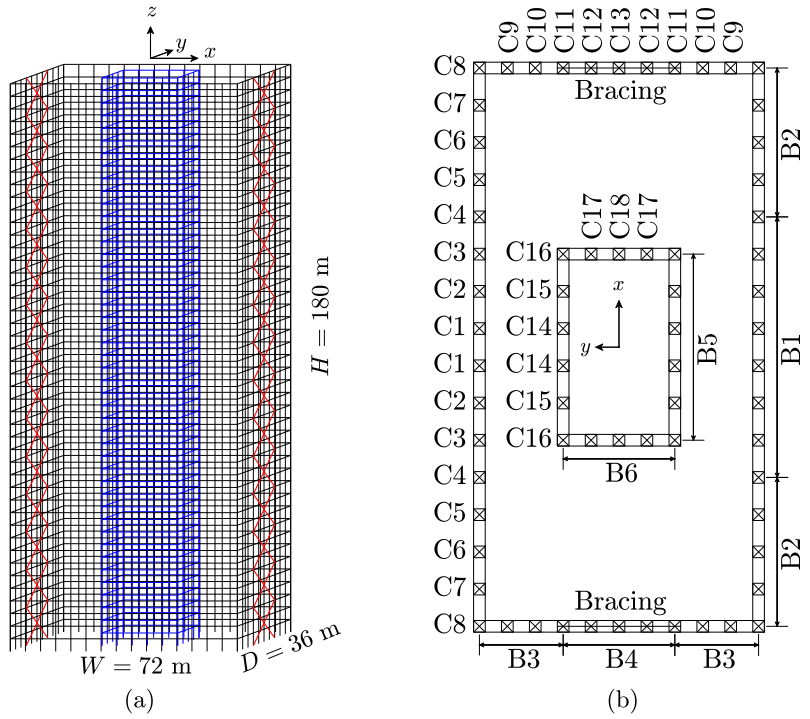

Figure 3.3: (a) 3D illustration of the structural system of the 45-story building; (b) Member layout for a typical floor (B = beam, C = Column).

from the W24 AISC (American Institute for Steel Construction) family while the columns are box sections with wall thickness taken as 1/20 of the mid-line diameter of the section. Each floor was considered rigid in its plane with a mass density of 0.38 t/m^2. The first three circular natural frequencies were estimated to be 1.30 rad/s, 1.67 rad/s and 2.70 rad/s. The first 10 modes were considered sufficient for describing the dynamic response of the building. The modal damping ratios were taken as log-normal random variables with mean 0.014 and coefficient of variation 0.3. To assign the member sizes, the system was designed to meet a 1/400 interstory drift ratio (evaluated at the corners of the building) under a 50-year mean recurrence interval (MRI) wind speed of $\bar{v}_H = 43.9$ m/s (estimated from the hazard curve of Sec. 3.8.2.1) blowing down the x or y direction. Demand to capacity ratios for all members were also limited to unity for a 1700-year MRI wind of $\bar{v}_H = 56.70$ m/s blowing down the x or y direction.

3.8.1.2 Envelope system

In this case study, the vulnerable components of the cladding system are taken as the glazing units. In particular, each unit has a 1.2 m × 2 m vulnerable dual-pane laminated glass panel. Both the inner and outer glass panes of the panel have a thickness of 6 mm. The layout of the glazing units is illustrated in Fig. 3.4, where each unit is positioned 0.5 m below the upper floor and 1.5 m above the lower floor. In total, 8100 units define the building envelope, with 2700 units belonging to each x direction face and 1350 belonging to each y direction face. Each unit is considered to be susceptible to two drift induced damage states corresponding to the glass hairline cracking and glass cracking. Table 3.1 reports the fragility functions, derived from the FEMA P-58 guidelines (*Federal Emergency Management Agency (FEMA)*, 2012b), associated with the two damage states. Each unit was also considered susceptible to glass blowout due to excessive equivalent pressure defined as (*Beason and Morgan*, 1984):

$$p_{eq}(t;\bar{\xi}_{xyz}) = \left(\frac{1}{t_{eq}}\int_0^t [p_n(t;\bar{\xi}_{xyz})]^s\right)^{\frac{1}{s}} \tag{3.22}$$

where t_{eq} is the reference duration, i.e. 3 s or 60 s, while s is an empirical constant. As commonly assumed (e.g. *ASTM E1300-16*, 2016), the two panes of glass are considered to resist p_{eq} through a parallel mechanism. Therefore, each glass pane takes 50% of p_{eq}. The capacity of both panes of glass to blowout are considered fully correlated and described by the fragility function of Table 3.1 that was based on the experimental data reported in (*Behr et al.*, 1991). Damage state DS_{p60} is considered terminal for the glazing unit while the occurrence of DS_{Dr_1} and DS_{Dr_2} are considered to result in a mean reduction in the capacity of the unit to resist p_{60} of 10% and 80% respectively, i.e. DS_{Dr_1} and DS_{Dr_2} are considered coupled with DS_{p60}. To model uncertainty, both reductions were considered to have a coefficient of variation of 0.1 and be described by a truncated normal distribution of support [0,1]. In translating damage into losses, all three damage states were considered to require the replacement of the glass panel. Therefore a single consequence, derived from

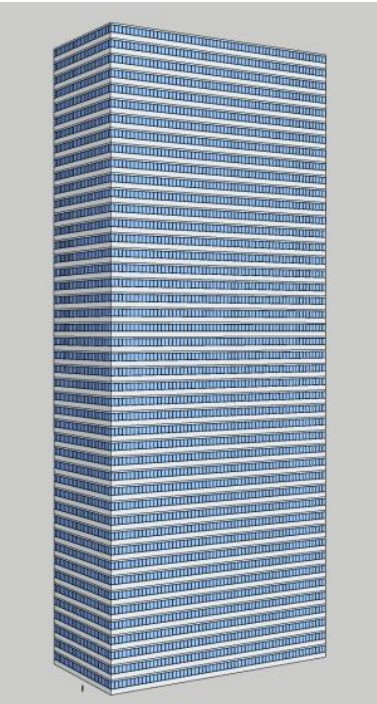

Figure 3.4: Schematic of the building showing the layout of the cladding system.

Table 3.1: Fragility functions for the three damage states of each glazing unit.

Component	Damage state (DS)	EDP	DS nomenclature	Median	Dispersion	Mean	Std	Unit
Glazing panel	Glass hairline cracking	Dr	DS_{Dr_1}	0.021	0.45	-	-	rad
Glazing panel	Glass cracking	Dr	DS_{Dr_2}	0.024	0.45	-	-	rad
Glazing panel	Glass blowout	P^*_{60}	$DS_{p_{60}}$	-	-	5.29	0.91	kPa

* P_{60} is the 60 s equivalent pressure with exponential parameter $s = 16$.

the FEMA P-58 guidelines (*Federal Emergency Management Agency (FEMA)*, 2012b), was considered whose median values were defined by (see Fig. 3.2): $Q_{\min} = 20$, $Q_{\max} = 20$, $Q_{\max} = 2955$ [USD], and $Q_{\min} = 1576$ [USD]. Uncertainty in the consequence function was modeled through a log-normal distribution with dispersion of 0.1185.

3.8.2 Wind and rain hazard

3.8.2.1 Hazard curve

To characterize the extreme wind speed climate in Miami, the hurricane wind speed database of the National Institute of Standards and Technology (NIST) (*National Institute of Standards and Technology*, 1980) was considered. In particular, the dataset of milepost

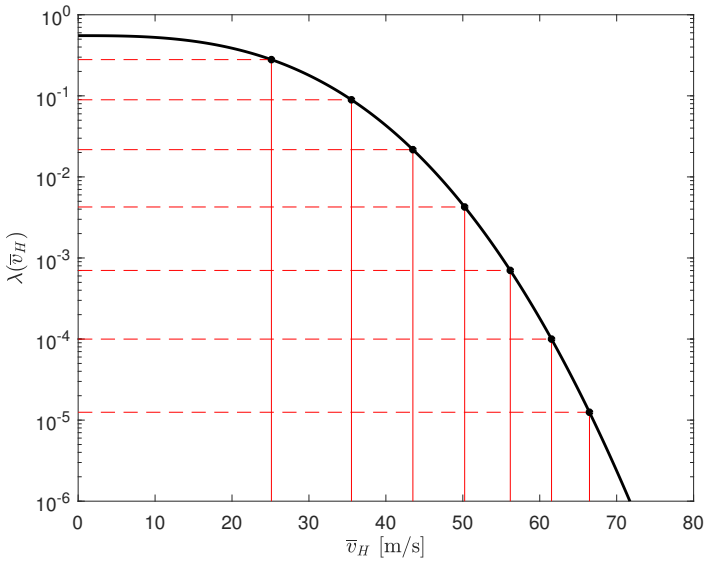

Figure 3.5: Illustration of the partitioned site-specific hazard curve.

1450 was used for which $\lambda_e = 0.55$. The distribution of $\bar{V}_H$ was estimated from the dataset as outlined in Sec. 3.3.1 while assuming a Weibull distribution for $F_{\bar{V}_H}$. To implement the stochastic simulation scheme of Sec. 3.7.2, $N_{\bar{v}_H} = 8$ was considered with the lower bound wind speed of the eighth and final interval chosen so as to have an annual exceedance rate of $\lambda(\bar{v}_H) = 1.25 \times 10^{-5}$, i.e. risk category III as indicated in Table 1.3-1 of (*ASCE 7-16*, 2016). By partitioning in terms of the square wind speed, the hazard curve was decomposed into the intervals illustrated in Fig. 5.3.

3.8.2.2 Wind direction

Each wind speed of the NIST hurricane database is paired with a wind direction. This data can therefore be used to estimate the conditional CCDF of Eq. (3.5) through the procedure of Sec. 3.3.2.1. Within this context, Fig. 3.6(a) reports the kernel density estimated circular pdf of α (where $\alpha = 0$ indicates wind blowing down the y direction) while Fig. 3.6(b) reports the bivariate copula associated with wind speed and direction of Eq. (3.7). In particular, from Fig. 3.6(b), the complex nonlinear dependency between $\bar{v}_H$ and α captured by the kernel copula is clearly evident.

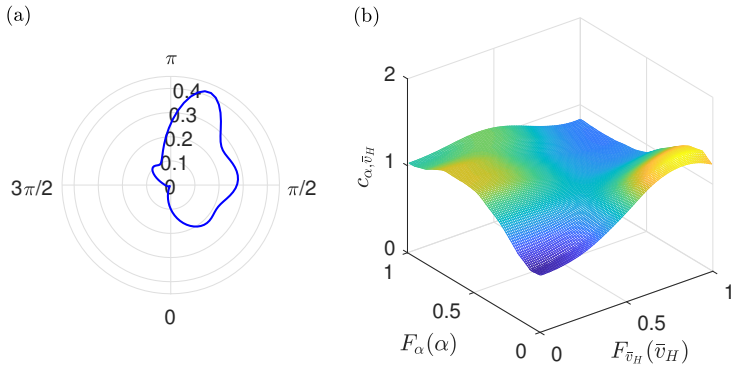

Figure 3.6: (a) Circular pdf of wind direction; (b) bi-variate copula density between $\bar{v}_H$ and α of Eq. (3.7).

3.8.2.3 Concurrent rainfall intensity

Due to a lack of available concurrent rainfall intensity and paired wind speed and direction data, the concurrent rainfall intensity was taken as independent of the intensity and direction of the wind event, i.e. the following was assumed $G(R_T|\alpha, \bar{v}_H) = G(R_T)$ which is also consistent with recent observations (*Rappaport*, 1999; *Dong et al.*, 2017). To estimate $G(R_T)$, the maximum annual 1-hour rainfall intensities occurring in Miami and associated with hurricanes were extracted from the Weather Bureau's technical report (*Bureau*, 1957-1960). After appropriate processing of the data, a Weibull distribution was fitted leading to the concurrent rainfall intensity CCDF of Fig. 3.7.

3.8.3 Envelope actions

3.8.3.1 External pressure coefficients

To calibrate the stochastic model of Sec. 3.4.1, datasets of the Tokyo Polytechnic University directional wind tunnel database (*Tokyo Polytechnic University*, 2008) were used. Each dataset consisted in simultaneous measurements of 510 pressure taps, located over the building surface, for which transient pressure coefficients were estimated at 10° increments starting from $\alpha = 0$. This data was used to estimate the POD eigenvalues and eigenvectors,

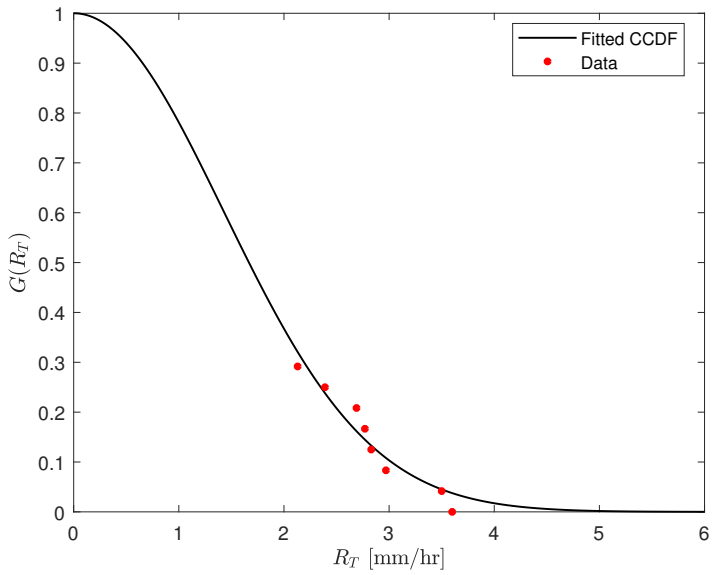

Figure 3.7: CCDF of the concurrent maximum hourly rainfall intensity for Miami.

Λ_i and $\mathbf{\Psi}_i$, necessary for calibrating the stochastic model of Eq. (3.11). In particular, the first 10 modes were considered sufficient for representing the external pressure field. In calibrating the kernal-Pareto mixture model describing the marginal distributions of $\mathbf{C}_{p,e}(t)$, 5% upper and lower tail thresholds were considered.

To illustrate the capability of the stochastic model in capturing the generally non-Gaussian features of $\mathbf{C}_{p,e}(t)$, Fig. 3.8 reports the comparison between the empirical marginal pdfs of three components of $\mathbf{C}_{p,e}(t)$ corresponding to two pressure taps (indicated with $C_{p,e,1}$ and $C_{p,e,1}$) located on the right x-direction face and one pressure tap (indicated with $C_{p,e,3}$) located on the back y-direction face for a wind direction of $\alpha = 0°$ and wind speed of $\bar{v}_H = 43.9$ m/s. As can be seen, good correspondence between the empirical and calibrated marginal pdfs is achieved. Figure 3.8 also reports the comparison between the target wind tunnel derived power spectral densities (PSDs) and those of the stochastic model. Good correspondence is achieved over a full range of frequencies indicating the sufficiency of using 10 POD modes. Figure 3.9 provides the comparison between the wind tunnel time histories of $C_{p,e,1}$, $C_{p,e,2}$, and $C_{p,e,3}$ and a randomly generated realization from the stochastic model. From visual inspection, the model can be seen to provide a good representation of the time histories.

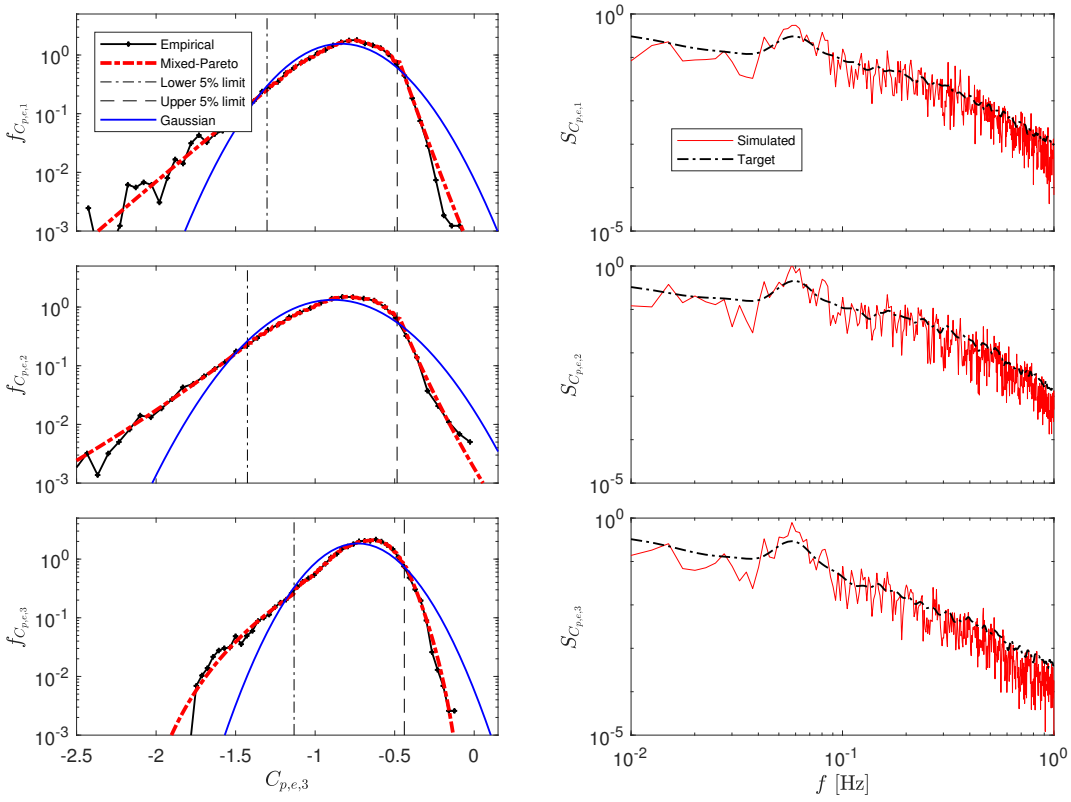

Figure 3.8: Comparison between target and calibrated stochastic model in terms of marginal pdfs and PSDs of $C_{p,e,1}$, $C_{p,e,2}$, and $C_{p,e,3}$.

Similar results to those of Figs. 3.8 and 3.9 were seen for all components of $\mathbf{C}_{p,e}(t)$.

3.8.3.2 Wind driven rain

The wind driven rain was simulated in OpenFOAM (*Weller et al.*, 1998). In particular, the three computational domains reported in Fig. 3.10 were considered. Each domain had a total of 139500 rectangular elements. These domains where used to simulate the normalized specific catch ratios for the wind directions of 0°, 45° and 90° for 17 rain phases defined by the raindrop diameters between 0.3 mm and 2.4 mm with 0.3 mm increments and between 2.4 mm and 6 mm with 0.4 mm increments. Through symmetry, these results were extended to the wind directions of 135°, 180°, 225°, 270° and 315°. With respect to wind speed, solutions where estimated at the boundaries of the hazard curve decomposition reported in Fig. 5.3. As discussed in Sec. 5.4.2, for intermediate values of wind speed and direction,

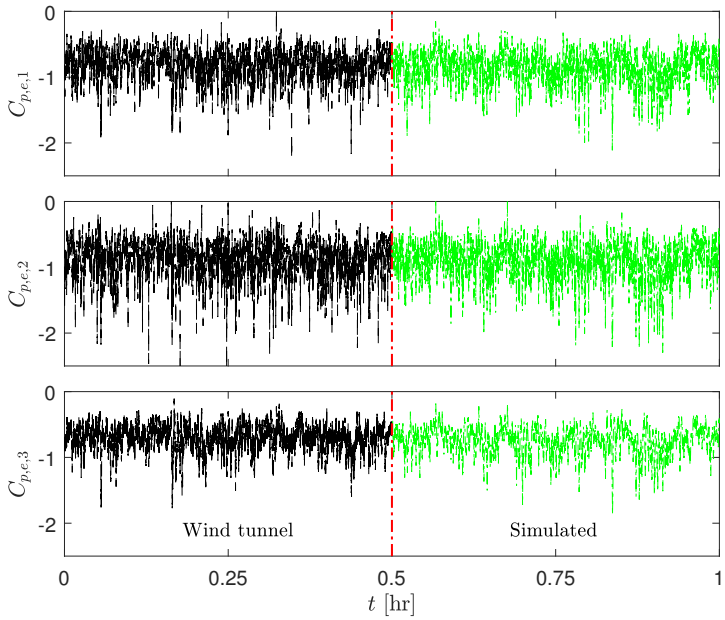

Figure 3.9: Comparison between the wind tunnel realization of $C_{p,e,1}$, $C_{p,e,2}$, and $C_{p,e,3}$ and a corresponding realization of the calibrated stochastic model.

linear interpolation/extrapolation was considered.

3.8.4 Results

In implementing the stochastic simulation scheme of Sec. 4.6, 1000 samples were considered for each interval of the partitioned hazard curve of Fig. 5.3. A total storm duration of $T = 1$ h was considered. In implementing the damage model of Sec. 3.5, a time step of $\Delta t = 0.5$ s was used.

3.8.4.1 System measures

With respect to the systems measures, i.e. the vectors $\mathbf{DS}$ and $\mathbf{V}_w$ reporting the final damage states and water ingress at each cladding component, detailed probabilistic component-level damage and water ingress maps can be constructed. For example, Fig. 3.11 reports the mean annual rate of each component of the envelope system assuming one of the three possible damage states outlined in Table 3.1 at the end of the wind event. It is interesting to observe the role played by the probability distribution of wind direction, reported in Fig.

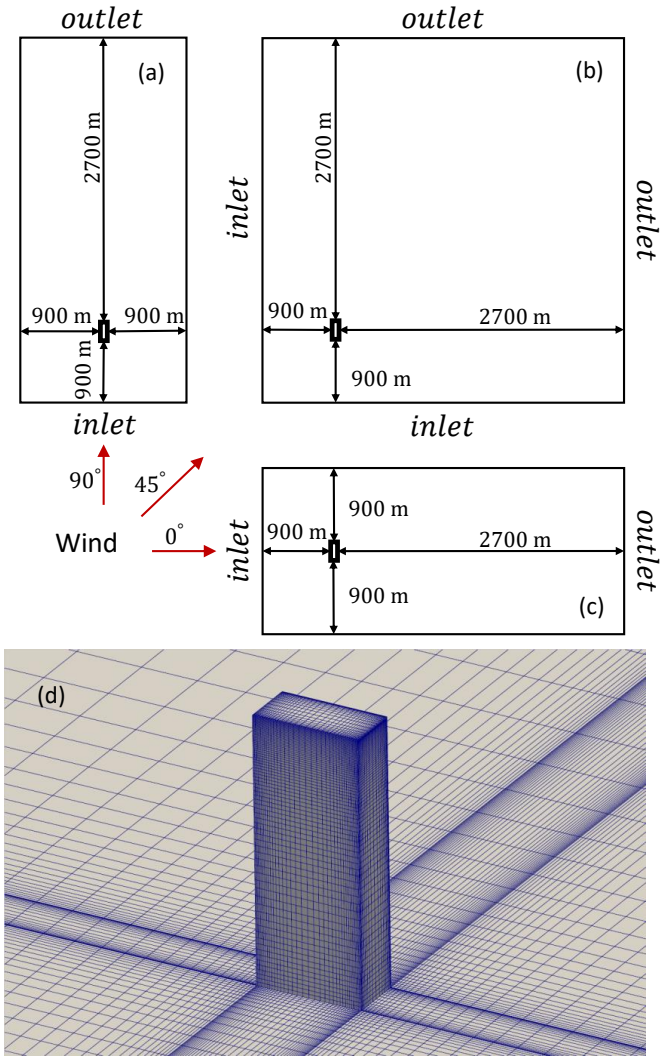

Figure 3.10: Schematic of the computational domains used to estimate the wind driven rain: (a) set up for $\alpha = 90°$; (b) set up for $\alpha = 45°$; (c) set up for $\alpha = 0°$; (d) typical mesh around the building.

3.6(a) in terms of the marginal pdf, on the mean annual rate of pressure damage. Indeed, the preference for wind directions in the interval $[0, 2\pi]$ leads to increased probability of higher positive pressures on the right/left of the front/back faces of the building as compared to the left/right of the front/back faces. It also generates increased probability of negative pressures on the edges of the left face as compared to the right face. This ultimately results in the asymmetric map of the mean annual rate of pressure damage of Fig. 3.11. From this figure, it can also be seen that, for a structural system designed to achieve drift ratio limits of 1/400 under wind loads calibrated to 50-year MRI wind speeds, damage will be dominated by local pressure, i.e. the mean annual rate of assuming as a final damage state $DS_{P_{60}}$ dominates. Notwithstanding this, Fig. 3.11 clearly illustrates that there is a non-negligible probability of having drift induced damage to the envelope system of high-rise systems subject to severe wind events. In terms of critical components, from the damage map of Fig. 3.11 it can be seen that annual rates in excess of 5×10^{-5} (color map limit) can be reached for window blowout on the right and left faces of building. Similar maps and analysis can be constructed and carried out for $\mathbf{V}_w$.

The knowledge of **DS** also enables system-level damage analysis. For example, Fig. 3.12 reports the mean annual rate of having more than N_{DS} cladding components assume as a final damage state one of the three damage states of Table 3.1. In particular, it can be seen that there is around a 2×10^{-3} rate of having at least one window blown out during a hurricane event. This corresponds to a MRI of 500 years.

3.8.4.2 Losses and consequences

Through the consequence functions of Sec. 3.8.1.2, probabilistic system-level loss curves can be estimated in terms of decision variables, *dv*s, identified with repair costs or time. In this respect, Fig. 3.13 reports the mean annual rate of exceeding a system-level repair cost C. From this curve, information such as the repair costs associated with MRIs of interest can be directly estimated. For example, by entering vertical axis of the loss of Fig. 3.13 at a

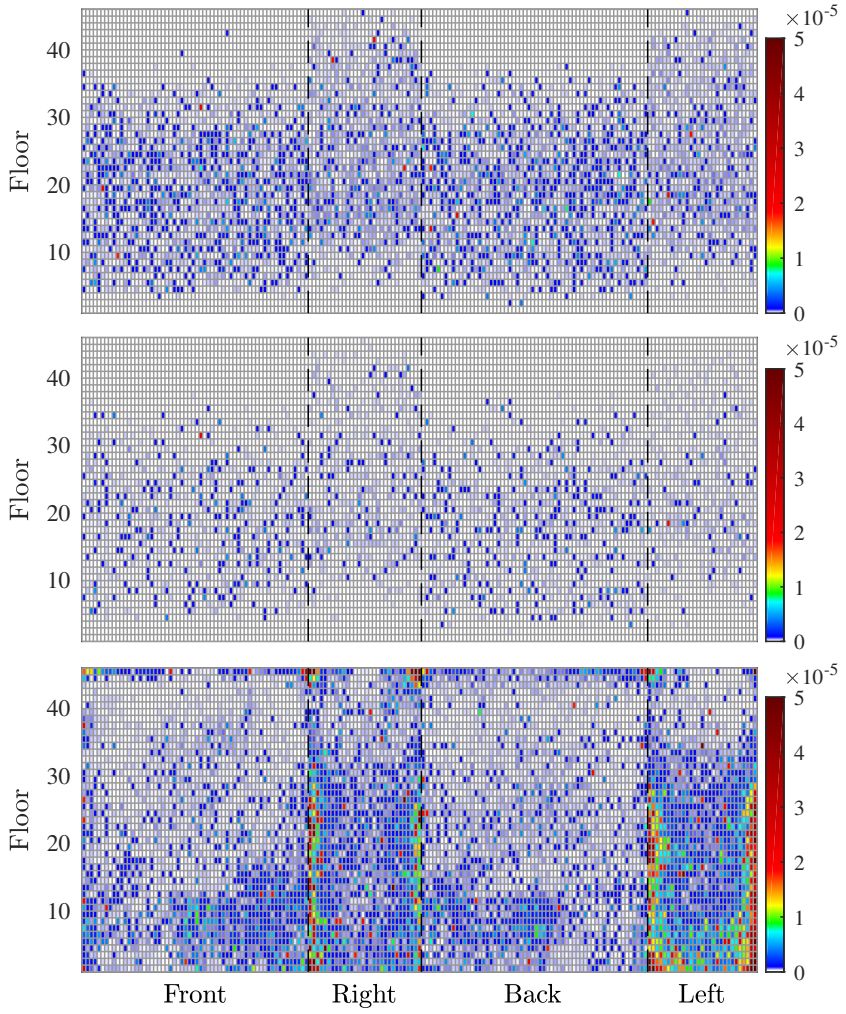

Figure 3.11: Mean annual rate of a cladding element assuming a final damage state DS_{Dr_1} top, DS_{Dr_2} middle, or $DS_{P_{60}}$ bottom.

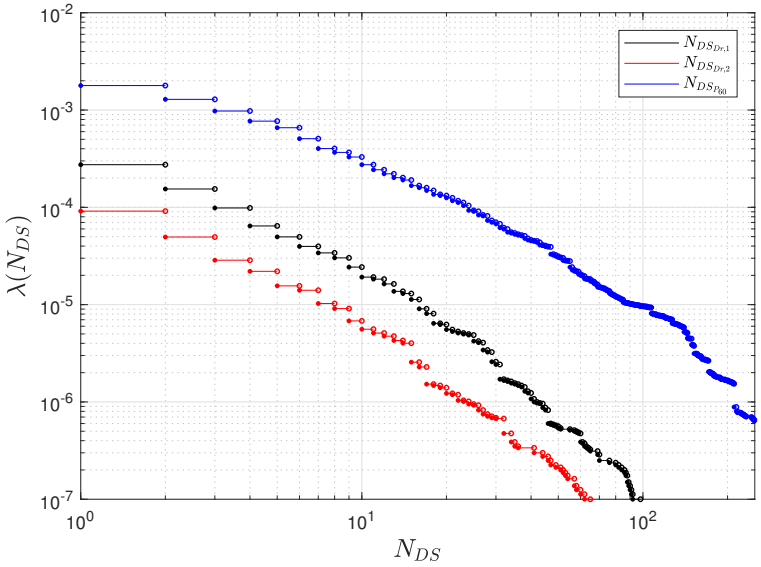

Figure 3.12: System-level mean annual rate of having N_{DS} components in DS_{Dr_1}, DS_{Dr_2}, or $DS_{P_{60}}$ at the end of the wind event.

value of $1/\text{MRI} = 1/1700 = 5.88 \times 10^{-4}$, the system-level repair cost with MRI of 1700 years can be estimated from the horizontal axis of the loss curve to be around \$9000. It should be observed that the value of \$9000 for a 1700-year event depends on the assumptions made in calibrating the the model, i.e. isolated building, fragility functions of Table Table 3.1, and negligible debris damage. Variations in these conditions could well result in situations in which the same building is predicted to have significant damage, and therefore losses, at lower return periods. Future development of this framework will include sensitivity analysis to identify the most influential parameters to losses. Similarly, the realizations of the system measures of component-level water ingress, $\mathbf{V}_w$, can be used to directly estimate system-level consequences in terms of mean annual exceedance rates of total ingressed water due to damaged envelope components. From this consequence curve, reported in Fig. 3.14, it can be estimated, for example, that the 1700-year total water ingress is around 3 m^3. Both the consequence curve of Fig. 3.14 and the loss curve of Fig. 3.13 can be deaggregated in order to provide more detailed information on the losses and consequences. For example, Fig. 3.15 reports deaggregation of the consequence curve of Fig. 3.14, where water ingress is reported for 15 groups of five consecutive floors commencing from the ground floor. From

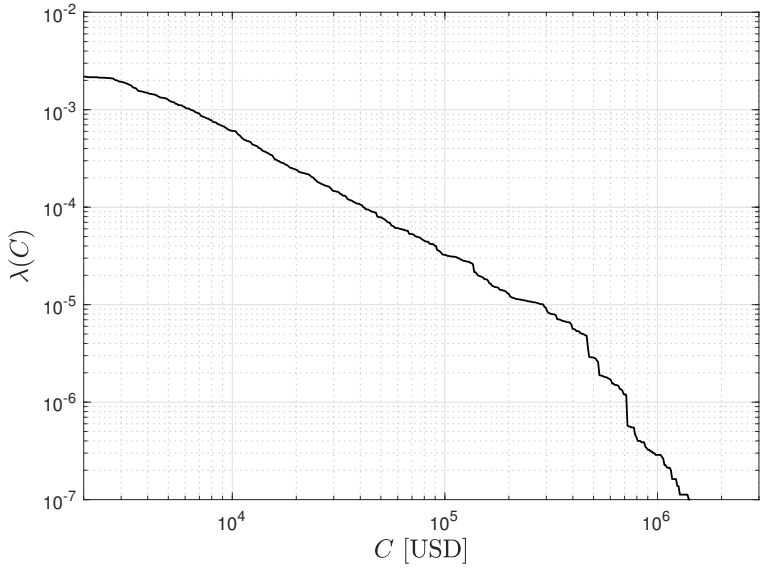

Figure 3.13: System-level mean annual rate of exceeding a repair cost associated with damage to the envelope system.

this deaggregation, it can be seen that the damage to the envelope components at the bottom to mid height will cause the majority of water ingress due to the effects of water runoff.

Finally, from Fig. 3.12 to Fig. 3.14, the effectiveness of the conditional stochastic simulation scheme of Sec. 3.7.2 is evident. Indeed, notwithstanding that only 8000 samples were generated in estimating the exceedance rates of Figs. 3.12 to 3.14, smooth estimates of failure rates as low as 10^{-5} are achieved. It should be observed that, by adding additional intervals, even lower rates could be accurately estimated.

3.8.5 Discussion

The case study of this section illustrated the potential of the proposed framework for probabilistically characterizing the performance of envelope systems of engineered structures. Having said this, there are some necessary advancements that would fully enable the transition from proof-of-concept to implementation. These include the modeling of damage due to debris as well as the modeling of water ingress through non-damaged envelope components. In particular, the first is a complex problem, as it is highly sensitive to the surrounding debris sources (including those caused by the progressive damage of nearby buildings) and would

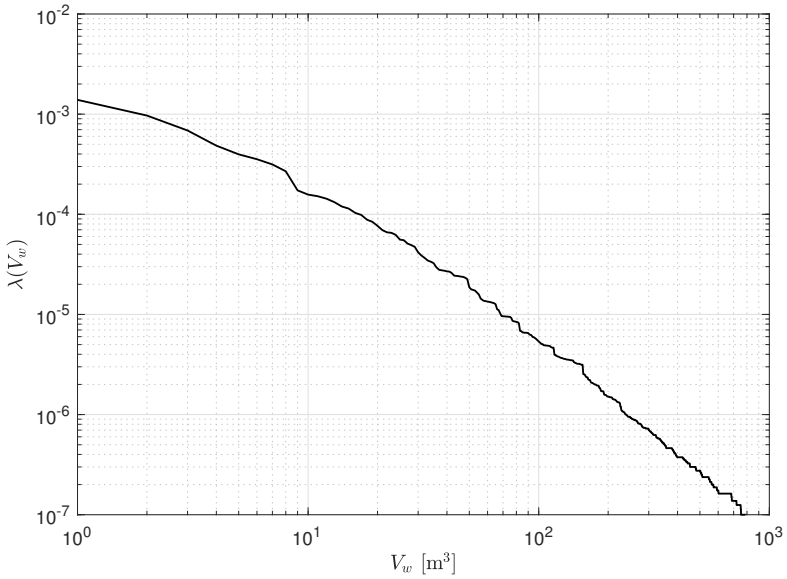

Figure 3.14: System-level mean annual rate of exceeding a total volume of ingressed water due to envelope damage.

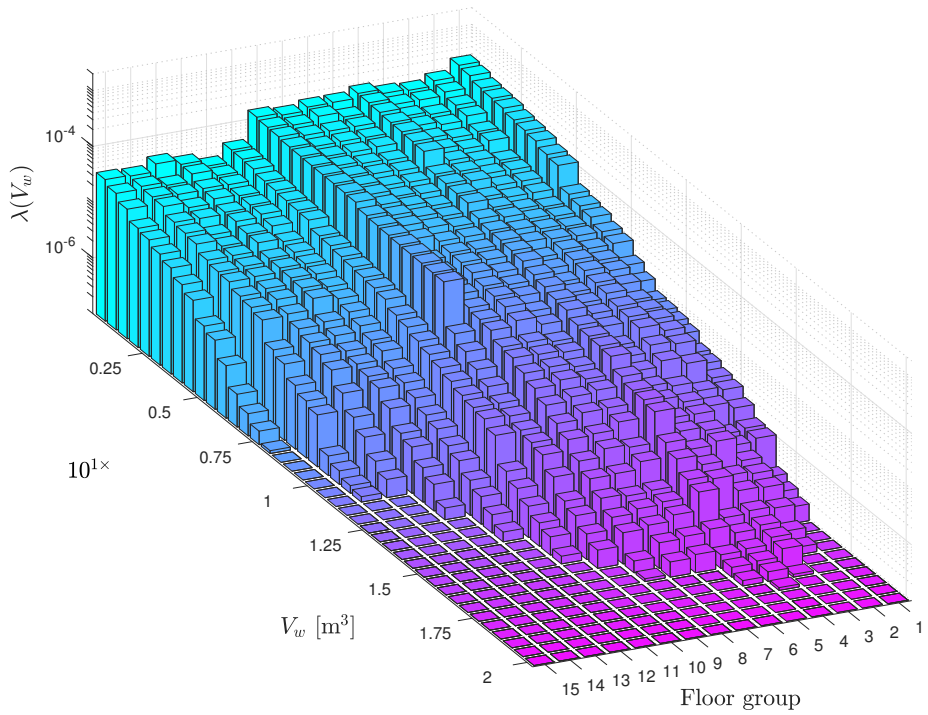

Figure 3.15: Deaggregation of the consequence curve of Fig. 3.14. Each group consists in five consecutive floors starting from the ground level.

require their careful probabilistic characterization. Having said this, because of how the proposed framework is based on stochastic simulation, once models are identified, they could be directly integrated into the framework. With respect to water ingress through non-damaged envelope components, recent models proposed during the development of the FPHLM (e.g. *Johnson et al.*, 2018) could be readily added. It should also be observed that, while this case study used off-the-shelf wind tunnel data, this was for illustration purposes. Indeed, consistently with the intent of PBWE, site-specific wind tunnel data would in general have to be used in order to properly capture the aerodynamic effects of surrounding buildings. In closing, it should also be observed that a final step for making the transition from proof-of-concept to implementation would be validation. This would require the calibration of the proposed framework to a building that sustained significant and documented damage during a hurricane event of measured intensity and track. An example of such a building could be the Chase Tower in downtown Houston, which sustained significant envelope damage during hurricane Ike (*Vega and Koke*, 2008).

3.9 Summary and conclusions

A computational framework for the holistic performance assessment of the envelope system of engineered building systems was proposed in this paper. The framework is based on integrating within a stochastic simulation framework: 1) data-driven probabilistic models of the extreme directional wind and concurrent rainfall hazard; 2) wind tunnel informed non-Gaussian stochastic pressure field models; 3) CFD-based Eulerian multiphase wind driven rain models; 4) fragility-based progressive damage models; and 5) loss and consequence models. By integrating these models within a conditional stochastic simulation framework, an efficient approach is defined for estimating system-level loss and consequences related to decision variables such as repair costs and ingressed water due to envelope damage. Because the framework is based on direct simulation, the results can be deaggregated as desired leading to detailed information on, for example, the mean annual rate of any particular envelope

component of the system assuming a given damage state, e.g. glass panel blowout or glass cracking. Similarly, detailed information can be obtained for the annual rate of water ingress through damaged envelope components. To illustrate the framework, the performance of a 45-story building clad with a typical dual-pane envelope system is analyzed for the directional Miami hurricane climate. System-level loss and consequence curves are derived as are the local and system-level damage state annual exceedance rates. Estimates of the 1700-year dollar losses and consequent water ingress are derived to illustrate the practicality of the framework within a decision-making process. It is believed that the framework outlined in this work will be of particular interest to the designers and analysts of buildings with engineered envelope systems designed within the context of performance-based wind engineering to resist extreme wind climates.

3.10 Acknowledgment

The research effort was supported in part by the National Science Foundation (NSF) under Grant No. CMMI-1562388. This support is gratefully acknowledged.

CHAPTER IV

Performance-Based Wind-Induced Structural and Envelope Damage Assessment of Engineered Buildings Through Nonlinear Dynamic Analysis[1]

Abstract

Performance-based wind engineering (PBWE) is undergoing a period of rapid development with numerous procedures and frameworks being proposed over the past few years. Notwithstanding these advancements, there is still a knowledge gap concerning the relative severity, dependency and rate of occurrence of structural and envelope damage in extreme wind events. This work is focused on investigating this problem for engineered buildings. In particular, envelope damage is estimated through a recently introduced PBWE framework that explicitly includes the effects of demands originating from dynamic net pressure and the structural responses. Structural damage is estimated through both fragility analysis as well as material yielding/hysteresis modeled through the adoption of a nonlinear fiber-based finite element formulation. Structural responses include the effects of large deformations through solving the finite element model in a corotational environment. To investigate the relative severity and dependency between the damages, a carefully calibrated archetype 45-story steel

[1]Ouyang, Z., & Spence, S. M. (2021). Performance-based wind-induced structural and envelope damage assessment of engineered buildings through nonlinear dynamic analysis. *Journal of Wind Engineering and Industrial Aerodynamics, 208*, 104452.

building located in Miami, FL, and subject to hurricane winds is studied. Probabilistic damage metrics are estimated for both the envelope and structural systems and are subsequently discussed in terms of relative severity, occurrence rates and nonlinear structural behavior.

4.1 Introduction

The assessment of wind excited engineered buildings is undergoing a period of rapid change driven by the interest in applying the principles of Performance-based wind engineering (PBWE) during the assessment and design of both the structural and envelope systems. This interest stems from the desire to both mitigate the huge economical losses incurred each year due to windstorms (*NOAA National Centers for Environmental Information (NCEI)*, 2020) as well as provide designers the flexibility to introduce innovative solutions that can reduce overall costs and environmental impact without loss of performance (*Ghosn et al.*, 2016). This has resulted in the development of a number of frameworks for the probabilistic PBWE assessment of engineered buildings in which structural and non-structural damages, including those to the envelope system, are estimated in terms of the dynamic response of the structural system (*Ciampoli et al.*, 2011; *Smith and Caracoglia*, 2011; *Petrini, F. and Ciampoli, M.*, 2012; *Chuang and Spence*, 2017; *Cui and Caracoglia*, 2018; *Zheng et al.*, 2019; *Cui and Caracoglia*, 2020; *Petrini et al.*, 2020). The root of many of these frameworks can be traced back to the performance-based seismic engineering (PBSE) methodologies introduced by the Pacific Earthquake Engineering Research (PEER) Center (*Cornell and Krawinkler*, 2000; *Porter*, 2003; *Yang et al.*, 2009) (and subsequently refined in the P-58 methodology (*Federal Emergency Management Agency (FEMA)*, 2012a)). The possibility of extending these frameworks to extreme wind is a consequence of how both hazards solicit a dynamic response of the lateral loading resisting system that can lead to direct damge to the structural system as well as indirect damage to non-structural components, e.g. envelope system, due to excessive dynamic responses, e.g. interstory drifts. This similarity in the mechanisms causing damage, together with the way in which damages and losses are estimated in PBWE

and PBSE, opens the door to the possibility of developing multi-hazard wind and seismic performance-based engineering frameworks, e.g. (*Venanzi et al.*, 2018; *Zheng et al.*, 2020). By providing a global approach, such multi-hazard frameworks represent a clear advantage in areas where both hazards are significant.

Notwithstanding these advances, a common assumption of the aforementioned PBWE frameworks is the neglect of damages to the envelope system due to excessive local net dynamic wind pressure, in spite of how this action can lead to significant damages (*Behr and Minor*, 1994; *Williams and Kareem*, 2003; *Kareem and Bashor*, 2006). With the aim of beginning to fill this gap, the authors have recently introduced a PBWE framework that is specifically focused on estimating losses caused by damages to the envelope system of engineered buildings in which both local net dynamic wind pressure and dynamic structural responses are treated as demands (*Ouyang and Spence*, 2019, 2020). The results of this work illustrated how damages from excessive local net dynamic wind pressure are in general greater than those generated by interstory drifts extracted from the dynamic structural response of the system. However, an important assumption of these models lies in how the structural system is treated as linear elastic, i.e. potential yielding of the structural system is ignored as are the effects of large deformations and potential connection damage. This assumption neglects not only potential losses due to structural damage but also the additional damage to the envelope system due to potential increases in the dynamic structural responses and so interstory drifts. It is also in discordance with the recent interest in letting the structural system of engineered buildings experience yielding in extreme events (*Judd and Charney*, 2015; *Tabbuso et al.*, 2016; *Chuang and Spence*, 2017; *Feng and Chen*, 2017, 2018; *Judd*, 2018; *Mohammadi et al.*, 2019; *American Society of Civil Engineers*, 2019).

This work is focused on investigating the importance of this assumption through the further development of the probabilistic PBWE framework recently introduced in (*Ouyang and Spence*, 2020). In particular, the linear elastic modal analysis modeling environment for the structural system is replaced with a nonlinear fiber-based dynamic finite element mod-

eling environment. Material yielding/hysteresis is enabled together with large deformations through the adoption of a corotational formulation. To consider the possibility of connection/joint damage, a fragility-based approach is adopted. To investigate the occurrence of structural damage and the dependency of envelope damage on this, together with large deformations, a carefully calibrated archetype 45-story steel high-rise building is considered. The building is assumed located in Miami, FL, and is designed to achieve common serviceability requirements as well as life safety limit states under dynamic wind loads and ASCE 7 load combinations for a risk category II building (*American Society of Civil Engineers*, 2016). A series of probabilistic component-/system-level damage metrics are evaluated for both the structural and envelope systems. The relative severity, dependency and rate of occurrence of structural and envelope damage during extreme wind events is subsequently analyzed and discussed within the context of PBWE.

4.2 The performance-based wind engineering framework

A widely adopted framework for implementing PBSE is that proposed by the PEER Center (*Cornell and Krawinkler*, 2000; *Porter*, 2003; *Yang et al.*, 2009). This framework is at the core of the PBWE framework considered in this work where applicability to wind is achieved through the modifications recently introduced by the authors in (*Ouyang and Spence*, 2020). The approach is based on describing performance through estimating the mean annual rate, λ, of exceeding a threshold value of a decision variable related to the general performance of the envelope system, e.g. mean annual rate of exceeding a threshold value of envelope repair costs. In particular, damage is estimated in terms of system measures, sm_i, that are related to the occurrence of a predefined damage state, e.g. blowout of an envelope component due to excessive dynamic net wind pressure, or the exceedance of a threshold value of a predefined damage measure, e.g. number of envelope components in a given damage state at the end of the wind event. From a theoretical standpoint, the annual rate at which the system measure, sm_i, occurs (is exceeded) can be written through the

application of the total probability theorem as:

$$\lambda(sm_i) = \iint G(sm_i|\alpha, \bar{v}_H)|\mathrm{d}G(\alpha|\bar{v}_H)||\mathrm{d}\lambda(\bar{v}_H)| \tag{4.1}$$

where: $\bar{v}_H$ is the maximum hourly mean wind speed at the building top; α is the wind direction; $G(sm_i|\alpha, \bar{v}_H)$ is the probability of occurrence/exceedance of sm_i given α and $\bar{v}_H$; $G(\alpha|\bar{v}_H)$ is the conditional complementary cumulative distribution function (CCDF) of wind direction given wind speed; while $\lambda(\bar{v}_H)$ is the non-directional annual wind hazard curve in terms of $\bar{v}_H$.

In (*Ouyang and Spence*, 2020), Eq. (4.1) was used to estimate damage exclusively to the envelope system. In this work, Eq. (4.1), and therefore the framework outlined in (*Ouyang and Spence*, 2020), will be extended to include damage to the structural system. This will be achieved through considering additional system measures that will be estimated through both fragility analysis as well as output from nonlinear finite element models of the structural system. This will enable not only the understanding of the extent of the dependency between envelope and structural damage, but also a comprehensive estimation of damage to the two most critical systems of an engineered building designed to survive in extreme winds.

It should be observed that Eq. (4.1) can be seen to decompose the task of damage estimation into two separate analysis steps. The first is related to the characterization of the structure and site specific wind hazard and involves the estimation of the non-directional wind hazard curve $\lambda(\bar{v}_H)$ and the directional term $G(\alpha|\bar{v}_H)$, while the second is related to the characterization of damage, through the term $G(sm_i|\alpha, \bar{v}_H)$, sustained by the envelope/structural system for a wind event of given intensity. Inherent to $G(sm_i|\alpha, \bar{v}_H)$ is the dynamic response of the system to time histories of aerodynamic loads conditioned on wind speed, $\bar{v}_H$, and wind direction, α.

4.3 Hazard analysis

To characterize the wind hazard at the site of interest, the terms $\lambda(\bar{v}_H)$ and $G(\alpha|\bar{v}_H)$ require estimation. Following the procedure outlined in (*Ouyang and Spence*, 2020), these can be estimated as:

$$\lambda(\bar{v}_H) = \lambda_e \left(1 - F_{\bar{v}_H}(\bar{v}_H)\right) \tag{4.2}$$

$$G(\alpha|\bar{v}_H) = \int_{\alpha}^{2\pi} f_{\alpha,\bar{v}_H}(\alpha, \bar{v}_H) \left(\frac{\mathrm{d}F_{\bar{v}_H}}{\mathrm{d}\bar{v}_H}\right)^{-1} \mathrm{d}\alpha \tag{4.3}$$

where λ_e is the annual arrival rate of the extreme wind events; $F_{\bar{v}_H}$ is the site specific non-directional cumulative distribution function (CDF) of $\bar{v}_H$ conditioned on the occurrence of an extreme wind event ($F_{\bar{v}_H}$ is typically taken as an extreme value distribution, e.g. a Weibull or Type I distribution); while $f_{\alpha,\bar{v}_H}(\alpha, \bar{v}_H)$ is the joint probability density function (JPDF) between $\bar{v}_H$ and the associated wind direction α.

To estimate the JPDF between $\bar{v}_H$ and α, a copula approach can be followed in which $f_{\alpha,\bar{v}_H}$ is estimated as:

$$f_{\alpha,\bar{v}_H}(\alpha, \bar{v}_H) = c_{\alpha,\bar{v}_H}\left(F_\alpha(\alpha), F_{\bar{v}_H}(\bar{v}_H)\right) \frac{\mathrm{d}F_\alpha}{\mathrm{d}\alpha} \frac{\mathrm{d}F_{\bar{v}_H}}{\mathrm{d}\bar{v}_H} \tag{4.4}$$

where $F_\alpha(\alpha)$ is the circular CDF of α (e.g. a generalized Von Mises or circular kernel estimated CDF) while $c_{\alpha,\bar{v}_H}$ is the bivariate copula function describing the dependency between $\bar{v}_H$ and α. In general, due to the nonlinear nature of the dependency between $\bar{v}_H$ and α, non-parametric copulas, such as the kernel density copula, should be used. To calibrate $c_{\alpha,\bar{v}_H}$, paired wind speed and wind direction data at the building site is required. However, in general, wind data is recorded at meteorological stations, and therefore require transformation to the site of interest before $c_{\alpha,\bar{v}_H}$ can be calibrated. This transformation should account for factors such as the generally different averaging times between the data collected at the meteorological station and that of interest to the analysis, differences in terrain conditions, as well as unavoidable observation and sampling errors. To account for this, probabilistic

transformations can be used. In this work, the transformations outlined in (*Ouyang and Spence*, 2020) are adopted. Therefore, the wind speed data is transformed through the probabilistic model outlined in (*Spence and Kareem*, 2014a), while wind direction is considered invariant and deterministic. Within this setting, $c_{\alpha,\bar{v}_H}$ and $F_{\bar{v}_H}$ become the expected site specific bivariate copula and non-directional CDF. For more details the reader is referred to (*Ouyang and Spence*, 2020).

4.4 Envelope system measures

The system measures, sm_i, related to envelope damage are estimated in this work through the framework outlined in (*Ouyang and Spence*, 2019). This framework estimates damage to each envelope component through evaluating suites of sequential fragility functions, used to model the susceptibility of the envelope components to suites of sequential damage states, through demands related to the dynamic net wind pressure and structural response. A brief overview of this framework within the context of this work will be provided in the following.

4.4.1 Dynamic net wind pressure demand

Demands on each envelope component due to wind pressure can be evaluated in terms of the dynamic net pressure:

$$p_n(t;\bar{v}_H,\alpha,\xi_{x,y,z}) = \frac{1}{2}\rho\bar{v}_H^2\left[C_{p,e}(t;\alpha,\xi_{xyz}) - C_{p,i}(t;\xi_{xyz})\right] \tag{4.5}$$

where $\xi_{x,y,z}$ is a generalized coordinate identifying the location of envelope component, $C_{p,e}$ is the external dynamic wind pressure coefficient acting on the component, $C_{p,i}$ is the internal dynamic pressure coefficient acting on the component, while ρ is the air density. To evaluate p_n, separate internal/external pressure models are required.

4.4.1.1 External pressure

The external pressure coefficients can be modeled as a non-Gaussian stochastic vector process $\mathbf{C}_{p,e}(t)$ where each coordinate of $\mathbf{C}_{p,e}(t)$ corresponds to a point on the building surface where experimental information is available on the dynamic behavior of the external pressure. In general, this information is gathered through wind tunnel tests carried out on scale models of the building. Therefore, the components of $\mathbf{C}_{p,e}(t)$ are generally related to where the pressure was measured in the wind tunnel. Numerical interpolation and extrapolation can then be implemented to obtain the external pressure value at the location of each envelope component. From the wind tunnel data, a proper orthogonal decomposition (POD) based spectral representation model can be calibrated for providing a Gaussian stochastic representation, $\tilde{\mathbf{C}}_{p,e}^{\mathcal{GP}}(t)$, of the external pressure coefficients (*Chen and Letchford*, 2005; *Chen and Kareem*, 2005). To capture the generally important non-Gaussian effects, a translation model can be used in which the nth component of $\tilde{\mathbf{C}}_{p,e}^{\mathcal{GP}}(t)$ is transformed as:

$$\tilde{C}_{p,e}^{(n)}(t;\alpha) = F_{C_{p,e}^{(n)}}^{-1}\left\{\Phi\left[\frac{\tilde{C}_{p,e}^{\mathcal{GP}(n)}(t;\alpha) - \mu_{C_{p,e}^{\mathcal{GP}(n)}}(\alpha)}{\sigma_{C_{p,e}^{\mathcal{GP}(n)}}(\alpha)}\right]\right\} \tag{4.6}$$

where Φ is the standard normal distribution function, $\mu_{C_{p,e}^{\mathcal{GP}(n)}}$ and $\sigma_{C_{p,e}^{\mathcal{GP}(n)}}$ are the mean and standard deviation of the Gaussian process, and $F_{C_{p,e}^{(n)}}$ is the target non-Gaussian distribution. In particular, $F_{C_{p,e}^{(n)}}$ can be estimated directly from the wind tunnel data through fitting a kernel-Pareto mixture model (*Zhao et al.*, 2019).

4.4.1.2 Internal pressure

Before sustaining damage the building envelope is considered intact and airtight. In this case the internal pressure coefficient can be assumed as a time independent (static) random variable that assumes the following normal distribution (*Ellingwood and Tekie*, 1999):

$$F_{C_{p,i}}(C_{p,i}) = \Phi\left\{\frac{1}{\sigma_{C_{p,i}}}\left[C_{p,i} - \left(0.15 - 0.3\frac{A^+}{A}\right)\right\}\right] \tag{4.7}$$

where A^+ is the exposure area with positive mean pressure, A is the total exposure area of the building envelope, and $\sigma_{C_{p,i}} = 0.05$ is the standard deviation.

Once the envelope sustains damage, dynamic air flows will be formed at the openings due to pressure differences. This can also lead to air flows between internal compartments (i.e. the internal volumes defining the building). This will in general cause the internal pressure coefficient, $C_{p,i}$, to become transient. To treat this phenomenon, the model introduced in (*Ouyang and Spence*, 2019), which is capable of treating general sets of interconnected compartments, can be adopted . The model is based on describing the transient air flow at each opening (external/internal or internal/internal) through the unsteady-isentropic form of the Bernoulli equation (*Vickery and Bloxham*, 1992; *Guha et al.*, 2011; *Yu et al.*, 2008). From the principle of conservation of mass, a nonlinear system of dynamic equations can be written and solved through a 4th-order Runge-Kutta scheme for the vector of unknown transient internal pressure coefficients $\mathbf{C}_{p,i}(t)$. In implementing this scheme, the pressure induced damage states of each vulnerable envelope component is updated iteratively at each time step until dynamic pressure equilibrium is reached. Also, at the beginning of each time step, the damage state of each envelope component, induced by the dynamic drift, $Dr(t)$, must be provided, as this can result not only in degradation of the capacity of the envelope components to resist net pressure, but also new envelope openings. This leads to coupling between both the pressure, $p_n(t)$, and drift, $Dr(t)$, demands, as well as the capacities of the envelope components.

4.4.2 Dynamic drift demand

The drift demands, $Dr(t)$, require the estimation of the dynamic response of the structural system over the duration of the wind event. Notwithstanding the extreme nature of the wind speeds (3000 year mean recurrence intervals and above), in the framework outlined in (*Ouyang and Spence*, 2019, 2020), this problem was solved through assuming small deformations and linear elastic material behavior. Modal integration was then used to provide solutions. As

outlined in Sec. 4.5, this work will replace this assumption with a nonlinear modeling environment that considers both large deformations as well as material yielding/hysteresis.

4.4.3 Envelope damages

The susceptibility to damage of each envelope component to N_{P_n} pressure induced damage states and N_{Dr} drift induced damage states is modeled through two sets of sequential damage thresholds: $\mathbf{C}_P = \{C_{P_1} \leq C_{P_2} \leq ... \leq C_{P_{N_{P_n}}}\}$ and $\mathbf{C}_{Dr} = \{C_{Dr_1} \leq C_{Dr_2} \leq ... \leq C_{Dr_{N_{Dr}}}\}$. At a given time, $\hat{t}$, the largest damage threshold exceeded by the net pressure demand, $p_n(t)$, and drift demand, $Dr(t)$, in $[0, \hat{t}]$ dictates the current pressure and drift damage states. To model uncertainty in the thresholds, each set of damage states is associated with a set of standard sequential fragility functions. The coupling between the damage states (i.e. the reduction in the capability of an envelope component to resist pressure given the occurrence of a drift damage state or vice versa) is modeled through degenerating the damage thresholds upon the occurrence of the coupled damage state (e.g. if a drift damage state occurs that reduces the capacity of the envelope component to resist pressure, the thresholds $\mathbf{C}_P$ are reduced). Figure 4.1 illustrates the steps of the envelope damage model discussed in this section, where the final damage states of each envelope component represent the system measures of interest and are collected in the alphanumeric vector $\mathbf{DS}^E$.

4.5 Structural system measures

The system measures, sm_i, related to structural damage are estimated in this work through the adoption of a nonlinear fiber-based structural model that is integrated with a fragility-based structural damage model. As illustrated in Fig. 4.1, the response (in the form of interstory drift) of the structural model will also drive part of the envelope damage, therefore coupling structural and envelope system measures.

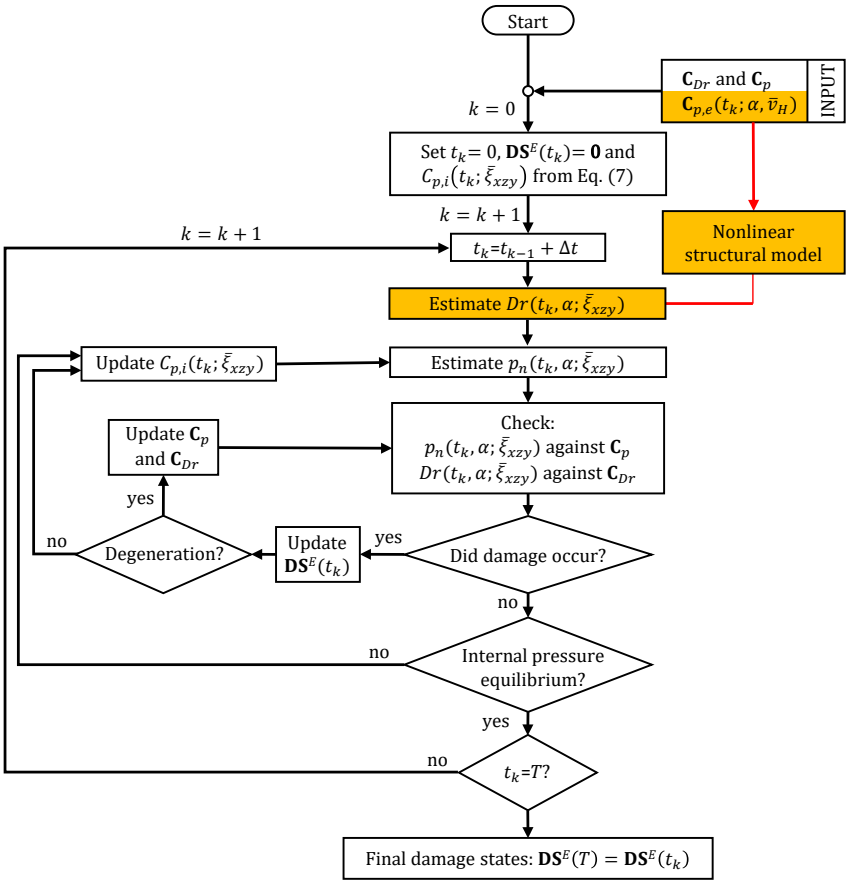

Figure 4.1: Damage model for the envelope system where the input from the nonlinear structural model has been highlighted.

4.5.1 Structural model

Under the actions of extreme winds, the structural system will in general experience a nonlinear dynamic response that can be modeled through dynamic equilibrium as:

$$\mathbf{M}\ddot{\mathbf{x}}(t)+\mathbf{C}\dot{\mathbf{x}}(t)+\mathbf{F}_{NL}\big(\mathbf{x}(t)\big)=\mathbf{f}(t;\bar{v}_H,\alpha) \tag{4.8}$$

where $\mathbf{x}(t)$, $\dot{\mathbf{x}}(t)$, and $\ddot{\mathbf{x}}(t)$ are the displacement, velocity and acceleration response vectors; $\mathbf{M}$ is the mass matrix of the system; $\mathbf{C}$ is the damping matrix of the system (generally modeled through Rayleigh damping); $\mathbf{f}(t;\bar{v}_H,\alpha)$ are the external wind loads for a wind speed of $\bar{v}_H$ and wind angle of α that can be directly estimated from the external pressure coefficients of Sec. 4.4.1.1; while $\mathbf{F}_{NL}(\mathbf{x})$ is the vector of restoring forces that are generally nonlinear due

to both material yielding/hysteresis and large deformations.

To solve the nonlinear system of Eq. (4.8), direct integration schemes can be used. In general, these schemes are based on modeling the change in $\mathbf{F}_{NL}(\mathbf{x})$ for a change in the state of the nonlinear system through evaluating the tangent stiffness matrix, $\mathbf{K}_{\top}\big(\mathbf{x}(t)\big)$, once an appropriate model has been introduced for $\mathbf{F}_{NL}(\mathbf{x})$. In this work, it is assumed that $\mathbf{F}_{NL}(\mathbf{x})$ can be estimated by discretizing the structural system through a fiber-based approach. In particular, because of its superior behavior over classic stiffness-based formulations (*Neuenhofer and Filippou*, 1997), a flexibility-based formulation with geometric nonlinearity is adopted (*Neuenhofer and Filippou*, 1998). In this approach, the equilibrium between the sectional and element end forces in a basic reference system (i.e. the local reference system associated with the element) is expressed in a strong form (pointwise as opposed to an average sense) as:

$$\hat{\mathbf{S}}_i(\hat{x}_i) = \mathbf{b}\,(\hat{x}_i)\,\hat{\mathbf{P}}_i \tag{4.9}$$

where $\hat{x}_i$ is the local coordinate indicating the position along the element, $\hat{\mathbf{S}}_i(\hat{x}_i)$ is the sectional force at $\hat{x}_i$, $\mathbf{b}$ is the matrix of displacement-dependent force interpolation functions, while $\hat{\mathbf{P}}_i$ is the vector of element end forces. In particular, considering a discretization of each section of the member into N_f fibers, the sectional forces can be written in the form:

$$\hat{\mathbf{S}}_i(\hat{x}_i) = \sum_{k=1}^{N_f} \mathbf{a}_k^T \sigma\big(\mathbf{a}_k \cdot \hat{\mathbf{d}}_i(\hat{x}_i)\big) A_k(\hat{x}_i) \tag{4.10}$$

where A_k is the area associated with the kth fiber of the section discretization, $\hat{\mathbf{d}}_i$ is the vector of generalized section strains, $\mathbf{a}_k$ is the row vector that relates the generalized section strains to the fiber stains (i.e. the product $\mathbf{a}_k \cdot \hat{\mathbf{d}}_i$ gives the strain in the kth fiber under the assumption of plane sections), while σ is the general nonlinear material constitutive law governing the stress-strain response of the fiber. To complete the flexibility-based formulation, the vector of generalized strains ($\hat{\mathbf{d}}_i$) can be related to the element end displacements, $\hat{\mathbf{D}}_i$, through the

weak form of compatibility and an appropriate integration scheme (e.g. Gauss-Lobatto) as:

$$\hat{\mathbf{D}}_i = \sum_{j=1}^{N_p} \mathbf{b}_i^{\star}(\hat{x}_i^j)^T \hat{\mathbf{d}}_i(\hat{x}_i^j) w_j \tag{4.11}$$

where N_p is the total number of integration points along the element, $\hat{x}_i^j$ is the location along the element of the jth integration point, $\mathbf{b}^{\star}$ is a matrix of displacement-dependent force interpolation functions, while w_j is the weight associated with the jth integration point.

From Eqs. (4.9) to (4.11), the element flexibility matrix can be estimated as:

$$\begin{aligned} \hat{\mathbf{f}}_i = \frac{\partial \hat{\mathbf{D}}_i}{\partial \hat{\mathbf{P}}_i} =& \frac{\partial \sum_{j=1}^{N_p} w_j \mathbf{b}^{\star}(\hat{x}_i^j) \hat{\mathbf{d}}(\hat{x}_i^j)}{\partial \hat{\mathbf{P}}_\mathbf{i}} \\ &= \sum_{j=1}^{N_p} w_j \frac{\partial \mathbf{b}^{\star}(\hat{x}_i^j)}{\partial \hat{\mathbf{P}}_i} \hat{\mathbf{d}}(\hat{x}_i) + w_j \mathbf{b}^{\star}(\hat{x}_i^j) \frac{\partial \hat{\mathbf{d}}(\hat{x}_i^j)}{\partial \hat{\mathbf{P}}_i} \end{aligned} \tag{4.12}$$

In evaluating Eq. (4.12), the first differentiation term can be estimated through a curvature-based displacement interpolation method (*De Souza*, 2000), while the second differential term can be evaluated as:

$$\frac{\partial \hat{\mathbf{d}}_i(\hat{x}_i^j)}{\partial \hat{\mathbf{P}}_i} = \frac{\partial \hat{\mathbf{d}}_i(\hat{x}_i^j)}{\partial \hat{\mathbf{S}}_i(\hat{x}_i^j)} \frac{\partial \hat{\mathbf{S}}_i(\hat{x}_i^j)}{\partial \hat{\mathbf{P}}_i} \tag{4.13}$$

The element tangent stiffness matrix $\hat{\mathbf{k}}_i$ can then be obtained as the inverse of the flexibility matrix.

To consider arbitrarily large rotations and displacements in a small deformation/strain setting, a corotational formulation can be implemented in which the basic reference system (i.e. the reference system where Eqs. (4.9) to (4.13) were derived) is considered fixed to the element as it deforms. The rotation and translation of this reference system is then described through rigid body motions. Following this formulation, the variationally consistent element tangent stiffness matrix in the global system can be expressed as:

$$\mathbf{k}_i = \mathbf{T}_i^T \hat{\mathbf{k}}_i \mathbf{T}_i + \mathbf{k}_{\mathbf{G}i} \tag{4.14}$$

where $\mathbf{T}_i$ is the matrix that transforms displacement variations in the global reference system ($\delta\mathbf{D}_i$) to those in the basic reference system ($\delta\hat{\mathbf{D}}_i$), i.e. $\delta\hat{\mathbf{D}}_i = \mathbf{T}_i\delta\mathbf{D}_i$; $\mathbf{T}_i^T\hat{\mathbf{k}}_i\mathbf{T}_i$ is the material stiffness; while $\mathbf{k}_{\mathbf{G}i}$ is the geometric stiffness matrix that is related to the variations of the rows of $\mathbf{T}_i$. For more information on the derivation of $\mathbf{k}_{\mathbf{G}i}$, the reader is referred to (*De Souza*, 2000). Once $\mathbf{k}_i$ is known for each element, the tangent stiffness matrix $\mathbf{K}_\top$ can be estimated through a standard assembly process. To implement the modeling environment outlined above in a standard nonlinear iterative solution process, the general state determination scheme outlined in (*De Souza*, 2000) can be adopted.

It should be observed that the nonlinear finite element environment of this section can be applied for the modeling of both steel and reinforced concrete systems, including structures with walls and cores (*Arabzadeh and Galal*, 2017), and can be directly implemented in OpenSees (*McKenna et al.*, 2013).

4.5.2 Structural damage

Depending on the complexity of the finite element model adopted to represent the structural system, a wide range of damage mechanisms can be explicitly modeled, including material yielding, buckling of the members, material degradation. To estimate damage to structural components not included in the finite element model (e.g. connections), or damage caused by phenomena not captured by the finite element model (e.g. local buckling), an implicit approach based on fragility can be followed. Similarly to how damage was estimated for the envelope components (Sec. 4.4.3), to model the susceptibility of a structural component to N_D damage states that can be induced by a demand parameter, $D(t)$, extracted from the structural model (e.g. interstory drift), a set of N_D sequential damage thresholds, $\mathbf{C}_D^S = \{C_{D_1} \leq C_{D_2} \leq ... \leq C_{D_{N_D}}\}$, are defined. The largest threshold to be exceeded at a given time during the wind event by $D(t)$ dictates the current damage state of the component. Uncertainty in the damage thresholds can be modeled through an appropriate set of sequential fragility functions. In particular, if it is assumed that for a given component

there is no interdependence between damage states induced by different demands (i.e. no degeneration of the damage thresholds can occur), then damage logics other than sequential can be readily included, e.g. the mutually exclusive or simultaneous damage logics outlined in (*Federal Emergency Management Agency (FEMA)*, 2012a). In the case of structural damage, the system measures of interest are the final damage states collected in the alphanumeric vector $\mathbf{DS}^S(T)$.

4.6 Simulation strategy

As outlined in Sec. 4.2, the goal of this work is to characterize the performance of the system through estimating the mean annual rate of exceeding the system measures of interest (e.g. the components of $\mathbf{DS}^E$ and $\mathbf{DS}^S$ or any output of interest from the nonlinear structural model Sec. 4.5.1) through solving Eq. (4.1). While direct Monte Carlo could be used to this end, the computational cost would be excessive. Indeed, the annual rates of interest to this work are small (in the order of 1×10^{-6}) while the models require significant computationally effort for their evaluation (e.g. the nonlinear structural model of Sec. 4.5). To overcome this, methodologies based on convolution of the system response conditioned on appropriate measures of the intensity of the wind event will be adopted. The basic idea can be traced back to work done in PBSE for the efficient estimation of the unconditional exceedance probability associated with nonlinear structural responses (*Bazzurro et al.*, 1998). Specifically, in this work, the strategy outlined in (*Ouyang and Spence*, 2020) is adopted. The hazard curve of Eq. (4.2) is therefore partitioned into $N_{\bar{v}_H}$ mutually exclusive and collectively exhaustive subevents $E_{\bar{v}_{H,k}}$. By then solving Eq. (4.1) conditioned on each subevent $E_{\bar{v}_{H,k}}$ through Monte Carlo simulation (i.e. for $\lambda(sm_i|E_{\bar{v}_{H,k}})$ with $k = 1, ..., N_{\bar{v}_H}$), unbiased estimates to Eq. (4.1) can be obtained through applying the total probability theorem, i.e. $\lambda(sm_i) = \sum \lambda(sm_i|E_{\bar{v}_{H,k}})P(E_{\bar{v}_{H,k}})$ with $P(E_{\bar{v}_{H,k}})$ the probability of the subevent $E_{\bar{v}_{H,k}}$, which can be directly estimated from the hazard curve. The computational advantage of the approach lies in how a sampling plan can be used in which the wind speed samples

are evenly spaced between rare and frequent events together with the possibility to directly implement parallel computation.

4.7 Case study

4.7.1 Archetype building

A 45-story office building located in downtown Miami is considered for studying the relative occurrence of envelope and structural damage through the proposed framework. The building has a steel structural system defined by an inner core and outer tube, as illustrated in Fig. 4.2(a), and a cladding system composed of a typical stick-built curtain wall. Outside the core, each floor is considered as open office space while the area inside the core is considered occupied by installations necessary for vertical transportation, such as elevators, corridors, and stairs. The floors are considered isolated from one another in terms of internal pressure.

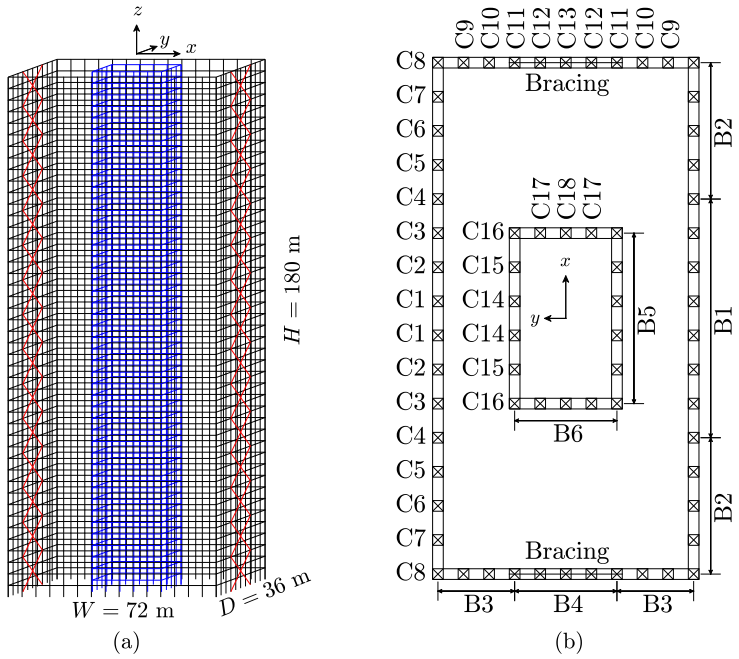

Figure 4.2: Illustration of the structural system:(a) 3D view; (b) typical grouping of the beams (groups B1 to B6) and columns (groups C1 to C18) in plan.

4.7.1.1 Structural system

The typical layout of the structural system is shown in Fig. 4.2. All columns are box sections with the mid-line width, D_i, belonging to the discrete set {0.2 m, 0.25 m ,..., 3 m} and flange thickness given by $D_i/20$. The columns are grouped vertically three floors at a time and in plan as indicated in Fig. 4.2(b). The beams and braces are designed to belong to the American Institute for Steel Construction (AISC) W24 family. Beams are grouped in plan as indicated in Fig. 4.2(b). Each group of beams extends over three consecutive floors (commencing from the first floor). Beams are therefore allowed to change over the height of the building. The X bracing is concentric, with each pair spanning three floors.

Potential damage to the beam column connections, concentric X braces, column base plates, and column splices are modeled through the fragility-based approach outlined in Sec. 4.5.2. In particular, the damage states and associated fragility functions for these components were obtained from the Federal Emergency Management Agency (FEMA) P-58 fragility database (*Federal Emergency Management Agency (FEMA)*, 2012b). In selecting the fragilities, generic components without special seismic detailing were considered. All damage states followed a sequential damage logic. Table 4.1 provides an overview of the fragility functions used to model the uncertainty in the damage thresholds. The possibility of using seismic fragilities for modeling wind damage requires some discussion. Indeed, seismic damage is in general a consequence of ultra-low-cycle fatigue, while, due to the comparatively long and repetitive nature of wind loading, wind damage is more likely a consequence of low/mid-cycle fatigue, i.e. a cumulative damage mechanism. This will in general lead to lower capacities against wind actions than can be expected for seismic actions. Having said this, it is generally known that seismic capacities are overly conservatives as a result of the experimental test protocols used in their estimation, which often require the repetition of a number of symmetric loading cycles (*Haselton et al.*, 2008; *Federal Emergency Management Agency (FEMA)*, 2009; *Haselton et al.*, 2020; *Suzuki and Lignos*, 2020). Therefore, in this work, seismic fragilities are considered as a first approximation of wind fragilities. More discussion

Table 4.1: Summary of the fragility functions used to model uncertainty in the damage thresholds associated with the envelope system.

Component	Description	Demand	Label	Median	Dispersion	Unit
One/two sided connection	Fracture of lower beam flange	Story drift	$DS^S_{C_1}$	0.017	0.4	rad
One/two sided connection	Fracture of upper beam flange	Story drift	$DS^S_{C_2}$	0.025	0.4	rad
One/two sided connection	Weld fracture and possible local buckling	Story drift	$DS^S_{C_3}$	0.03	0.4	rad
Concentric X brace	Minor initial buckling and gusset yielding	Story drift	$DS^S_{B_1}$	0.0016	0.7	rad
Concentric X brace	Brace buckling and gusset/brace yielding	Story drift	$DS^S_{B_2}$	0.01	0.3	rad
Concentric X brace	Brace fracture and gusset plate rupture	Story drift	$DS^S_{B_3}$	0.0178	0.3	rad
Base plate	Initial cracking between column/base plate	Story drift	$DS^S_{P_1}$	0.04	0.4	rad
Base plate	Minor cracking between column/base plate	Story drift	$DS^S_{P_2}$	0.07	0.4	rad
Base plate	Brittle column and/or base plate cracking	Story drift	$DS^S_{P_3}$	0.1	0.4	rad
Splice	Minor ductile fracture of weld flange splice	Story drift	$DS^S_{S_1}$	0.04	0.4	rad
Splice	Ductile fracture of weld flange splice	Story drift	$DS^S_{S_2}$	0.07	0.4	rad
Splice	Complete failure of the splice	Story drift	$DS^S_{S_3}$	0.1	0.4	rad

on potential fatigue failure will be presented in Sec. 4.7.5.2. Finally, it should be observed that, once wind specific fragilities become available, they can be directly incorporated into the proposed framework.

4.7.1.2 Envelope system

The components susceptible to damage of the building envelope are taken as the 1.2 m $\times$ 2 m dual-pane laminated glazing units of the cladding system. Each pane of glass composing the unit has a thickness of 6 mm. The units are mounted 0.5 m from the upper floor and 1.5 m from the lower floor. Any lateral stiffness provided by the system is neglected in this study. In total, 8100 units define the building envelope.

Each glazing unit is considered susceptible to two drift induced damage states. The first, indicated with $DS^E_{Dr_1}$ in the following, coincides with hairline cracking of the glass panes of the unit, while the second, $DS^E_{Dr_2}$ in the following, coincides with fracture of the glass panes. The units are also considered susceptible to the damage state DS^E_{p60} indicating glass blowout due to excessive net pressure (measured through 60 second equivalent net pressure with exponential parameter equal to 16 (*Ouyang and Spence*, 2019)). Table 4.2 provides a summary of the fragility functions. Among these damage states, DS^E_{p60} is considered as a terminal damage state for the glazing unit. Following the model of Sec. 4.4.3, interdependence between the

Table 4.2: Summary of the fragility functions used to model uncertainty in the damage thresholds associated with the envelope system.

Component	Description	Demand	Label	Median	Dispersion	Mean	Std	Unit
Glazing unit	Hairline cracking of glass	Story drift	$DS^E_{Dr_1}$	0.021	0.45	-	-	rad
Glazing unit	Glass fracture	Story drift	$DS^E_{Dr_2}$	0.024	0.45	-	-	rad
Glazing unit	Glass blowout	Equivalent pressure	DS^E_{p60}	-	-	5.29	0.91	kPa

capacity of the glazing unit to take net pressure and the current drift induced damage state is considered. In particular, the occurrence of $DS^E_{Dr_1}$ is considered to reduce the capacity threshold associated with DS^E_{p60} by a factor of 0.9, while the occurrence of $DS^E_{Dr_2}$ is considered to reduce the capacity by a factor of 0.2. To model uncertainty, these factors are taken as the expected values of truncated normal random variables of support $[0, 1]$ and standard deviation 0.1.

4.7.2 Wind Loads

4.7.2.1 Directional hurricane climate

To model the Miami hurricane climate, the model of Sec. 4.3 is calibrated to data corresponding to milepost 1450 of the directional hurricane database of the National Institute of Standards and Technology (NIST) (*National Institute of Standards and Technology*, 1980). For this milepost (corresponding to Miami) the annual rate of arrival of hurricanes is $\lambda_e = 0.55$. In fitting the model of Sec. 4.3, the site specific marginal CDF of the maximum mean hourly wind speed, $F_{\bar{V}_H}$, was taken as a Weibull distribution. After implementing the probabilistic transformation of (*Ouyang and Spence*, 2020), the resulting expected non-directional hurricane hazard curve is shown in 5.3(a) together with the wind speed partitions used in calibrating the simulation strategy of Sec. 4.6. The marginal distribution of wind direction, F_α, was estimated through fitting a circular kernel density as is illustrated in Fig. 5.3(b). In estimating the expected joint distribution, $f_{\alpha,\bar{v}_H}$, the expected bivariate copula $c_{\alpha,\bar{v}_H}$ was estimated using a non-parametric kernel density copula (*Nagler*, 2017).

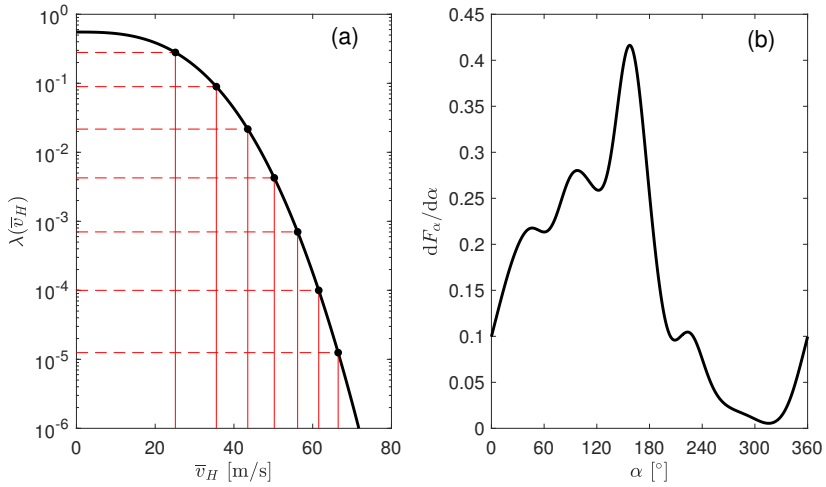

Figure 4.3: Characteristics of the Miami hurricane climate: (a) expected hurricane hazard curve; (b) marginal pdf of wind direction where α is measured counter-clockwise with $\alpha = 0°$ corresponding to wind blowing down the y direction of Fig. 4.2(b).

4.7.2.2 Aerodynamic loads

The non-Gaussian stochastic wind pressure model of Sec. 4.4.1.1 was calibrated to a dataset of the Tokyo Polytechnic University directional wind tunnel database (*Tokyo Polytechnic University*, 2008). The dataset corresponds to tests carried out on a 1/360 rigid scale model of the building in urban terrain conditions. In each test, pressure data was collected at 510 pressure taps located over the building surface at a sampling frequency of $f_w = 1000$ Hz and mean wind speed at the building top of $\bar{v}_{H_w} = 11$ m/s. Pressure coefficients, normalized to $\bar{v}_{H_w}$, were estimated every 10° commencing from the local y direction of Fig. 4.2(b), i.e. from $\alpha = 0°$. In converting the pressure coefficients to full scale, the following classic Strouhal number frequency scaling was implemented (*Simiu and Scanlan*, 1986; *Holmes*, 2001):

$$f_p = \left(\frac{\bar{v}_H}{\bar{v}_{H_w}}\right)\left(\frac{L_m}{L_p}\right) f_m \tag{4.15}$$

where f_p is the full scale sampling frequency, L_w and L_p are the characteristic lengths at wind tunnel and full scale (i.e. $L_m/L_p = 1/360$), and $\bar{v}_H$ is the target wind speed at full scale, e.g. a wind speed sample of the stochastic simulation strategy of Sec. 4.6.

In calibrating Eq. (4.6), $\tilde{\mathbf{C}}_{p,e}^{\mathcal{GP}}(t;\alpha)$ was modeled considering the first 10 spectral POD

modes of the scaled wind tunnel pressure coefficients (shown in (*Ouyang and Spence*, 2020) to provide a good representation of local wind pressures), while, to obtain a constant full scale sampling frequency (i.e. independent of the wind speed sample), interpolation of the spectral POD modes was implemented (*Ding et al.*, 2006; *Kareem*, 2008). Finally, the marginal distributions, $F_{C_{p,e}^{(n)}}(\alpha)$, were calibrated through considering 5% upper and lower tail thresholds.

4.7.3 Building design

4.7.3.1 Gravity loads

The vertical dead (D), superimposed dead (SD), and Live (L) loads considered acting at each floor of the building were estimated in accordance with the ASCE 7 standard (*American Society of Civil Engineers*, 2016). In particular, in determining these loads, the area outside the core was considered as office space while the area inside the core was considered as occupied by corridors and vertical transportation systems (elevators, stairs). The resulting area loads are reported in Table 4.3. In addition, the cladding system is considered to have a vertical surface dead load of 0.72 kPa. This load is applied to each floor after transformation to a perimeter line load. In assessing the performance of the structure through the proposed framework, the gravity loads were combined with the dynamic wind loads, W, through the following load combination (*American Society of Civil Engineers*, 2016):

$$1.2(D + SD) + F_r L + W \tag{4.16}$$

where F_r is the live load reduction factor estimated following the recommendations of ASCE 7 (*American Society of Civil Engineers*, 2016).

Table 4.3: Floorwise gravity loads.

	L [kPa]	SD [kPa]	D [kPa]
Inside the core	4.79	0.72	4
Outside the core	2.40	0.48	4

4.7.3.2 Design

The structural system is designed to satisfy the following typical serviceability and life safety performance objectives: (1) expected peak drifts under a 50-year mean recurrence interval (MRI) wind event should not exceed a drift ratio of 1/400; (2) the members of the structural system should not experience yielding under a 700-year MRI wind event (*American Society of Civil Engineers*, 2016). To satisfy these requirements, A572 steel is chosen for the box section column members, and A992 steel is selected for the W section beam and bracing members. The resulting member sizes are listed in 4.10 and result in first three natural frequencies of 0.2061 Hz, 0.2673 Hz and 0.4270 Hz (estimated from the OpenSees model of Sec. 4.7.4 with nonlinearity, both geometric and material, deactivated). In designing the structural system, four 1-hour wind loading scenarios were considered defined by calibration to non-directional 50-/700-year MRI wind speeds (estimated from the hazard curve of Fig. 5.3(a) to be $\bar{v}_H = 43.9$ m/s and $\bar{v}_H = 53.9$ m/s respectively) and wind directions of $\alpha = 0°$ and $\alpha = 90°$ (wind blowing down the x and y direction of Fig. 4.2(b)). In estimating the dynamic response for the design events, Rayleigh damping was considered so as to provide a 1.4% damping ratio for the first two modes (*Satake et al.*, 2003; *Spence and Kareem*, 2014b). To illustrate the satisfaction of the serviceability performance objective, Fig. 4.4 reports the expected (average) peak drift ratios at each corner of the building for the governing design event. For the life safety performance objective, Fig. 4.5 reports the maximum elastic stress in all the members of the structural systems for both design events (vertical loads were combined through Eq. (4.16)). As can be seen, members subject to combined bending and axial force (i.e. columns) are within the design limits suggested by AISC (*American Institute of Steel Construction*, 2010) as are members subject to pure bending (i.e. beams).

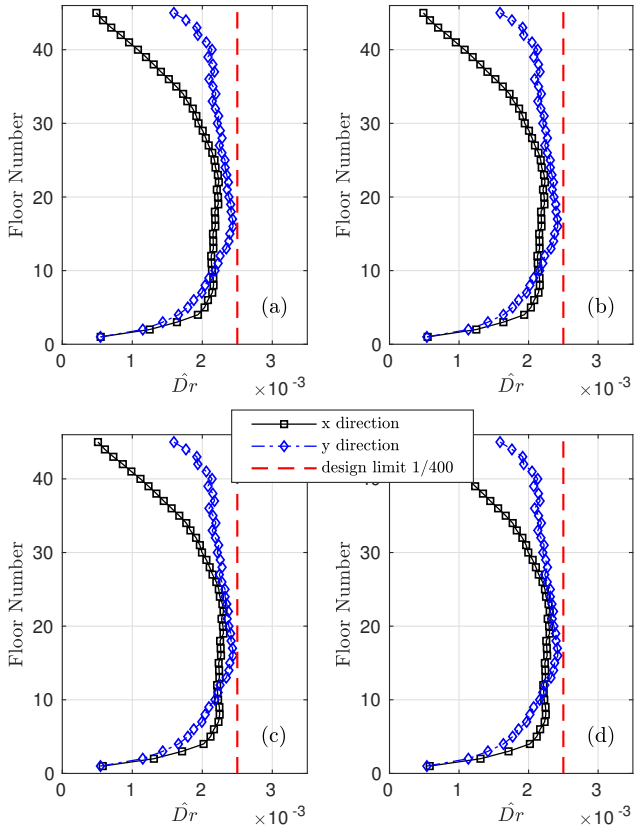

Figure 4.4: The expected peak interstory drift ratios for the serviceability design wind event associated with $\alpha = 0°$: (a) column line at $x = -36$ m and $y = 18$ m; (b) column line at $x = 36$ m and $y = 18$ m; (c) column line at $x = -36$ m and $y = -18$ m; (d) column line at $x = 36$ m and $y = -18$ m.

4.7.4 Nonlinear structural model

4.7.4.1 Model description

The nonlinear modeling environment of Sec. 4.5 is implemented in the open source software framework OpenSees (*McKenna et al.*, 2013). In particular, in creating the finite element model of the structural system, each member is modeled through one force-based beam-column element with five integration points and Gauss-Lobatto integration scheme. A fiber mesh resolution of 6×1 has been used for each section wall, flange, and web. A total of 24 fibers are therefore used for each box column member and 18 fibers for each wide flange beam/bracing memebr. The shear and torsion responses are considered to remain elastic throughout the analysis. The expected yield stress of A992 steel fibers is taken as 379 MPa,

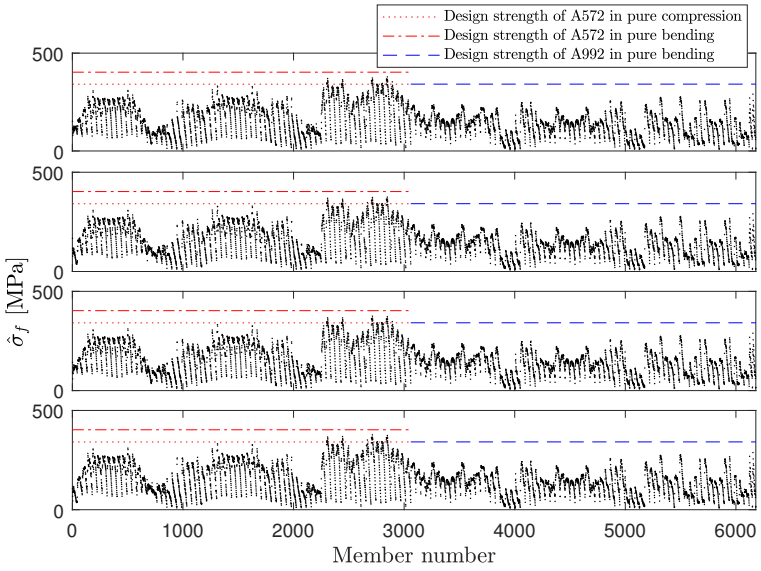

(a)

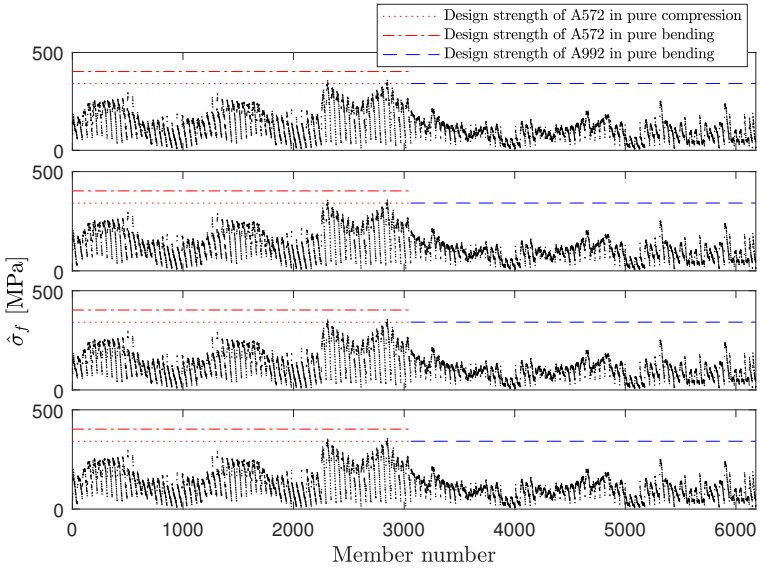

(b)

Figure 4.5: Peak fiber stresses in each member for the life safety design events: (a) $\alpha = 0°$; (b) $\alpha = 90°$.

while those of A572 is taken as 417 MPa (*Bartlett et al.*, 2003).

A bilinear model was adopted to define the stress-strain behavior with a strain hardening ratio of 0.4%. The choice of a bilinear model for the fibers was made to balance computational efficiency with overall modeling accuracy. However, it should be observed that this model does not incorporate cyclic degradation of strength and stiffness, or properly capture residual deformations/strains. More sophisticated material stress-strain models should be used if

greater detail in the nonlinear fiber behavior is desired.

Inherent damping was modeled as mass and stiffness proportional Rayleigh damping. To model uncertainty, the coefficients, $\tilde{\alpha}$ and $\tilde{\beta}$, were calibrated through imposing the condition:

$$\begin{bmatrix} \tilde{\alpha} \\ \tilde{\beta} \end{bmatrix} = 2 \begin{bmatrix} \omega_1^{-1} & \omega_1 \\ \omega_2^{-1} & \omega_2 \end{bmatrix}^{-1} \begin{bmatrix} \tilde{\zeta}_1 \\ \tilde{\zeta}_2 \end{bmatrix} \tag{4.17}$$

where ω_1 and ω_2 are the first two natural frequencies while $\tilde{\zeta}_1$ and $\tilde{\zeta}_2$ are the first two modal damping ratios that were assumed as log-normal random variables with mean 0.014 (1.4%) and coefficient of variation 0.3 (*Bernardini et al.*, 2015).

4.7.4.2 Analysis options

To ensure both efficiency and accuracy in solving Eq. (4.8) for each sample of the stochastic simulation, a dynamic updating analysis scheme was implemented based on the average constant acceleration Newmark-beta integration method. An initial time of step of $\Delta t = 0.1$ s was considered together with a modified Newton algorithm. This time step was allowed to reduce until $\Delta t = 0.01$ s. If convergence was still not achieved, a time step of $\Delta t = 0.001$ s was considered together with a Newton with line search algorithm.

4.7.5 Results

4.7.5.1 Preamble

In applying the proposed framework, the simulation strategy of Sec. 4.6 was implemented by dividing the hazard curve into the 8 wind speed subevents, $E_{\bar{v}_{H,k}}$ for $k = 1, ..., 8$, shown in Fig. 5.3(a). In particular, as suggested in (*Ouyang and Spence*, 2020), the lower bound of $E_{\bar{v}_{H,8}}$ was taken as the wind speed corresponding to an annual rate of exceedance of 1.25×10^{-5}, i.e. the failure rate associated with a risk category III building of ASCE 7 (*American Society of Civil Engineers*, 2016). The intermediate bounds between the subevents

were calculated imposing a constant squared wind speed difference. In other words, the lower and upper bound wind speeds defining each subevent, $\bar{v}_{H,k}^{L}$ and $\bar{v}_{H,k}^{U}$ respectively, were chosen so that the squared difference $(\Delta\bar{v}_{H,k})^2 = (\bar{v}_{H,k}^{U} - \bar{v}_{H,k}^{L})^2$ was constant for $k = 1, ..., 8$. In estimating the conditional rates, $\lambda(sm_i|E_{\bar{v}_{H,k}})$, 1000 samples were used for each subevent. To illustrate the role of nonlinearity/damage of the structural system, each sample is also analyzed considering a purely elastic structural model (absence of material and geometric nonlinearity) solved using a classic modal integration scheme (*Spence and Kareem*, 2013) with common random numbers. All wind events were considered to have a total duration of 1 hour to which a 200 second ramp was added at the beginning to ensure reasonable initial conditions.

In the following, response samples selected from $E_{\bar{v}_{H,8}}$ will be discussed in detail with the aim of illustrating the type of nonlinearity that can be expected under extreme wind speeds. Successively, the probabilistic damage metrics associated with the structural and envelope system will be discussed and critically compared.

4.7.5.2 Discussion on the extreme responses

Two extreme realizations from $E_{\bar{v}_{H,8}}$, indicated in the following as $\tilde{E}_{\bar{v}_{H,8}}^{(x)}$ and $\tilde{E}_{\bar{v}_{H,8}}^{(y)}$, are discussed in detail in this section. In particular, $\tilde{E}_{\bar{v}_{H,8}}^{(x)}$ corresponds to a maximum mean hourly wind speed of $\bar{v}_H = 77.45$ m/s with direction $\alpha = 200°$ and produced the largest observed central x direction top floor displacement (-2.1 m) while $\tilde{E}_{\bar{v}_{H,8}}^{(y)}$ corresponds to a maximum mean hourly wind speed of $\bar{v}_H = 68.58$ m/s and direction $\alpha = 0°$ and was responsible for the largest observed central y direction top floor response (1.9 m). The non-directional annual rates of these winds are estimated from the hazard curve of Fig. 5.3(a) to be 4.36×10^{-8} and 4.36×10^{-6} respectively.

Figures 4.6 and 4.7 report the central x and y displacements at the building top for $\tilde{E}_{\bar{v}_{H,8}}^{(x)}$ and $\tilde{E}_{\bar{v}_{H,8}}^{(y)}$ together with their linear elastic counterparts. As can be seen, the major difference between the responses is in terms of the residual displacements at the end of the events, as

illustrated through the 10 minute moving averages. In particular, for $\tilde{E}^{(x)}_{\bar{v}_{H,8}}$ (Fig. 4.6), residual displacements of -0.43 m and -0.35 m are seen in the x and y directions respectively. For $\tilde{E}^{(y)}_{\bar{v}_{H,8}}$ (Fig. 4.7), no discernible residual displacement is seen in the x direction, while in the y direction a residual of displacement of 0.41 m is seen. These results correspond to residual drift ratios of under 0.25% and therefore are unlikely to require significant repair actions (*Federal Emergency Management Agency (FEMA)*, 2012a). It is interesting to observe how residuals of similar magnitude can occur for wind loads generating a zero mean acrosswind type response, Fig. 4.6(a), as well as wind loads that cause a significant mean alongwind type response, Figs. 4.6(b) and 4.7(b). From Figs. 4.6 and 4.7, it can also be seen that the fluctuations around the moving averages are of similar magnitude between the linear elastic and fully nonlinear models.

Figure 4.8 reports the peak absolute strains occurring in each member for $\tilde{E}^{(x)}_{\bar{v}_{H,8}}$ and $\tilde{E}^{(y)}_{\bar{v}_{H,8}}$. As can been seen, significant yielding is expected in both the columns (members 1 to 3060) and beams/braces (members 3061 to 6180) of the system. To illustrate how yielding is distributed in the structural system, Fig. 4.9 provides a 3D map of the yielded members, from which it can be seen that significant yielding is occurring in the bottom 2/3 of the structure and involves both the core and outer tube.

To illustrate the typical yielding behavior of individual members, Figs. 4.10(a)-(b) report the stress and strain time histories for the critical fiber of a column experiencing significant yielding during the event $\tilde{E}^{(x)}_{\bar{v}_{H,8}}$, while Figs. 4.10(c)-(d) reports analogous information for a beam during $\tilde{E}^{(x)}_{\bar{v}_{H,8}}$. In particular, with reference to Fig. 4.2(b), for $\tilde{E}^{(x)}_{\bar{v}_{H,8}}$, the response of column C_4 of the 4th quadrant on the 23rd floor is reported, while, for $\tilde{E}^{(y)}_{\bar{v}_{H,8}}$, the response of beam B_3 between columns C_{10} and C_{11} of the 2nd quadrant of floor 12 is reported. From Fig.4.10, it is interesting to observe that significant material yielding occurs in bursts associated with short duration wind gusts rather than gradually over the duration of the event. In some cases, as illustrated Figs. 4.10(c)-(d), the majority of yielding is occurring due to a single wind gust (occurring 1740 seconds after the beginning of the wind event in this

case). This type of yielding behavior was seen in all fibers experiencing material nonlinearity and indicates the importance of modeling the peaks in wind loads accurately, including non-Gaussian effects, if the nonlinear response is to be properly captured. Figure 4.11 reports the stress-strain curves for the two fibers of Fig. 4.10 and illustrates how fibers can experience behavior ranging from alternating plasticity (Fig. 4.10(a)) to ratcheting (Fig. 4.10(b)). Both these behaviors could lead to potential fiber failure. Concerning the ratcheting behavior, the observed maximum strains (less than 5×10^{-2}) would suggest that fiber fracture due to incremental plasticity is unlikely. With respect to alternating plasticity, low-cycle fatigue could potentially lead to failure due to fracture. To preliminarily investigate this, the 20 members with the largest peak absolute strain values were analyzed in more detail. While, for $\tilde{E}^{(x)}_{\bar{v}_{H,8}}$, none of the members experienced alternating plasticity, for $\tilde{E}^{(x)}_{\bar{v}_{H,8}}$ 9 members formed cycles of alternating plasticity. The maximum number of cycles was 58, which would suggest low-cycle fatigue failure is unlikely to occur in this case (*Pereira et al.*, 2014).

4.7.6 Probabilistic Damage Metrics

4.7.6.1 Structural damage

As outlined in Sec. 4.5.2, structural damage can be explicitly modeled through the finite element model of the structural system. In this respect, Fig. 4.12 reports the annual exceedance rate associated with the total number of members experiencing yielding. As can be seen, first yield tends to occur in the columns with an exceedance rate of around 4×10^{-4}, which corresponds to a MRI of approximately 2500 years. This is somewhat more conservative than the design requirements of Sec. 4.7.3.2, due primarily to directional wind effects that were neglected in the design process. From Fig. 4.12, it can be seen that at an annual exceedance rate of 1×10^{-6} (which will be the occurrence rate of the wind hazard maps suggested in the commentary of the upcoming ASCE 7-22 for performance-based wind analysis), over 900 members have experienced yielding. This corresponds to around 15% of the members (total number of members in the system is 6180) with yielding evenly distributed

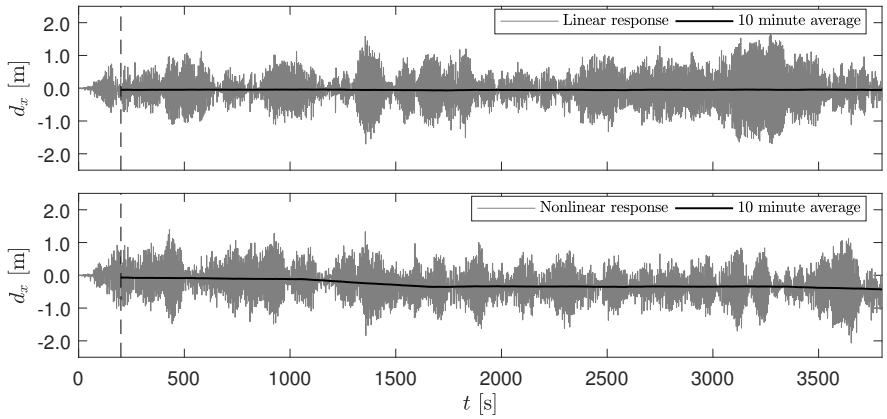

(a)

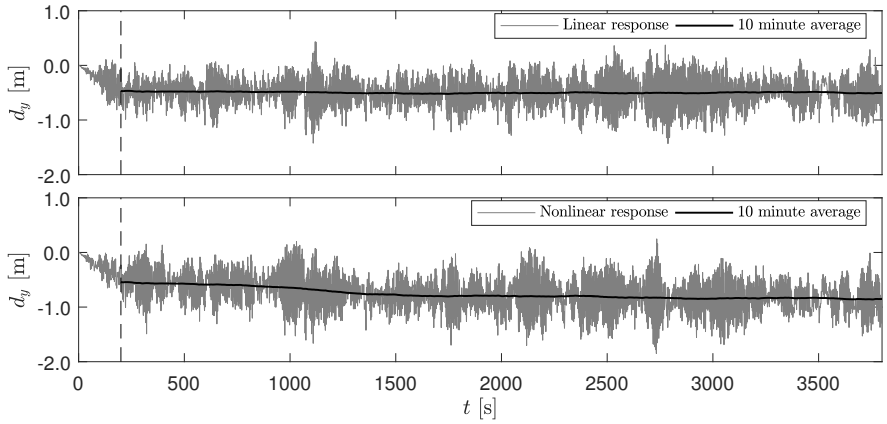

(b)

Figure 4.6: Top floor central displacement time histories for $\tilde{E}^{(x)}_{\bar{v}_{H,8}}$ (vertical dashed line indicates the end of the 200-second load ramp): (a) x direction response; (b) y direction response.

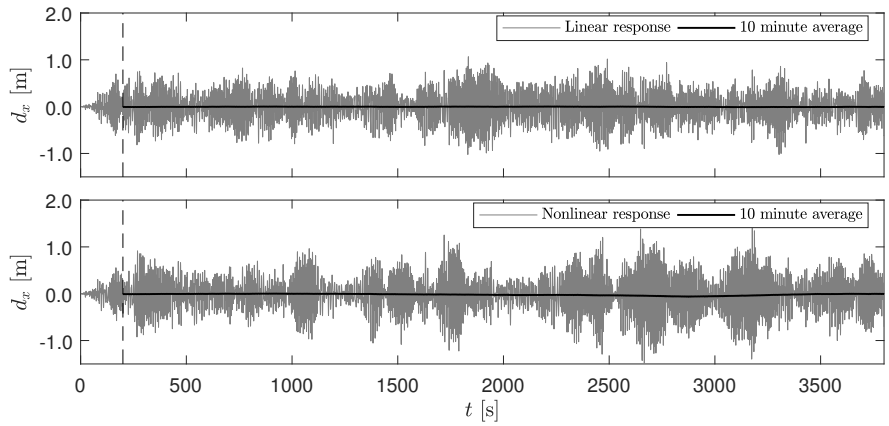

(a)

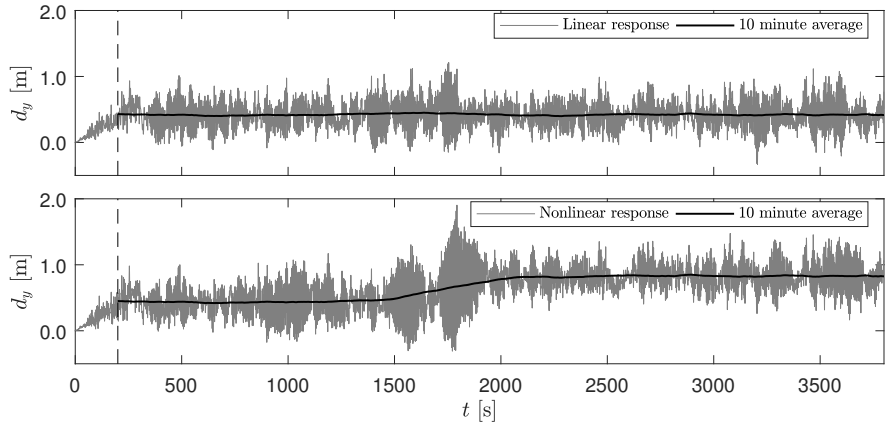

(b)

Figure 4.7: Top floor central displacement time histories for $\tilde{E}^{(y)}_{\bar{v}_{H,8}}$ (vertical dashed line indicates the end of the 200-second load ramp): (a) x direction response; (b) y direction response.

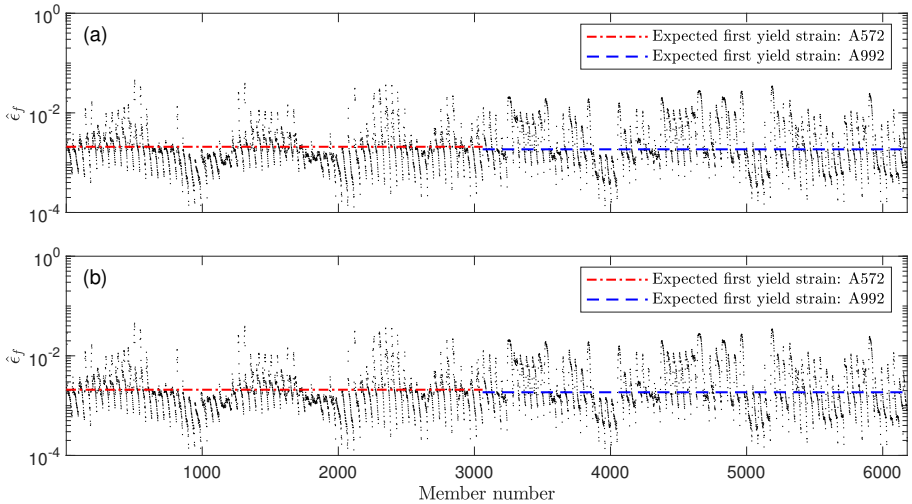

Figure 4.8: Absolute peak fiber strains in each member: (a) event $\tilde{E}^{(x)}_{\bar{v}_{H,8}}$; (b) event $\tilde{E}^{(x)}_{\bar{v}_{H,8}}$.

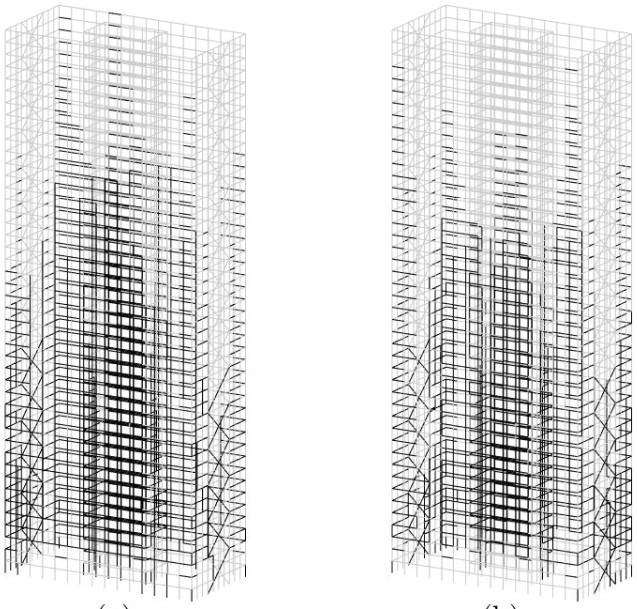

Figure 4.9: 3D illustration of yielding in the structural system: (a) event $\tilde{E}^{(x)}_{\bar{v}_{H,8}}$; (b) event $\tilde{E}^{(y)}_{\bar{v}_{H,8}}$.

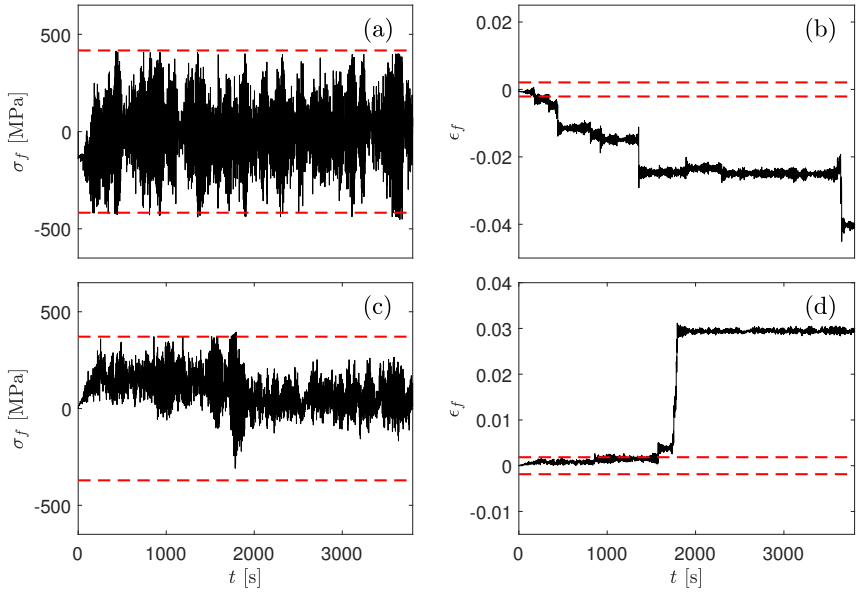

Figure 4.10: Representative stress and strain responses in critical fibers during $\tilde{E}^{(x)}_{\bar{v}_{H,8}}$ and $\tilde{E}^{(y)}_{\bar{v}_{H,8}}$ (dashed lines indicate first yield limits): (a) stress history for $\tilde{E}^{(x)}_{\bar{v}_{H,8}}$; (b) strain history for $\tilde{E}^{(x)}_{\bar{v}_{H,8}}$; (c) stress history for $\tilde{E}^{(y)}_{\bar{v}_{H,8}}$; (c) strain history for $\tilde{E}^{(y)}_{\bar{v}_{H,8}}$.

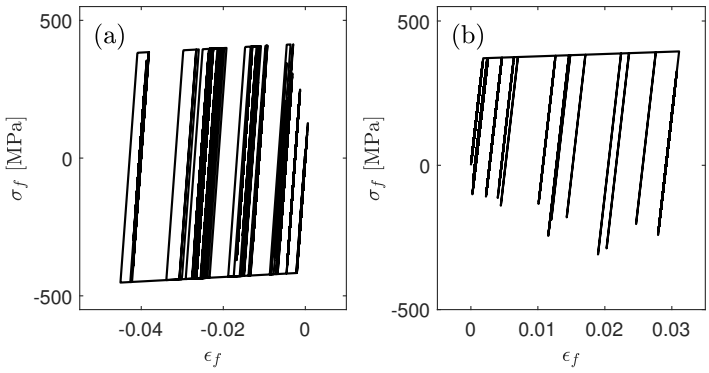

Figure 4.11: Stress-strain curves for the representative fibers of Fig. 4.10: (a) fiber of $\tilde{E}^{(x)}_{\bar{v}_{H,8}}$; (b) fiber of $\tilde{E}^{(y)}_{\bar{v}_{H,8}}$.

between beams and columns. To investigate the consequence of this yielding on the integrity of the structural system, Fig. 4.13 reports the exceedance rates associated with the peak absolute strains occurring in the system. As can be seen, for an exceedance rate of 1×10^{-6}, peak strains of less than 0.015 are seen, therefore suggesting fiber fracture due to incremental plasticity is unlikely. To quantify the overall integrity of the structural system after yielding, Table 4.4 reports the maximum interstory drift ratios over the building height in both the x and y directions. As can be seen, drift ratios do not exceed 1% at annual rates of 1×10^{-6}. From the damage thresholds for steel structures reported in (*Wen and Kang*, 2001), this level of peak interstory drift is expected to produce only light to moderate damage.

With respect to damage modeled implicitly through the fragility functions of Table 4.1, Fig. 4.14 reports the annual exceedance rates associated with the total number of beam column connections and braces experiencing damage. As can be seen from Fig. 4.14(a), connections are likely to experience damage at rates similar to that seen for yielding in the members, with around 8% of connections (total number of connections in the structure is 3060) experiencing at least $DS^S_{C_1}$ at annual rates of 1×10^{-6}. It is interesting to observe that $DS^S_{C_3}$, which may be considered a severe damage state for a connection, has a first annual occurrence rate of just over 1×10^{-5}. Therefore, while very unlikely, severe damage to the connections could occur. Figure 4.14(b) reports the annual exceedance rates associated with the braces. As can be seen, all braces are likely to experience some damage in extreme wind

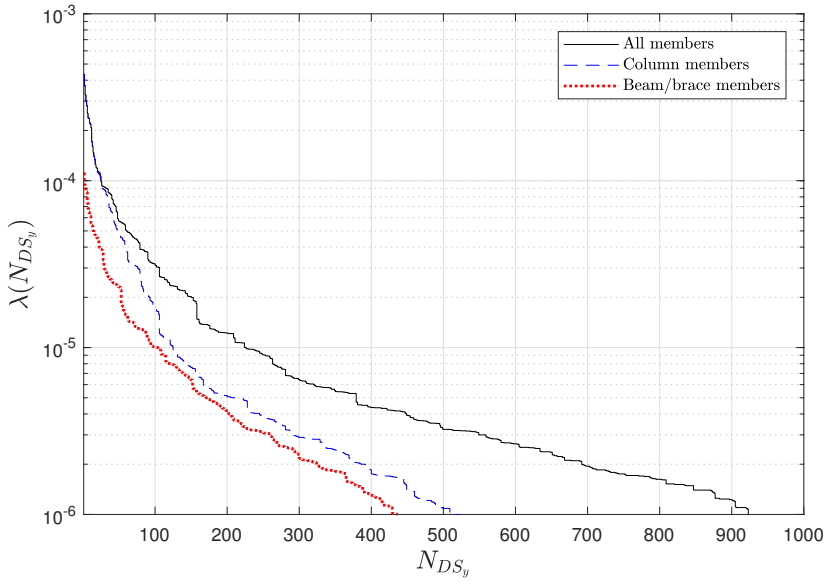

Figure 4.12: Mean annual exceedance rate associated with the total number of members experiencing yielding.

Table 4.4: Maximum interstory drift ratios for specified annual exceedance rates.

	$\max(\hat{Dr}_x)$ [%]	$\max(\hat{Dr}_y)$ [%]
$\lambda = 1 \times 10^{-4}$	0.63	0.55
$\lambda = 1 \times 10^{-5}$	0.81	0.71
$\lambda = 1 \times 10^{-6}$	0.99	0.87

events. However, even for annual rates as low as 1×10^{-6}, the severe damage state, $DS^S_{C_1}$, did not occur. For the column splices and base plates, no damage was observed.

4.7.6.2 Envelope damage

Figure 4.15 reports the annual exceedance rate associated with having $N_{DS^E_{P_{60}}}$ envelope components assume $DS^E_{P_{60}}$ of Table 4.2 as a final damage state. From Fig. 4.15, it can be seen that first window blowout occurs with a rate of around 1.9×10^{-3}, which corresponds to a MRI of just over 500 years. For an exceedance rate of 1×10^{-6}, around 250 components

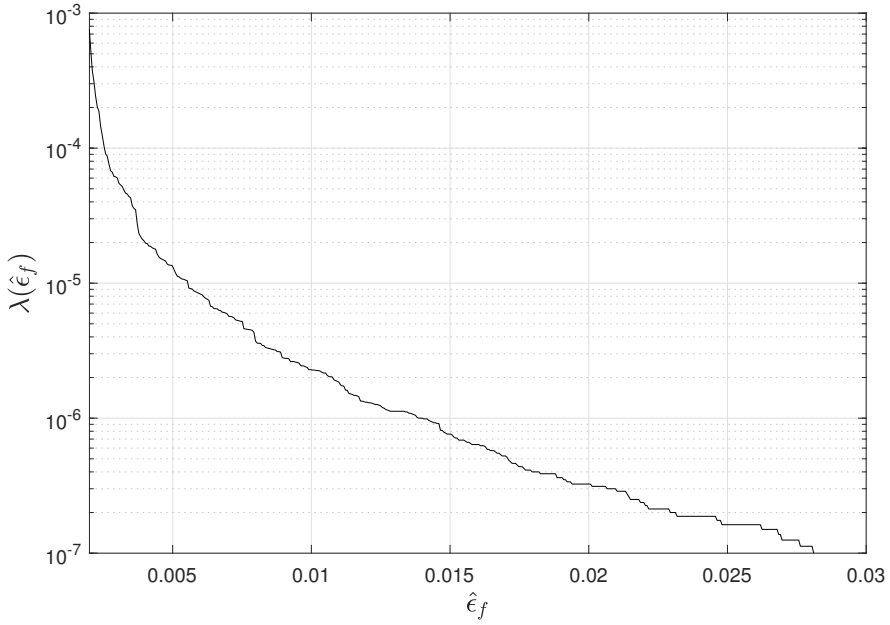

Figure 4.13: Mean annual exceedance rate associated with the peak absolute strains occurring in the system.

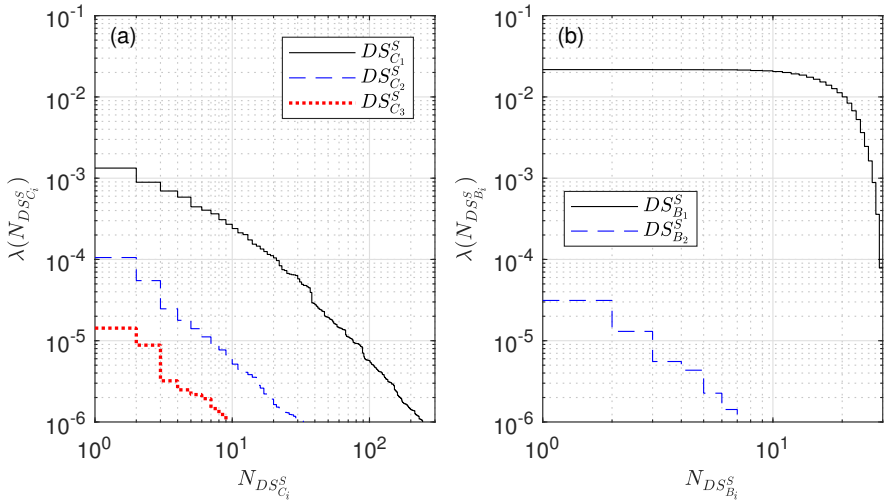

Figure 4.14: Mean annual exceedance rates associated with the connection and brace damage states: (a) connections; (b) braces.

(3% of the 8100 envelope components of the system) are expected to have been lost due to net pressure blowout. Figure 4.16 reports the number of envelope components expected to assume one of the two drift induced damage states of Table 4.2 at the end of the wind event. As can be seen, at an annual rate of 1×10^{-6} around 1.6% of the components will assume a drift induced final damaged state with around 0.6% assuming $DS^E_{Dr_2}$. These results confirm how in general local dynamic net pressure damage will exceed damage induced by excessive drift.

To illustrate the influence of geometric and material nonlinearity on envelope damage, Fig. 4.15 also reports the annual exceedance rates associated with considering a linear structural behavior in determining the drift demands for the envelope components. As can be seen, this assumption results in a noticeable reduction in the number of components experiencing damage. To quantify this difference, Fig. 4.17(a) shows how the relative error (in terms of underestimation) in λ induced by this assumption can exceed 20% for thresholds associated with low exceedance rates. For comparison, Fig. 4.15 also reports the annual exceedance rate associated with $DS^E_{P_{60}}$ when coupling between the drift and net pressure induced damage states is neglected (i.e. the occurrence of a drift induced damage state is not considered to reduce the capacity of the glazing panels to resist dynamic net pressure). From 4.17(a), it can be observed that this can result in relative errors (strictly underestimates) of λ of well over 50%. This illustrates the importance of considering coupled demand analysis when estimating the performance of the envelope system. Finally, Fig. 4.16 illustrates the effects of considering linear structural models in estimating the demands used in determining the annual exceedance rate of drift induced damage to the envelope. As expected, significant underestimates in λ are seen for both $DS^E_{Dr_1}$ and $DS^E_{Dr_2}$. Indeed, from 4.17(b), relative errors (in terms of underestimation) in λ of around 50% can be seen over all thresholds.

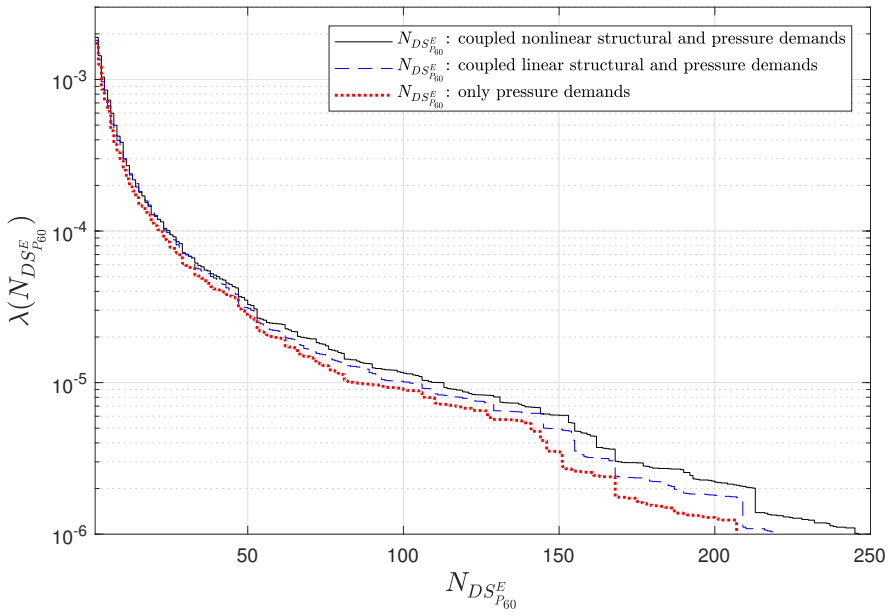

Figure 4.15: Mean annual exceedance rate of the total number of envelope components in $DS^E_{P_{60}}$ at the end of the wind event.

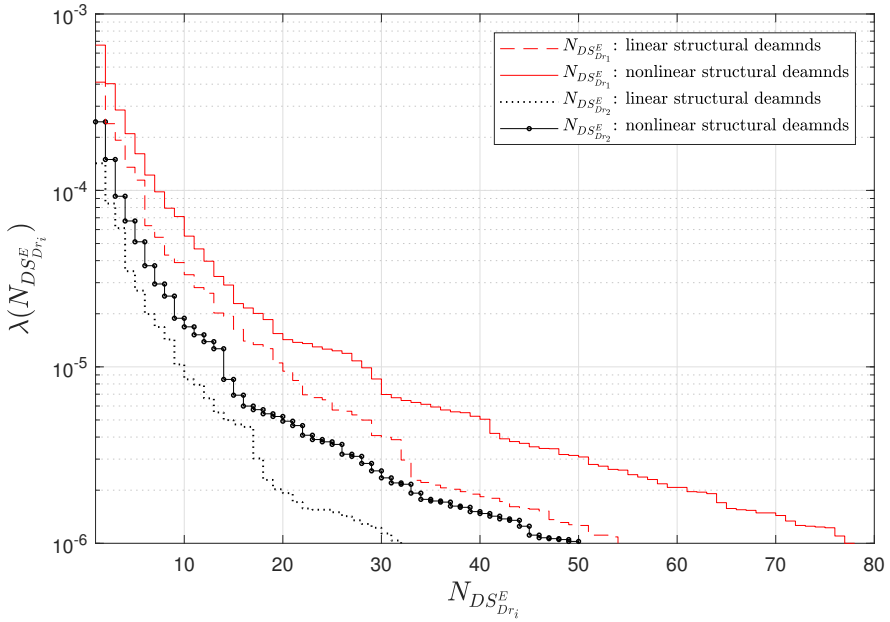

Figure 4.16: Mean annual exceedance rate of the total number of envelope components in $DS^E_{Dr_1}$ and $DS^E_{Dr_2}$ at the end of the wind event.

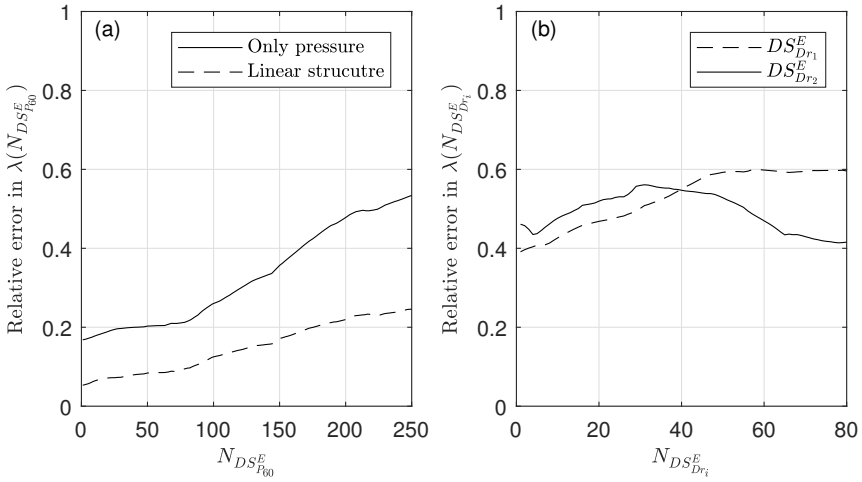

Figure 4.17: Relative error in the exceedance rates of the total number of envelope components in DS^E_{P60}, $DS^E_{Dr_1}$ or $DS^E_{Dr_2}$: (a) relative error associated with DS^E_{P60}; (b) relative error associated with $DS^E_{Dr_1}$ and $DS^E_{Dr_2}$.

4.7.6.3 Observations

From the results of Secs. 4.7.6.1 and 4.7.6.2, the following observations can be made: 1) the structural system will experience significant yielding (up to 15% of the structural members of the case study) for wind events with exceedance rates superior to those used in design; 2) while undergoing noticeable yielding, the structural system is unlikely to experience significant damage, even for annual rates as low as 1×10^{-6}; 3) as expected, the envelope damage is far superior in severity as compared to that of the structural system (in the case study, around 3.6% of the envelope components experienced severe damage as compared to 0.3% of connections in structural system); 4) structural damage, in terms of material yielding/hysteresis estimated in a geometrically nonlinear setting, will generally cause a non-negligible increase in the probability of envelope damage (a 20% increase in the annual rate of envelope damage was seen in the case study). Additionally, it is interesting to observe how the envelope system was seen to be primarily intact even for events with annual rates as low as 1×10^{-6}. Overall, these observations would suggest that wind excited structures designed to typical performance criteria are potentially more resilient than systems designed to resist other natural hazards, such as earthquakes, where significant damage is generally expected

for annual rates in the order of 1×10^{-6}.

4.8 Summary and conclusions

This paper outlined a probabilistic performance-based wind engineering framework for estimating the damage to the structural and envelope system of engineering buildings subject to extreme winds. The framework was based on integrating a recently introduced probabilistic model for estimating the damage to envelope systems of engineered buildings with a nonlinear finite element modeling environment for estimating the response of the structural system within the setting of material yielding/hysteresis and large deformations. To enable efficient consideration of small failure rates, the framework was housed in a conditional stochastic simulation algorithm. To illustrate the framework and to shed light on the nonlinear performance of typical structural and envelope systems at annual exceedance rates as low as 1×10^{-6}, the response of a 3D steel archetype building located in Miami, FL, and subject to a fully directional description of the hurricane climate was investigated. The building was carefully designed so as to satisfy commonly adopted serviceability and life safety performance criteria. To ensure the proper capture of aerodynamic phenomena such as vortex shedding, the external pressures were modeled through a non-Gaussian stochastic pressure model that was calibrated to specific wind tunnel data. A full rage of damage states were defined for both the structural and envelope system through appropriate fragility functions. Through the analysis of the probabilistic performance metrics obtained from the proposed framework, the structural system was seen to experience significant yielding for response levels approaching annual rates of 1×10^{-6}. However, this yielding only resulted in light/moderate damage. With respect to the performance of the envelope system, it was seen to remain primarily functional during extreme events and to be noticeably influenced by the occurrence of structural damage.

4.9 Acknowledgment

The research effort was supported by the National Science Foundation (NSF) under Grant No. CMMI-1562388. This support is gratefully acknowledged.

4.10 Appendix

Appendix B.1. Member sizes for the case study structure

The member assignments for each of the 375 design groups defined in Sec. 4.7.1.1 and Fig. 4.2(b) are reported in Table 4.1. In particular, group B7 of Table 4.1 is associated with the bracing of the left and right face of the building.

Table 4.1: Member section assignments for the steel structure of the case study. W24 sections are identified through their weight per unit length using imperial units. Box sections are identified in terms of their mid-line width in cm.

Group	Floor Number														
Number	1-3	4-6	7-9	10-12	13-15	16-18	19-21	22-24	25-27	28-30	31-33	34-36	37-39	40-42	43-45
B1	146	146	146	146	162	162	146	162	131	131	131	131	131	131	131
B2	162	370	370	370	370	370	370	306	306	250	192	192	162	192	192
B3	450	408	492	492	450	450	450	450	492	450	450	408	250	207	192
B4	335	408	408	408	450	450	450	408	370	370	306	279	229	192	176
B5	176	250	250	229	192	176	176	176	162	162	162	162	146	146	146
B6	335	335	306	306	279	279	250	250	279	229	207	192	192	162	162
B7	192	176	162	146	146	162	207	229	229	229	229	176	131	76	94
C1	55	50	50	50	50	50	45	45	45	45	45	45	45	45	45
C2	55	50	50	50	50	50	45	45	45	45	45	45	45	45	50
C3	55	50	50	50	55	50	50	50	45	50	50	45	50	50	50
C4	60	55	50	60	55	55	50	50	50	50	50	50	50	50	50
C5	60	55	55	60	60	55	55	55	55	55	55	50	55	50	55
C6	70	70	70	65	65	65	65	60	60	60	60	55	55	55	55
C7	80	80	80	80	80	75	75	70	70	70	65	65	60	60	60
C8	175	125	105	105	90	90	85	75	75	70	65	65	60	60	55
C9	85	90	90	85	85	85	85	85	80	80	75	75	70	60	55
C10	90	85	85	90	85	80	80	80	85	80	80	75	70	65	55
C11	110	80	75	80	80	75	75	75	75	70	70	70	65	65	55
C12	55	75	75	75	75	75	70	70	70	65	60	55	60	55	50
C13	65	70	70	70	75	75	75	70	70	65	65	65	60	60	60
C14	65	65	60	60	55	55	50	50	50	50	50	50	50	45	45
C15	65	60	60	60	55	55	55	55	55	50	50	50	50	50	50
C16	160	100	90	80	70	65	60	55	55	55	50	50	50	50	50
C17	80	80	80	75	70	65	60	55	55	60	55	55	50	50	45
C18	70	75	70	65	65	65	65	65	65	65	65	60	60	55	55

CHAPTER V

A Performance-Based Wind Engineering Framework for Engineered Building Systems Subject to Hurricanes[1]

Abstract

Over the past decade, significant research efforts have been dedicated to the development of performance-based wind engineering (PBWE). Notwithstanding these efforts, frameworks that integrate the damage assessment of the structural and envelope system are still lacking. In response to this need, the authors have recently proposed a PBWE framework that holistically treats envelope and structural damages through progressive multi-demand fragility models that capture the inherent coupling in the demands and damages. Similar to other PBWE methodologies, this framework is based on describing the hurricane hazard through a nominal straight and stationary wind event with constant rainfall and 1-hour duration. This paper aims to develop a PBWE framework based on a full description of the hurricane hazard in which the entire evolution of the storm track and time-dependent wind/rain fields is simulated. Hurricane induced pressures impacting the building envelope are captured through the introduction of a non-stationary/-straight/-Gaussian wind pressure model. Time-dependent

[1]Ouyang, Z., & Spence, S. M. (2021). A performance-based wind engineering framework for engineered building systems subject to hurricanes. Draft manuscript prepared for submission.

wind-driven rain is modeled through a CFD-based Eulerian multiphase framework with an interpolation scheme for the rapid computation of wind-driven rain intensities over building surface. Through the development of a conditional stochastic simulation algorithm, envelope performance is efficiently characterized through probabilistic metrics associated with rare events of design interest. The framework is demonstrated through analyzing a 45-story archetype building located in Downtown Miami, FL, for which envelope performance is estimated in terms of a suite of probabilistic damage and loss metrics. A thorough comparative study is carried out in order to provide insight into the differences that can occur due to the use of nominal hurricane models.

5.1 Introduction

Performance-based design (PBD) has been widely accepted as a rational way of assessing risks to engineered facilities subjected to natural hazards (*Porter*, 2003). Over the past decade, significant research effort has been placed on the development of frameworks for the performance-based assessment of wind-excited buildings (*Ciampoli et al.*, 2011; *Smith and Caracoglia*, 2011; *Petrini, F. and Ciampoli, M.*, 2012; *Chuang and Spence*, 2017; *Cui and Caracoglia*, 2018; *Ierimonti et al.*, 2019; *Ouyang and Spence*, 2019, 2020, 2021). Most frameworks developed to date assess damage and loss to the building system based on demands estimated exclusively from the structural response (e.g. peak interstory drifts, accelerations) notwithstanding how a significant portion of envelope damage is generated from local dynamic wind pressure. In an attempt to address this, the authors have recently a PBWE framework in which damage is estimated through a progressive damage analysis in which coupled structural response and wind pressure demands are considered as input to a multi-demand fragility analysis that captures damage state interdependency *Ouyang and Spence* (2019, 2020, 2021). Similarly to existing PBWE methodologies, this framework adopted a nominal hurricane hazard based on the assumption of a straight (i.e. constant wind direction) and stationary wind event of 1-hour duration. The intensity of the wind event was

characterized through the maximum hourly-mean wind speed to occur at the building top. Likewise, the intensity of the concurrent rain event was characterized through the maximum horizontal rainfall to occur during the hurricane at the site of interest. While this nominal hurricane setting simplifies subsequent damage and loss analysis, the relative accuracy of performance assessments based on nominal hurricanes, as compared to those carried out considering the full non-straight/-stationary nature of hurricane winds and concurrent rainfall, remains unknown.

To fill in this knowledge gap, this work develops a PBWE framework for the performance assessment of envelope systems based on describing the full evolution of the hurricane event through parametric hurricane models for both the wind and concurrent rainfall fields. In particular, hurricane tracks are described through the probabilistic parametric models outlined in (*Vickery and Twisdale*, 1995a; *Vickery et al.*, 2000b; *Cui et al.*, 2021) while the associated wind fields are described through the 2-dimensional wind field model outlined in (*Vickery and Twisdale*, 1995b; *Vickery et al.*, 2000a; *Jakobsen and Madsen*, 2004). These models are subsequently combined with parametric precipitation models (e.g. *Lonfat et al.*, 2007; *Snaiki and Wu*, 2018; *Brackins and Kalyanapu*, 2020; *Grieser and Jewson*, 2012; *Geoghegan et al.*, 2018) that use as input a subset of the hurricane model input parameters therefore enabling a probabilistic description of concurrent horizontal rainfall intensity. The consideration of continuously time varying hurricane inputs (i.e. evolving storm track and horizontal rainfall intensity) requires a new set of models for the simulation of the aerodynamic loads and wind-driven rain. To this end, a novel wind-tunnel informed proper orthogonal decomposition (POD)-based non-straight/-stationary/-Gaussian wind pressure simulation framework is introduced. For the wind-driven rain, the Eulerian-Multiphase computational fluid dynamics (CFD) model outlined in (*Kubilay et al.*, 2013, 2015a) is adopted with an interpolation scheme within the space of the wind speed and direction, therefore, allowing for the efficient estimation of the instantaneous rainwater deposition on the building envelope in terms of the continually varying wind speed and direction.

To demonstrate the applicability of the framework, a 45-story archetype building located in downtown Miami, FL, is studied in terms of probabilistic performance metrics associated with envelope damages, monetary losses, and water ingress. A comprehensive comparison of the results with those obtained by considering a nominal hurricane setting is also carried out with the aim of better understanding the feasibility of using classic hurricane hazard models in the PBWE of engineered building systems.

5.2 The performance-based wind engineering setting

Pioneered by the Pacific Earthquake Engineering Research (PEER) center (*Porter*, 2003), frameworks for probabilistic performance-based earthquake engineering have been widely adopted as the basis for developing frameworks for PBWE. The current work is developed based on the recently proposed PBWE framework outlined in (*Ouyang and Spence*, 2020), the implementation of which enables the estimation of probabilistic building envelope performance metrics of interest to stakeholders (e.g. expected repair costs, expected water ingress, etc) based on a nominal, as defined in Sec. 5.1, description of the hurricane hazard. In particular, this framework is based characterizing performance through solving the following probabilistic integral:

$$\begin{aligned}\lambda(dv) = \iiiint & G(dv|sm)|dG(sm|R_h, \alpha_H, \bar{v}_H)| \\ & |dG(R_h|\alpha_H, \bar{v}_H)||dG(\alpha_H|\bar{v}_H)||d\lambda(\bar{v}_H)|\end{aligned} \tag{5.1}$$

where G = the complementary cumulative distribution function (CCDF), sm = the system measure variables (e.g. number of damaged components and amount of water ingress), R_h = the hourly-mean rainfall intensity, α_H = wind direction, $\bar{v}_H$ = the maximum hourly-mean wind speed measured at a height of interest (e.g. building top), dv = decision variable threshold of interest (e.g thresholds related to repair costs, downtime, volume of water ingress), and λ is the mean annual rate of exceeding a threshold of interest, therefore, resulting in $\lambda(\bar{v}_H)$

representing the non-directional hurricane hazard curve and $\lambda(dv)$ representing the loss or water ingress curves.

For the hurricane framework proposed in this paper, Eq. (5.1) cannot be directly adopted as the hurricane inputs of wind speed, wind direction, and rainfall intensity are all time-dependent. To capture these variations Eq. (5.1) can be reformulated as:

$$\lambda(dv) = \iiint G(dv|sm)|dG(sm|\Theta)||dG(\Theta|\bar{v}_H)||d\lambda(\bar{v}_H)| \tag{5.2}$$

where Θ is a parameter vector defining the time-dependent hurricane track (to which non-stationary/-straight/-Gaussian wind pressures will be associated) with $\bar{v}_H$ the maximum non-directional mean hourly wind speed to occur at the site of interest over the duration of the hurricane. In Eq. (5.1) the system measures (sm) are evaluated conditional on a full hurricane event and therefore the parameters in Θ. The evaluation of Eq. (5.2) for the envelope performance can be decomposed into three fundamental stages:

1. Hurricane hazard analysis, in which the terms $G(\Theta|\bar{v}_H)$ and $\lambda(\bar{v}_H)$ are estimated for different hurricane intensities measured in terms of $\bar{v}_H$.

2. Responses analysis, in which the structural and aerodynamic responses are simulated based on the hurricane parameter vector Θ to estimate $G(sm|\Theta)$.

3. Loss and consequence analysis, in which the estimations of sm are translated into probabilistic measures of monetary losses and volumes of water ingress through the term $G(dv|sm)$.

5.3 Hurricane hazard analysis

5.3.1 Full hurricane model

5.3.1.1 Storm track model

The simplified storm track model outlined in (*Vickery and Twisdale*, 1995a) is adopted to simulate hurricanes making landfall at a site of interest. In this model, a hurricane risk region is first formed through a circular subregion centered at a location of interest (e.g. building location). Hurricane tracks are subsequently modeled as straight lines crossing the subregion. Within this context, the hurricane lifetime begins when the hurricane center enters the subregion and ends when it leaves the subregion. In this model, the distance vector between the site of interest and the hurricane center, $\mathbf{r}_s$, at any given time t during the hurricane event is defined as:

$$\begin{aligned}\mathbf{r}_s(t) = &\left(\cos\theta \cdot d_{min} - \sin\theta\sqrt{R_s^2 - d_{min}^2} + c \cdot \sin\theta \cdot t\right) \cdot \mathbf{e} \\ &+ \left(-\sin\theta \cdot d_{min} - \cos\theta\sqrt{R_s^2 - d_{min}^2} + c \cdot \cos\theta \cdot t\right) \cdot \mathbf{n}\end{aligned} \tag{5.3}$$

where d_{min} is the minimum distance between the hurricane center and the site of interest (taken positive if the site of interest sits to the left of the hurricane track and negative otherwise), R_s is the diameter of the subregion centered at the site of interest, θ is the angle between the storm track and the north direction, and $\mathbf{e}$ and $\mathbf{n}$ are the unit vectors pointing towards East and North.

5.3.1.2 Wind field model

The parametric model proposed in (*Jakobsen and Madsen*, 2004) is adopted to model the hurricane wind velocity field. The implementation of this wind field model is coupled with the hurricane track input vector Θ through the initial central pressure difference (Δp_0) and the radius of the maximum wind (r_M). In this model, the hurricane wind field at 500 m

above the sea at time t is solved for the tangential and radial velocity components through as:

$$\begin{aligned}\mathbf{v}_c(r,\beta,t) =& v_M(t)\left[\sqrt{r'^{-B}\exp(1-r'^{-B})+a^2r'^2}-ar'\right] \\ &\cdot(\sin\beta\cdot\mathbf{e}-\cos\beta\cdot\mathbf{n})\end{aligned} \tag{5.4}$$

$$\begin{aligned}\mathbf{u}_c(r,\beta,t) =& \left[\frac{\frac{K}{r}\left(\frac{\partial v_c}{\partial r}+r\frac{\partial^2 v_c}{\partial^2 r}\right)-K\frac{v_c}{r^2}-\frac{C_d v_c^2}{h}\sqrt{1+\alpha_M^2}}{\frac{\partial v_c}{\partial r}+\frac{v_c}{r}+f}\right] \\ &\cdot(\cos\beta\cdot\mathbf{e}+\sin\beta\cdot\mathbf{n})\end{aligned} \tag{5.5}$$

where $\mathbf{v}_c$ = the tangential component of the velocity field, $\mathbf{u}_c$ = the radial component of the velocity field, B is the Holland number; (r,β) are the polar coordinates of a reference system centered at the eye of the hurricane, where $\beta = 0$ when r points in the positive direction of $\mathbf{e}$; $r' = r/r_M$; and v_M is the maximum tangential velocity which is estimated as:

$$v_M(t) = \sqrt{\frac{\lambda B\Delta p(t)}{e\rho_a}} \tag{5.6}$$

with ρ_a the air density, λ the coefficient defined by $(1+\alpha_M)^{-1}$, $\alpha_M = 0.364$, and the coefficient a estimated from:

$$a = f\cdot\frac{r_M}{2v_M} \tag{5.7}$$

where f is the Coriolis parameter, $C_d(\sim 0.0015)$ = the drag coefficient, and K = the diffusion coefficient. Based on Eq. (5.4), the wind field vector $\mathbf{v}_s$ at (r,β) for time t is defined as:

$$\mathbf{v}_s(r,\beta,t) = \mathbf{v}_c(r,\beta,t)+\mathbf{u}_c(r,\beta,t)+\exp\left(-\frac{r}{r_G}\right)\cdot\mathbf{c} \tag{5.8}$$

where $r_G(\sim 500\text{km})$ is the environmental length scale defining the extend to which $\mathbf{c}$ decays in the radial direction. Based on the above definitions, the hourly-mean wind speed at a

location and height of interest can be estimated through the following transformation:

$$v_H(t) = 0.1171 \ln\left(\frac{H}{z_0}\right)\left(\frac{z_0}{0.03}\right)^{0.0706} ||\mathbf{v}_s\left(||\mathbf{r}_s||, \beta_s, t\right)|| \tag{5.9}$$

where H = the height of interest height (e.g. building height), z_0 = terrain roughness length at the site of interest, 0.1171 is a coefficient to account for the difference in measurement conditions (e.g. different reference heights and terrain roughness lengths) in wind speed transformation, and β_s is the angle in polar coordinates of the site of interest.

As the hurricane moves along its track, the wind speed, $v_H(t)$, continuously varies due to variations in the wind velocity field and relative position of the hurricane center to the site of interest. The corresponding time varying wind direction, $\alpha_H(t)$, at the site of interest can be determined from $\mathbf{v}_s(||\mathbf{r}_s||, \beta_s, t)$ estimated for the current wind velocity field.

5.3.1.3 Filling-rate model

Once hurricanes make landfall, the center pressure difference (Δp) will in general decay resulting in a reduction in the wind field and hence the wind speed at the site of interest. To simulate this phenomenon, the following filling-rate model proposed in (*Vickery and Twisdale*, 1995b) is adopted:

$$\Delta p(t) = \exp\left(-a_f t\right)\Delta p_0 \tag{5.10}$$

where an exponential decay is used to model the dissipation of the hurricane center pressure deficit once landfall in made. To include uncertainties in the decay rate, the following probabilistic filling constant a_f, dependent on the initial central pressure difference Δp_0, is considered:

$$a_f = a_0 + a_1 \Delta p_0 + \epsilon_f \tag{5.11}$$

where ϵ_f is a zero mean normally distributed error term with standard deviation σ_ϵ while the parameters a_1, a_2 are site specific and model the expected decay. Suggested values for various locations for a_1, a_2, and σ_ϵ can be found in (*Vickery and Twisdale*, 1995b). The

parameters a_0, a_1, and ϵ_f are also included in the hurricane input parameter vector Θ.

5.3.1.4 Precipitation model

To model the concurrent rainfall, the IPET (Interagency Performance Evaluation Task) parametric precipitation model, developed based on the National Aeronautics and Space Administration's Tropical Rainfall Measuring Mission database, is adopted. Comparative studies have suggested this models is superior to other commonly used parametric rainfall models (*Lonfat et al.*, 2004; *Brackins and Kalyanapu*, 2020). From the IPET model, the evolution of the mean hourly horizontal rainfall $R_h(t)$ can be estimated at the site of interest directly from the hurricane parameters $\Delta p(t)$, $r_s(t)$ and r_M at any given time t through the following expression:

$$R_h(t) = \begin{cases} 1.14 + 0.12\Delta p(t); & r_s(t) \leq r_M \\ (1.14 + 0.12\Delta p(t)) \exp\left(-0.3\left(\frac{r_s(t) - r_M}{r_M}\right)\right); & r_s(t) > r_M \end{cases} \tag{5.12}$$

where Δp is in millibars, R_h is in h/mm, and $r_s(t)$ and r_M are in kilometers. The value calculated by Eq. (5.12) provides the symmetric component of the rainfall field. To estimate the asymmetric component, $R_h(t)$ can be multiplied by a factor of 1.5 if the site of interest is in the northern hemisphere and to the right of the hurricane track (0.5 if it is to the left).

5.3.2 Hazard curve

The intensity of each hurricane is measured through the maximum hourly-mean wind speed $\bar{v}_H$ to occur at the site of interest at height H during the passage of a hurricane. The choice of $\bar{v}_H$ as an intensity measure is convenient as it allows direct comparison between performance assessments carried out using a nominal or full hurricane representation. As will be outlined in Sec. 5.7, it also allows for the definition of a conditional stochastic simulation strategy that enables the efficient estimation of failure rates associated with rare events.

Following this definition, the performance assessment of envelope systems through Eq.

(5.2) relies on an accurate estimation of the hazard curve $\lambda(\bar{v}_H)$. In particular, unlike the nominal case where $\bar{v}_H$ is treated as an independent random variable to be characterized alongside wind direction, $\bar{v}_H$ is dependent on the hurricane track input parameters Θ. In other words, the probability density function (PDF) of $\bar{v}_H$ takes the form:

$$f_{\hat{v}_H}(\bar{v}_H) = \int_{\Theta} f_{\bar{v}_H|\Theta}(\bar{v}_H|\Theta) f_{\Theta}(\Theta) d\Theta \tag{5.13}$$

where the components of Θ are the initial central pressure difference Δp_0, translation speed c, size of the hurricane r_M, approach angle θ, shortest distance d_{min} between site of interest and hurricane track, and the coefficients a_0, a_1 and ϵ_f of the filling-rate model, $f_{\hat{v}_H}$ = the PDF of $\hat{v}_H$, $f_{\bar{v}_H|\Theta}$ = the PDF of $\hat{v}_H$ conditional on Θ, and f_{Θ} = the joint PDF of the components of Θ. From $f_{\hat{v}_H}(\bar{v}_H)$, the hazard curve is defined as:

$$\lambda(\bar{v}_H) = \lambda_e \int_{\bar{v}_H}^{+\infty} f_{\hat{v}_H}(v) dv \tag{5.14}$$

where λ_e is the mean annual recurrence rate of hurricanes at the site of interest.

5.4 Response analysis: envelope actions

5.4.1 Non-stationary/-straight/-Gaussian external pressure

The simulation model for generating realizations of non-stationary, non-straight, and non-Gaussian wind pressure processes during the hurricane evolution is developed based on a stationary and straight but non-Gaussian wind pressure simulation framework proposed in (*Ouyang and Spence*, 2020).

5.4.1.1 Overview

Base on the straight and stationary wind pressure simulation model outlined in (*Ouyang and Spence*, 2020), a non-stationary/-straight wind pressure model is developed to capture

the effects on the aerodynamic pressures of the continuously varying wind speed and direction associated with full hurricanes. The main steps of the model are outlined in the conceptual flowchart of Fig. 5.1. The model is calibrated to data in the form of model-scale surface pressure coefficients $\mathbf{C}_{p,e,M}(t_M)$, with t_M = model-scale time, collected in wind tunnel pressure tests where stationary/straight but non-Gaussian pressures are measured at a grid of pressure sensors on the model surface for a discrete set of wind directions (e.g. $\{10°, 20°, ..., 350°\}$). To reconcile the discrete wind directions of the wind tunnel data with continuously varying wind directions of the storm track, these last are transformed into a piece-wise discrete representation, as illustrated in step (I) of Fig. 5.1, where a set of segments with constant wind directions are defined. In step (II), the model-scale stationary/straight but non-Gaussian wind pressure coefficient processes $\mathbf{C}^{(i)}_{p,e,M}(t_M)$ are generated for each segment and all the sensor grid locations through the straight/stationary but non-Gaussian models outlined in (*Ouyang and Spence*, 2020). In step (III) the continuous wind directions are approximated through a piece-wise linear representation to which the segments of straight/stationary and non-Gaussian pressures are merged therefore leading to a non-stationary/-straight/-Gaussian representation of the pressure coefficient processes $\mathbf{C}_{p,e,M}(t_M)$ for the full hurricane event at model-scale. Finally, $\mathbf{C}_{p,e,M}(t_M)$ is mapped back to the building-scale time in step (IV) and translated to the non-stationary/-straight/-Gaussian process $\mathbf{P}_n(t)$ in step (V). More details on each step are provided in the next section.

5.4.1.2 Procedure

In the following, further details of each step of the model outlined in Fig. 5.1 are provided.

Step I The continuous wind direction history $\alpha_H(t)$ is first discretized into a set of segments with each segment representing a straight wind event. This discretization can be expressed through the following formula:

$$\bar{\alpha}_H(t) = \text{nint}\left(\frac{\alpha_H(t)}{\Delta\alpha}\right)\Delta\alpha \tag{5.15}$$

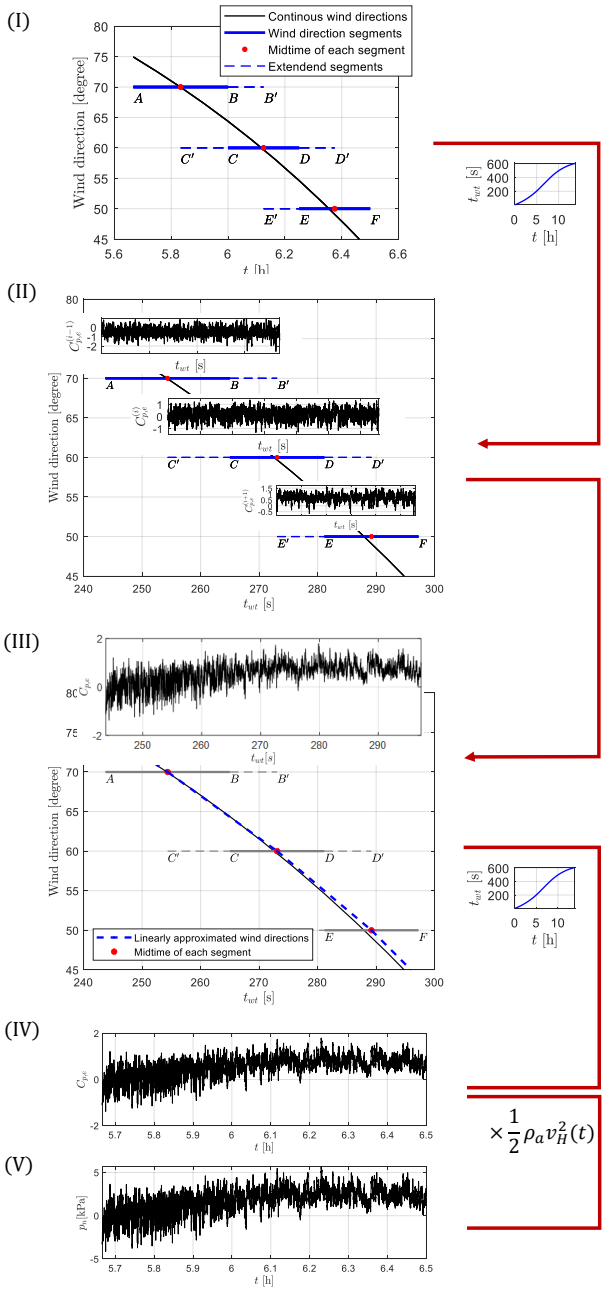

Figure 5.1: Conceptual flowchart of the non-stationary/-straight/-Gaussian wind pressure simulation model.

where $\bar{\alpha}_H(t)$ is the discretized wind direction history, nint is the function which returns a number rounded to the nearest integer, $\Delta\alpha$ is the direction step size of the wind tunnel tunnel data (e.g. $\Delta\alpha = 10°$). Each segment $\bar{\alpha}_H^{(i)}(t)$ represents a straight wind event, where $i \in \{1, 2, ..., N_{seg}\}$ with N_{seg} the total number of segments in $\bar{\alpha}_H(t)$. Within the segment $\bar{\alpha}_H^{(i)}(t)$, the mid-time is denoted by $T_m^{(i)}$ (e.g. the red dots in Fig. 5.1 with the start and end time denoted by $T_s^{(i)}$ and $T_e^{(i)}$. To form the transition region, each segment is further extended on both ends up to the mid-times of the nearby segments (e.g. the ith segment is extended to $T_m^{(i-1)}$ and $T_m^{(i+1)}$ with the boundary cases of $i = 1$ and $i = N_{seg}$ treated by only extending one end).

Step II The wind pressure coefficient processes $\mathbf{C}_{p,e,M}^{(i)}(t_M)$ are generated for each extended segment at the model-scale, where t_M is the tunnel-scale time. To obtain the total duration of each extended segment at model-scale, the following nonlinear time-scale mapping from t to t_M is derived base on Strouhal number matching:

$$t_M(t) = \frac{\gamma_H}{\bar{v}_M} \int_0^t \bar{v}_H(u)du \tag{5.16}$$

with γ_H = the ratio of model to full scale height, $\bar{v}_M$ = the mean wind speed used in the wind tunnel during the tests. Based on Eq. (5.16), the duration of the ith extended segment can be calculated through:

$$T_{seg}^{(i)} = \begin{cases} t_M(T_m^{(i+1)}) - t_M(T_s^{(i)}) \text{ if } i = 1 \\ t_M(T_e^{(i)}) - t_M(T_m^{(i-1)}) \text{ if } i = N_{seg} \\ t_M(T_m^{(i+1)}) - t_M(T_m^{(i-1)}) \text{ otherwise} \end{cases} \tag{5.17}$$

with $T_{seg}^{(i)}$ the duration of the ith extended segment.

Through Eq. (5.17), the duration of each extended segment is calculated and used to simulate the stationary/straight but non-Gaussian wind pressure coefficient processes $\mathbf{C}_{p,e,M}^{(i)}(t_M)$

through the models outlined in (*Ouyang and Spence*, 2020). The maximum sampling frequency (dictated by the wind tunnel data) should be chosen in generating $\mathbf{C}^{(i)}_{p,e,M}(t_M)$ to minimize any interpolation errors in Step (V).

Step III From the stationary wind pressure coefficient processes $\mathbf{C}^{(i)}_{p,e,M}(t_M)$ of step (II), a filter-based transition model is introduced to merge the segments into the non-stationary/-straight/-Gaussian wind pressure coefficient processes $\mathbf{C}_{p,e,M}(t_M)$. To implement the transition, the stationary processes $\mathbf{C}^{(i)}_{p,e,M}(t_M)$ are decomposed into a time-averaged component $\overline{\mathbf{C}}^{(i)}_{p,e,M}(t_M)$ and a fluctuation component $\widetilde{\mathbf{C}}^{(i)}_{p,e,M}(t_M)$ as:

$$\mathbf{C}^{(i)}_{p,e,M}(t_M) = \overline{\mathbf{C}}^{(i)}_{p,e,M}(t_M) + \widetilde{C}^{(i)}_{p,e,M}(t_M) \tag{5.18}$$

where $\overline{\mathbf{C}}^{(i)}_{p,e,M}(t_M)$ = the mean (time-averaged sense) of $\mathbf{C}^{(i)}_{p,e,M}(t_M)$. The following linear ramping-based filter is then applied to each time-averaged component:

$$\psi^{(i)}_{C_{p,e}}(t_M) = \begin{cases} \dfrac{t_M - T^{(i)}_{M,m}}{T^{(i+1)}_{M,m} - T^{(i)}_{M,m}} \text{ if } t_M > T^{(i)}_{M,m} \\ \dfrac{T^{(i)}_{M,m} - t_M}{T^{(i)}_{M,m} - T^{(i-1)}_{M,m}} \text{ if } t_M \leq T^{(i)}_{M,m} \end{cases} \tag{5.19}$$

where $T^{(i)}_{M,m}$ is the mid-time of the ith segment at model-scale time. Based on this linear filter, the merged time-averaged components with $t_M \in [T^{(i)}_{M,m}, T^{(i+1)}_{M,m}]$ is defined as:

$$\overline{\mathbf{C}}_{p,e,M}(t_M) = \psi^{(i)}_{C_{p,e,M}}(t_M)\overline{\mathbf{C}}^{(i)}_{p,e,M}(t_M) + \psi^{(i+1)}_{C_{p,e,M}}(t_M)\overline{\mathbf{C}}^{(i+1)}_{p,e,M}(t_M) \tag{5.20}$$

To merge the fluctuation components, $\widetilde{C}^{(i)}_{p,e,M}(t_M)$, a nonlinear ramping-based filter in the form of the square root of $\psi^{(i)}_{C_{p,e,M}}$ is applied with $t_M \in [T^{(i)}_{M,m}, T^{(i+1)}_{M,m}]$ as follows:

$$\widetilde{\mathbf{C}}_{p,e,M}(t_M) = \sqrt{\psi^{(i)}_{C_{p,e}}(t_M)}\widetilde{\mathbf{C}}^{(i)}_{p,e,M}(t_M) + \sqrt{\psi^{(i+1)}_{C_{p,e}}(t_M)}\widetilde{\mathbf{C}}^{(i+1)}_{p,e,M}(t_M) \tag{5.21}$$

where the complete $\bar{\mathbf{C}}_{p,e,M}(t_M)$ and $\widetilde{\mathbf{C}}_{p,e,M}(t_M)$ can be computed through iterating over all segments with special boundary consideration for $i = 1$ and $i = N_{seq}$. The non-stationary/-straight/-Gaussian wind pressure coefficient process is then obtained as:

$$\mathbf{C}_{p,e,M}(t_M) = \overline{\mathbf{C}}_{p,e,M}(t_M) + \widetilde{\mathbf{C}}_{p,e,M}(t_M) \tag{5.22}$$

Through the transition model outlined above, the merged wind pressure process will have second order statistics (auto- and cross-correlation functions) that vary following a nearly linear relationship between the wind directions in which wind tunnel data is available. Inherent to this transition model is the capture of non-Gaussianity in $\mathbf{C}_{p,e,M}(t_M)$ that matches those observed in the wind tunnel for the discrete wind directions at which wind tunnel tests were performed.

Step IV To generate the wind pressure process at building-scale with a target constant sampling frequency, the model-scale wind pressure coefficient processes need to be sampled with a non-uniform sampling frequency due to the continuously varying wind speed $v_H(t)$. This non-uniform sampling is achieved through a model-scale interpolation scheme, where the uniform time samples t_l, with $l \in \{1, 2, ..., N_l\}$ and N_l the total number of uniform samples at building-scale, are mapped to the model-scale through Eq. (5.16). This leads to a non-uniform space of model scale time samples $t_M(t_l)$ that are evaluated through interpolation. The discrete representation of the building-scale non-stationary/-straight/-Gaussian pressure coefficient processes $\mathbf{C}_{p,e}(t_l)$ is defined as:

$$\mathbf{C}_{p,e}(t_l) = \mathbf{C}_{p,e,M}(t_M(t_l)) \tag{5.23}$$

Step V From the pressure coefficient processes of Eq. (5.23), the non-stationary/-straight/-Gaussian external pressures can be estimated as:

$$\mathbf{p}_e(t_l) = \frac{1}{2}\rho_a {v_H}^2(t_l)\mathbf{C}_{p,e}(t_l) \tag{5.24}$$

where $\mathbf{p}_e$ is the vector of the non-stationary/-straight/-Gaussian pressure processes at the sensor grid locations at full scale. To estimate the pressure processes at a location, identified by the coordinate ξ_{xyz}, on the building envelope where direct measurements were not carried out, 2D interpolation with extrapolation can be used.

5.4.2 Wind-driven rain

The simulation of the time-dependent wind-driven rain is developed through the extension of the nominal wind-driven rain model outlined in (*Ouyang and Spence*, 2020). For the nominal hurricane, constant wind-driven rain is simulated through the 3D steady Reyolds-averaged Navier-Stokes (RANS) equations-based Eulerian Multiphase (EM) model proposed in (*Huang and Li*, 2012; *Kubilay et al.*, 2013, 2017). The implementation of this framework consists of two steps: (1) the RANS equations with a realizable k-ϵ turbulence model are solved for the steady-state wind field around the building; and (2) based on the steady-state solution from the first step, the EM model is implemented with the $k-\epsilon$ turbulence model to solve for wind-dispersed rain phases. In particular, each rain phase represents a phase flow problem for a group of raindrops with diameters in a predefined range. The solution of the EM model gives a vector of normalized specific catch ratios, $\bar{\boldsymbol{\eta}}(\xi_{xyz})$ for all rain phases at each location, ξ_{xyz}, of interest. The corresponding wind-driven rain can then be directly calculated based on the rainfall intensity R_h and the associated conditional raindrop diameter distribution.

To model the time-dependency of the wind-driven rain due to the continuously varying wind speed and direction, the specific catch ratios would need to be continuously solved in time. This poses a significant computational issue as this would in general imply the need

to solve RANS-based EM model for a sequence of wind speeds and directions for each storm track of interest. To overcome this issue, a numerical interpolation-based approach is adopted, where the specific catch ratios at each envelope point of interest, $\bar{\boldsymbol{\eta}}(\xi_{xyz})$, are pre-computed for a predetermined grid of wind directions, α_H, and wind speeds, v_H. The time-dependency of $\bar{\boldsymbol{\eta}}(\xi_{xyz}, t)$ can then be efficiently estimated through instantaneous interpolation at $\alpha_H(t)$ and $v_H(t)$. Based on this approach, the time-dependent wind-driven rain intensity at each envelope location of interest, $R_{wdr}(\xi_{xyz}, t)$, is estimated as:

$$R_{wdr}(\xi_{xyz}, t) = \Phi^T(t)\bar{\boldsymbol{\eta}}(\xi_{xyz}, t) \tag{5.25}$$

where $\Phi(t)$ is a weighting vector whose kth component is defined as:

$$\Phi_k(t) = R_h(t)\Delta d_k f_h\left(d_k | R_h(t)\right) \tag{5.26}$$

with Δd_k = the raindrop diameter range of the kth rain phase, d_k = the median raindrop diameter in the kth rain phase, and f_h = the PDF of the raindrop diameter distribution.

5.5 Response analysis: system analysis

Based on the envelope actions, demands in terms of dynamic story drifts and local net dynamic pressures can be estimated through the adoption of the models outlined in (*Ouyang and Spence*, 2020). Based on these demands, system measures, *sm*, associated with the final damage states of each vulnerable envelope component and subsequent water ingress can be evaluated. As will be briefly outlined below, the use of the models outlined in (*Ouyang and Spence*, 2020), enables not only the capture of the interdependencies between demands and damages, but also the progressive nature of wind induced damage.

5.5.1 Demands

5.5.1.1 Structural response

Based on the results reported in (*Ouyang and Spence*, 2021), the structural system is assumed to respond elastically. The dynamic response of the structural system can therefore be estimated through solving the following modal equations:

$$\ddot{q}_i(t) + 2\omega_i\zeta_i\dot{q}_i(t) + \omega_i^2 q_i(t) = Q_i^{\mathcal{N}}(t) \tag{5.27}$$

where q_i, $\dot{q}_i$ and $\ddot{q}_i$ are the displacement, velocity and acceleration associated with the ith dynamic mode; ω_i and ζ_i are the circular frequency and modal damping ratio of the ith mode, while $Q_i^{\mathcal{N}}(t)$ is the non-stationary/-straight/-Gaussian generalized force of the ith mode estimated as:

$$Q_i^{\mathcal{N}}(t) = \frac{\phi_i^T}{\phi_i^T \mathbf{M} \phi_i} \tilde{\mathbf{f}}_{\mathcal{N}}(t) \tag{5.28}$$

where ϕ_i = the ith mode shape; $\mathbf{M}$ = the structural mass matrix; and $\tilde{\mathbf{f}}_{\mathcal{N}}(t)$ is the dynamic forcing vector evaluated through integrating the non-stationary/-straight/-Gaussian pressure of Eq. (5.24).

From the solution of Eq. (5.27), the dynamic structural response can be approximated form the first N_m modes as:

$$\mathbf{x}(t) \approx \sum_{i=1}^{N_m} \phi_i q_i(t) \tag{5.29}$$

Dynamic story drift, $Dr(t)$, at any location of interest can then be directly estimated through a linear combination of the appropriate components of $\mathbf{x}(t)$.

5.5.1.2 Net dynamic pressure

The net pressure demands at an envelope location ξ_{xyz} of interest, $p_n(t, \xi_{xyz})$, are evaluated as:

$$p_n(t, \xi_{xyz}) = p_e(t, \xi_{xyz}) - p_i(t, \xi_{xyz}) \tag{5.30}$$

where $p_e(t, \xi_{xyz})$ is the external pressure estimated through the models of Sec. 5.4.1 at ξ_{xyz} while $p_i(t, \xi_{xyz})$ are the corresponding internal pressures. To estimate the dynamic internal pressures $p_i(t, \xi_{xyz})$, the interior of the building is modeled as a system of interconnected compartments. Initially, the building is considered enclosed with negligible internal pressurization. During the hurricane, openings can be created in the envelope due to component damages, which allows air to flow into or out of the building triggering dynamic internal pressures in all compartments that are connected through an internal opening. To solve the transient air flows, the internal pressure model outlined in (*Ouyang and Spence*, 2019) is adopted, in which the air velocity at each opening is described through the unsteady-isentropic form of the Bernoulli equation (*Vickery and Bloxham*, 1992; *Guha et al.*, 2011; *Yu et al.*, 2008). To treat the time dependency of V_H, the dynamic internal pressures, $p_i(t, \xi_{xyz})$, at each opening (external/internal or internal/internal) are directly estimated through solving a set of system nonlinear equations (one for each opening) derived based on the principle of mass conservation. A 4th-order Runge-Kutta scheme can be used to solve the system where, at each time step, the pressure-induced damages are iteratively updated until dynamic equilibrium is achieved.

It is important to observe that in solving for $p_i(t, \xi_{xyz})$ the current drift induced damage state of each envelope component must be considered. This couples not only the structural and pressure demands (e.g. a drift induced damage to the envelope can cause airflow, therefore, effecting the internal pressure), but also the demand and damage analysis (e.g. the occurrence of a drift or pressure induced damage state can effect internal pressures). It should also be observed that damage to the envelope is progressive in nature as it accumulates over the duration of the event.

5.5.2 System measures

5.5.2.1 Component damages

To model the damage susceptibility of the ith envelope component to N^i_{Dr} drift induced and N^i_p pressure-induced damage states, suites of N^i_{Dr} and N^i_p sequential damage thresholds are defined: $\mathbf{C}^i_p = \{C^i_{p_1} \leq C^i_{p_2} ... \leq C^i_{p_{N_p}}\}$ and $\mathbf{C}^i_{Dr} = \{C^i_{Dr_1} \leq C^i_{Dr_2} ... \leq C^i_{Dr_{N_{Dr}}}\}$. The randomness in the thresholds are modeled through corresponding suites sequential of fragility functions. At a given time step, $\hat{t}$, all the component's thresholds are compared with the current story drift demand, $Dr^i(t)$, and net pressure demand $p_n(t, \xi^i_{xyz})$, where the largest exceeded threshold defines the current pressure and/or drift induced damage state. To model potential coupling between drift and pressure induced damage states (e.g. the occurrence of a drift induced damage state could effect the capacity of the component to resist net pressure and vice versa), the thresholds of a suite of coupled damages states are probabilisticly degenerated upon the occurrence of the coupled damage state. The final damage states of each envelope component represent the system measures of interest.

5.5.2.2 Water ingress

The concurrent rainfall leads to the deposition of rainwater on the envelope. Damage to the envelope can then lead to water ingress. To estimate the volume of water ingress, the flow rate at each opening can be estimated directly from $R_{wdr}(\xi_{xyz}, t)$, estimated through the models of Sec. (5.4.2), and the steady-state water runoff solution derived in (*Ouyang and Spence*, 2019). From the flow rate at each opening, the total volume of water entering through an opening at a given time $\hat{t}$ can be estimated by integrating the flow rate from the time the opening first occurred, i.e. the time at which the damage causing the opening occurred. Through the implementation of this water ingress model, the time traces of total volume of water entering through each opening can be estimated.

5.6 Loss and consequence analysis

To translate the final damage states of each envelope component into repair costs and actions, the concept of unit loss function (ULF), as defined by the Federal Emergency Management Agency (FEMA) (*Federal Emergency Management Agency (FEMA)*, 2012b), is adopted. Specifically, the ULF defines the repair cost as a monotonically decreasing function with respect to the total number of components in a given damage state. To consider economies scale, a minimum quantity, Q_{min}, is defined as the lower limit below which economies scale do not take effect. Likewise, a maximum quantity, Q_{max}, is defined as the upper limit after which economies scale no longer occur. To include uncertainty in the loss estimation, the value given by the ULF is taken as the expected value of a lognormal random variable with assigned dispersion. Through ULFs, each envelope damage state can be converted, in a straightforward manner, to the repair (or time) cost. The evaluation of the of the total system level repair cost, i.e. the decision variable (dv), can then be evaluated by simply summing all envelope component repair costs. This scheme can also be used to estimate downtimes associated with repair actions. Similarly, the system-level consequence of envelope damage related to total volume of water ingress can be assessed by simply adding the volumes of water ingress at each damaged envelope component.

5.7 Simulation strategy

The evaluation of the envelope system performance relies on the possibility of efficiently solving Eq. (5.2). Because the failure rates of interest to this work are small, i.e. related to rare events, and the models used to characterize performance are computational intense, direct Monte Carlo (MC) methods are generally intractable. To overcome this, a conditional stochastic simulation scheme, that integrates subset simulation (*Au and Beck*, 2001), is developed. The approach is based on using the $\bar{v}_H$ as an indicator of hurricane intensity. The hazard curve is then divided into $N_{\bar{v}_H}$ mutually exclusive and collectively exhaustive

hazard intervals with each interval representing a set of sub-events of intensity measured over intervals of maximum mean hourly wind speed. The performance within each sub-event is evaluated using direct MC methods. The samples for each sub-event are generated through a hybrid simulation technique in which hurricane track samples, i.e. realizations of Θ conditional on the sub-event, are efficiently generated through Markov Chain Monte Carlo (MCMC) algorithms and combined with randomly sampled sets of model parameters (e.g. the component thresholds and modal damping ratios). Following this strategy, Eq. (5.2) is reformulated through the total probability theorem as:

$$\lambda(dv) = \lambda_e \sum_{k=1}^{N_{\bar{v}_H}} \left[\iint G(dv|sm)|dG(sm|\Theta)||dG(\Theta|E_{\bar{v}_H,k})| \right] P(E_{\bar{v}_H,k}) \tag{5.31}$$

with $E_{\bar{v}_H,k} = k$th sub-event defined as $\bar{v}_H \in [\bar{v}^L_{H,k}, \bar{v}^U_{H,k})$ with $\bar{v}^L_{H,k}$ and $\bar{v}^U_{H,k}$ the lower-and upper-bound wind speed defining the kth interval, where $\bar{v}^U_{H,k} = +\infty$ for $k = N_{\bar{v}_H}$; $P(E_{\bar{v}_H,k}) =$ the probability of a hurricane sample belonging to $E_{\bar{v}_H,k}$ (which can be directly estimated from the hazard curve); $N_{\bar{v}_H}$ is the total number of sub-events; and λ_e is the annual occurrence rate of hurricanes o engineering interest.

To evaluate Eq. (5.31) through the approach outlined above, subset simulation is first used to estimate the hazard curve, $\lambda(\bar{v}_H)$, through sampling the space of Θ while using $\bar{v}_H$ as the response of interest. In particular, it is convenient to select the lower and upper bound wind speeds for each sub-event based on the thresholds of $\bar{v}_H$ identified during the implementation of subset simulation. In this way, the number of intervals will depend on the target exceedance probability set for the lower bound of the last interval and the intermediate probability, P_s, used in calibrating the subset simulation algorithm. Furthermore, the probabilities $P(E_{\bar{v}_H,k})$ can be directly estimated from P_s. The number of samples used for each conditional failure event of the subset simulation will dictate the maximum number of samples that can be used to evaluate the term in square brackets of Eq. (5.31) through MC simulation. Therefore, the number of samples should be chosen to provide adequate resolution.

5.8 Case study

5.8.1 Building system

To illustrate the proposed framework while also studying the differences between performance assessments carried out using nominal as opposed to full hurricane hazard models, the archetype building outlined (*Ouyang and Spence*, 2020) with location downtown Miami, FL, is considered. As shown in Fig. 5.2, the building is a rectangular 45-story steel structure with a central core and symmetric X-bracing. The structural members were designed to satisfy a story drift limit of 1/400 under a nominal wind event with a 50-year mean recurrence interval (MRI). The first 10 dynamic modes were considered adequate for representing the dynamic response. The first three natural frequencies were 1.30, 1.67, and 2.70 rad/s respectively. The damageable components considered in the case study are the dual-pane laminated glazing units of size of 1.2×2 m^2. The thickness of each laminated pane is taken as 6mm. Each floor has 180 units with 60 units on the front (back) face and 30 units on the right (left) face, which results in a total of 8100 units for the entire building. To calibrate the damage model of Sec. 5.5.2.1, two drift-induced damages states (defined as hairline cracking, DS_{Dr_1}, and the glass cracking, DS_{Dr_2}) and one pressure-induced damage state $DS_{P_{60}}$ (defined as full loss of the window panes) are defined with random thresholds calibrated through the fragility functions outlined in (*Ouyang and Spence*, 2020). The properties of the fragility functions are reported in Table 5.1. The dual panes of each unit are considered to work in parallel when resisting net pressure that is modeled as equivalent net pressure over a duration of $t_{eq} = 60$ s with exponential parameter $s = 16$ (*Ouyang and Spence*, 2020).

Table 5.1: Fragility functions for each glazing unit.

State	Median	Dispersion	Mean	Std	Unit
DS_{Dr_1}	0.021	0.45	-	-	rad
DS_{Dr_2}	0.024	0.45	-	-	rad
$DS_{P_{60}}$*	-	-	5.29	0.91	kPa

*with $t_{eq} = 60$ s and $s = 16$.

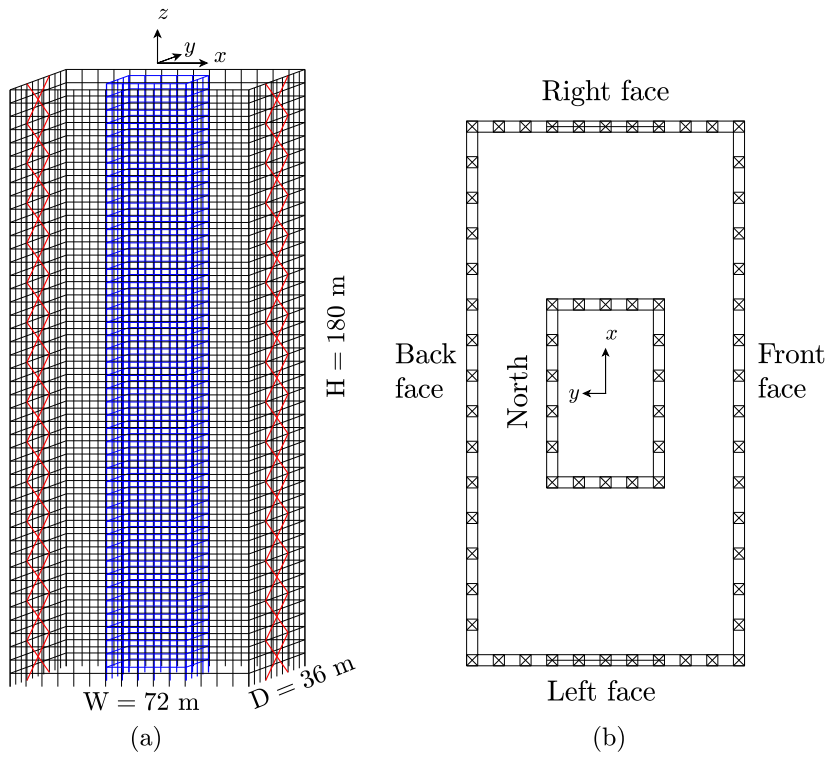

Figure 5.2: (a) Three-dimensional illustration of the 45-story structure; (b) plan view indicating the front (back), left (right) faces and North direction.

5.8.2 Hurricane hazard

To calibrate the parametric hurricane model of Sec. 5.3.1.1, and therefore the vector Θ, to downtown Miami, a subregion diameter of $R_s = 500$ km was considered while the probabilistic characteristics of the components of Θ followed the suggestions in (*Vickery and Twisdale*, 1995a). The aerodynamic model of Sec. 5.4.1.2 was calibrated to a data set of the Tokyo Polytechnic University (TPU) wind tunnel pressure database (*Tokyo Polytechnic University*, 2008). This data is used to calibrate the stationary/straight but non-Gaussian wind pressure coefficient processes $\mathbf{C}_{p,e,M}(t_M)$ at model-scale. For the data set considered, the ratio of tunnel model height to building height, γ_H, was 1/360 while the mean wind speed at model height during the wind tunnel tests was $\bar{v}_M = 11.11$ m/s. During the tests, transient pressure coefficients were simultaneously measured at 510 pressure taps located over the building surface with a constant sampling frequency of 1000 Hz and a wind direction increment of 10°. Based on $\mathbf{C}_{p,e,M}(t_M)$, the non-stationary/-straight/-Gaussian wind pressure

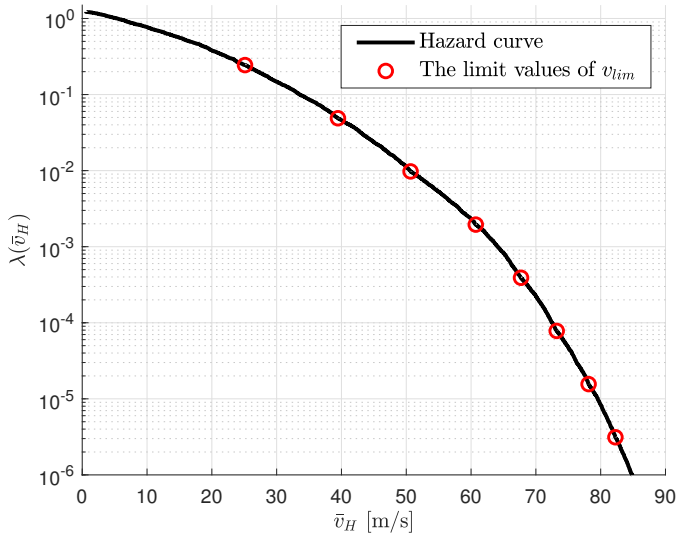

Figure 5.3: The hazard curve estimated based on the peak mean wind speed $\hat{v}_H$ at the building top.

processes $\mathbf{C}_{p,e}(t)$ were generated through the five-step procedure in Sec. 5.4.1.2.

As defined in Sec. 5.3.1.1, each sample of Θ uniquely determines a hurricane track of a full hurricane. To estimate the hazard curve through subset simulation, an intermediate probability of $P_s = 0.2$ was chosen together with $N_{\bar{v}_H} = 9$ conditional failure events. Considering how $\lambda_e = 1.22$ for Miami (*Vickery and Twisdale*, 1995a), this leads to a lower bound wind speed with an annual exceedance rate of $\lambda_e(P_s)^8 = 3.123 \times 10^{-6}$, i.e. a mean recurrence interval of over 300,000 years, which is considered adequate for evaluating the performance of the system for PBWE design scenarios. Within each subset, $N_s = 1300$ samples of Θ are considered. In running the MCMC Metropolis Hasting algorithm, a univariate normal distribution with the zero mean and standard deviation of 0.5 was considered as the proposal pdf. The choice of $N_s = 1300$ leads to $N_s(1-P_s) = 1040$ hurricane samples for for subsequent MC analysis necessary for evaluating Eq. (5.31) through the procedure of Sec. 5.7. The final hazard curve is reported in Fig. 5.3.

5.8.3 Results

5.8.3.1 Preamble

To enable the comparison between the full hurricane model of this work and a classic nominal hurricane setting, for each full hurricane sample, a nominal hurricane is also generated based on the maximum wind speed $\bar{v}_H$, with associated direction α_H, and the maximum rainfall intensity to occur over the duration of the full hurricane. For both nominal and full hurricanes, a uniform time step of $\Delta t = 0.5$ s at building-scale is used.

5.8.3.2 Discussion on a single event

To illustrate and discuss the evolution damage during a full hurricane event, a single hurricane event is analyzed in detail in this section. The event corresponds to a category V hurricane, as defined by the Saffir-Simpson hurricane wind scale (*Taylor et al.*, 2010), with a maximum wind speed of $\bar{v}_H = 67.7$ m/s is. The time evolution of hourly-averaged wind speed $\bar{v}_H(t)$, wind direction $\alpha_H(t)$ (measured clockwise from north) and hourly-mean rainfall intensity $R_h(t)$ is reported in Fig. 5.4. An example of the corresponding non-stationary/-straight/-Gaussian wind pressure simulated through the procedure of Sec. 5.4.1 is shown in Fig. 5.5 for an envelope component located at the upper-left corner of the front face of the building.

Figure 5.6 report the accumulation of damage over the duration of the hurricane in terms of the total number of envelope components assuming DS_{Dr_1}, DS_{Dr_2} or $DS_{P_{60}}$. From the comparison between the damages history and the wind speed history of Fig. 5.4(a), it can be seen that most damage occurs near the time of the maximum wind speed time, i.e. during the 7th hour the hurricane event. By the end of the hurricane event, the final damage states for each envelope component were recorded, and are reported in Table 5.2 in terms of the number of damaged components on each face of the building. As can been seen, due to the continually varying wind direction, the damage is relatively evenly distributed between the faces. The distribution of final damages shows how pressure-induced damages are dominant, which is

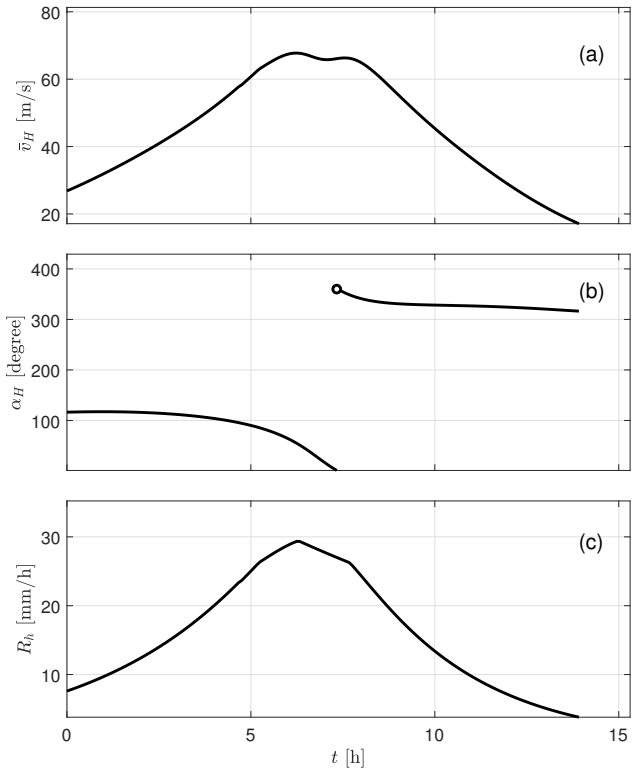

Figure 5.4: The simulated category V hurricane in Saffir-Simpson scale measured at the building site: (a) evolution of the mean hourly wind speed; (b) wind direction; and (c) mean hourly rainfall intensity.

Table 5.2: Number of envelope components assuming DS_{Dr_1}, DS_{Dr_2} or $DS_{P_{60}}$ as final damage state.

Final damage state	Front face	Right face	Back face	Left face
DS_{Dr_1}	4	3	1	3
DS_{Dr_2}	0	2	1	1
$DS_{P_{60}}$	5	12	4	11

consistent with the results reported in (*Ouyang and Spence*, 2020) for a nominal hurricane representation. Water ingress is also recorded during and at the end of the hurricane, where a total volume of 270.5 m^3 of water was estimated to enter the building through the damaged envelope components. The time histories of water ingress at each floor during the hurricane are reported in Fig. 5.7 and show how water ingress towards the bottom of the building dominates.

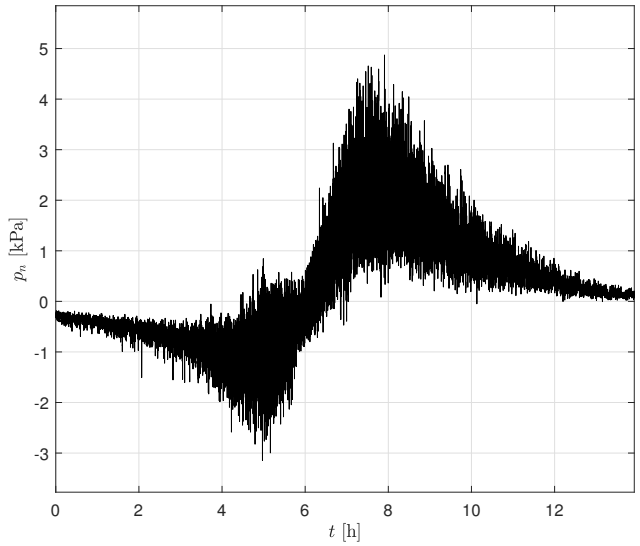

Figure 5.5: An example of the non-stationary/-straight/-Gaussian wind pressure process for an envelope component located at the upper-left corner of the front face of the building.

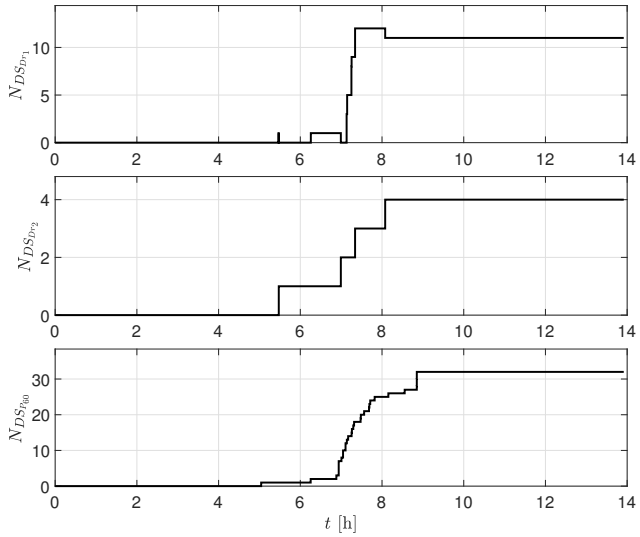

Figure 5.6: Time history of the total number of components in damage states DS_{Dr_1}, DS_{Dr_2} and $DS_{P_{60}}$.

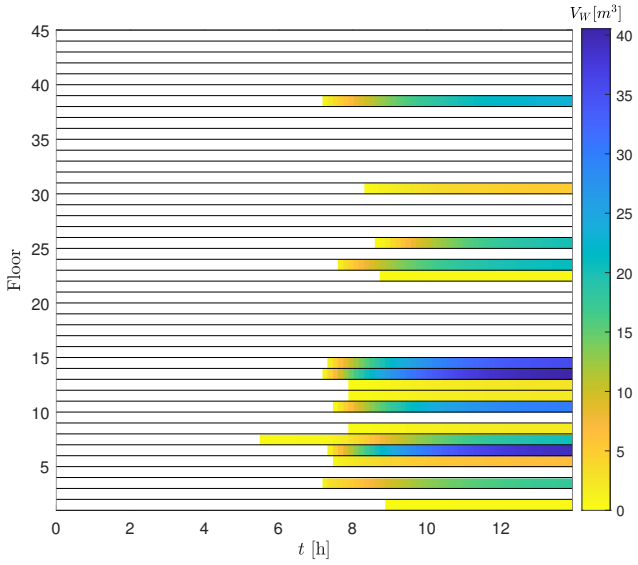

Figure 5.7: Time histories of the water ingress at each floor.

5.8.3.3 Probabilistic performance metrics

The mean annual rate of each envelope component assuming as a final damage state DS_{Dr_1}, DS_{Dr_2}, or $DS_{P_{60}}$ are reported in Fig. 5.8. The damage maps show how the drift-induced damages are uniformly distributed over the envelope except for the top and bottom floors, while the pressure-induced damages are more concentrated near the edges of the building due to the local aerodynamic response of the system. Overall, the damage patterns and rates are similar to those seen for the nominal hurricane setting analyzed in (*Ouyang and Spence*, 2020).

To evaluate the system-level envelope performance for both the nominal and full hurricanes, Fig. 5.9 reports the damage curves for both scenarios in terms of the mean annual rate of exceeding a total number of components assuming as a final damage state DS_{Dr_1}, DS_{Dr_2}, or $DS_{P_{60}}$. Comparison between the drift induced damage curves shows how the total number of damaged components are well estimated by the nominal hurricane for annual rates greater than 10^{-6}. However, for rarer events, the nominal hurricane will generally lead to considerable overestimation of damage. For pressure-induced damage, it can be seen that the nominal hurricanes underestimate the damages for mean annual rates greater than 10^{-6},

but once again significantly overestimate damages for rarer events. The differences in Fig. 5.9 are likely caused by the duration of the maximum wind T_m, where T_m is defined as duration when the hurricane wind speed $v_H(t)$ is within a certain percentage of the maximum wind speed $\bar{v}_H$ (e.g. $v_H(t) = 95\%\bar{v}_H$). Indeed, the storm track model considered in this study suggests that hurricanes with a larger maximum mean wind speed $\bar{v}_H$ have a relatively "sharper" wind speed history curve (i.e. the duration of the maximum wind is shorter).

To investigate this, the distributions of maximum wind speed duration are analyzed for all hurricane samples in hazard intervals three to nine, where the first two intervals are not considered as the value of $\bar{v}_H$ is negligible in these intervals. The mean and standard deviation of the durations are reported in Fig. 5.10. From this figure, it can be seen that as the hurricane event becomes rarer, the duration of maximum wind becomes shorter. In particular, it can be seen that wind speeds within 98% the maximum have an expected duration of around 1-hour. The capability of the nominal hurricane inadequately reproducing the damage would suggest that envelope damage is occurring essentially when wind speeds are at their maximum.

The loss curves associated with repair costs are reported in Fig. 5.11. The relative magnitude of total repair cost between the nominal and full hurricanes are similar to the damage curves of Fig. 5.9(c), which implies that the pressure-induced damages dominate the total repair cost associated with the envelope components. Figure 5.12 reports the exceedance rates associated with the consequence metric of total volume of water ingress V_W. From the comparison of the water ingress curves, the nominal hurricane significantly underestimated the total amount of water ingress as compared to the full hurricanes. Indeed, for rare events, the exceeding rates predicted by the nominal hurricane can be as much as 50 times smaller than those predicted from the full hurricane. The root of this difference can be traced back to how the nominal hurricane neglects the water that can enter the building due to rainfall after the peak wind speeds have occurred.

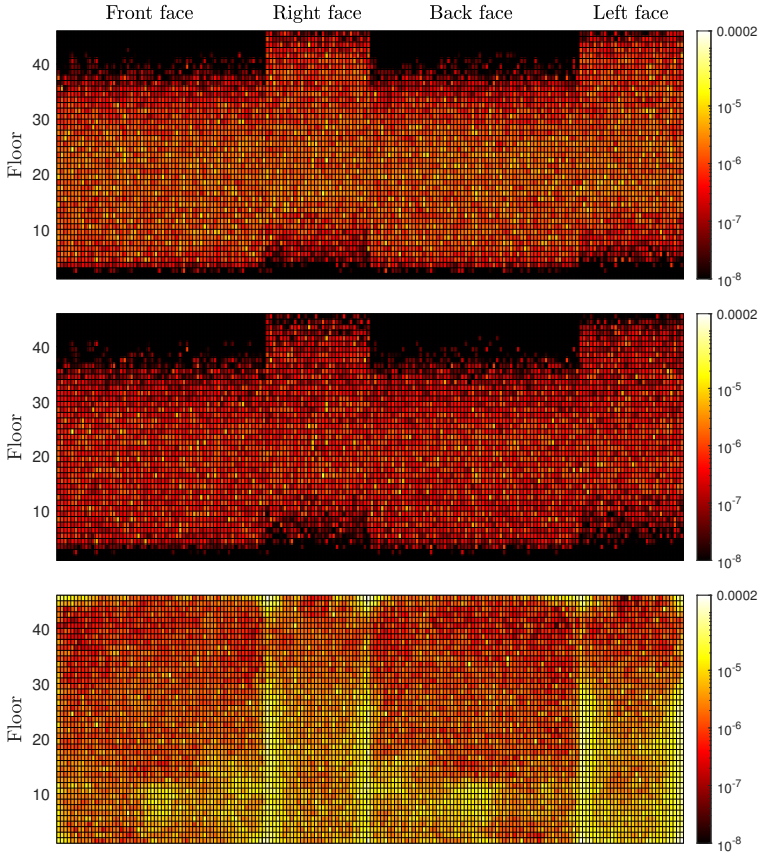

Figure 5.8: Mean annual rate of each envelope component assuming as a final damage state DS_{Dr_1}, DS_{Dr_2}, or $DS_{P_{60}}$. Top panel is associated with DS_{Dr_1}, middle panel with DS_{Dr_2}, and top panel with $DS_{P_{60}}$.

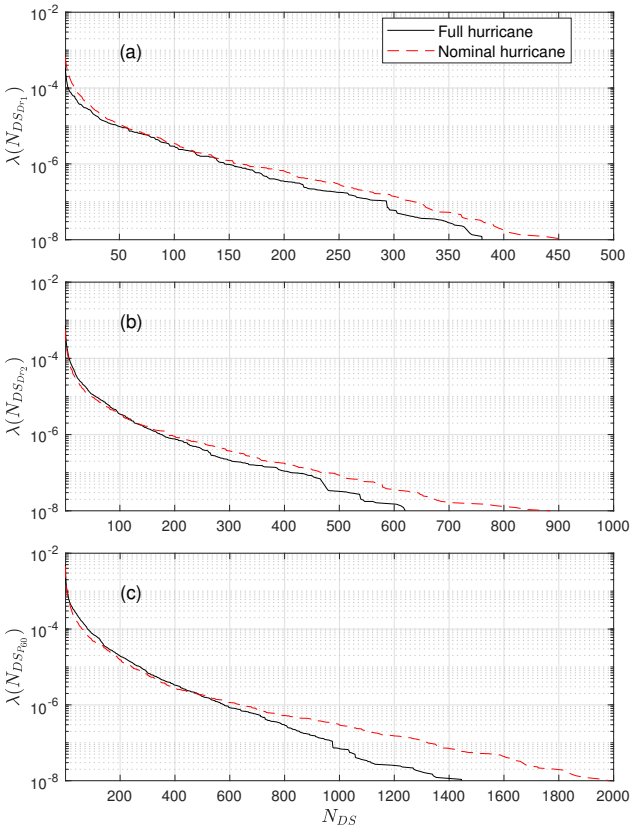

Figure 5.9: Mean annual rate of exceeding a total number of envelope components assuming as a final damage state: (a) DS_{Dr_1}; (b) DS_{Dr_2}; (c) $DS_{P_{60}}$.

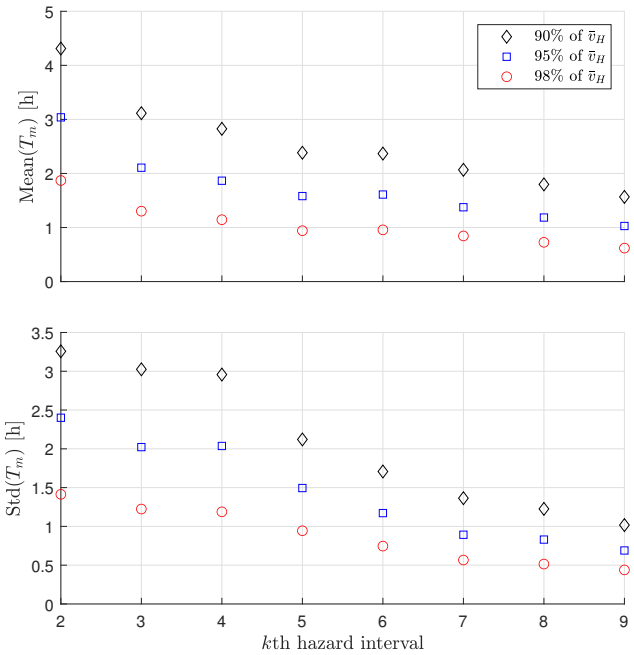

Figure 5.10: Mean and the standard deviation (Std) of T_m for hazard intensity intervals three to nine.

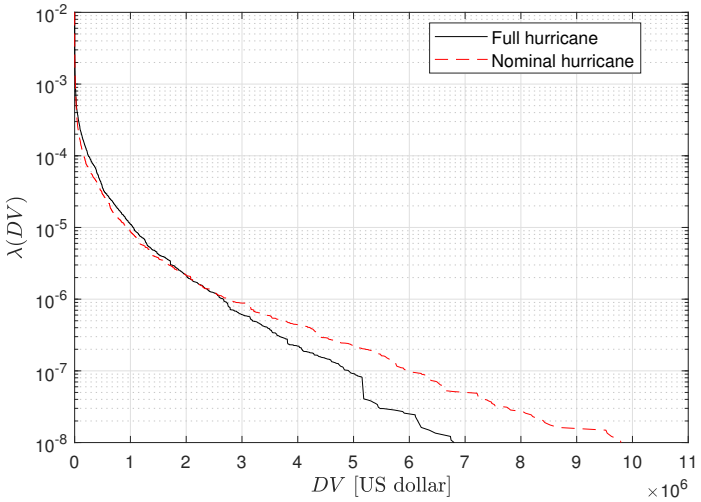

Figure 5.11: Repair cost loss curves in USD for the nominal and full hurricanes.

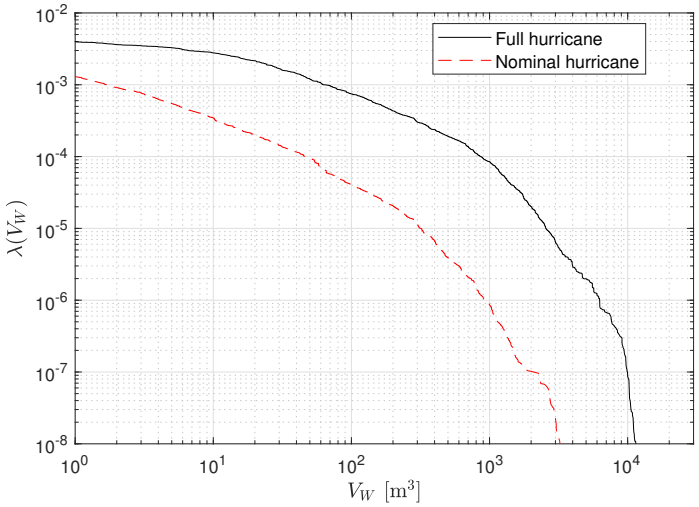

Figure 5.12: Consequence curve associated with total water ingress due to envelope damage.

5.9 Summary and conclusion

A framework is outlined for the performance assessment of the envelope system of engineered buildings considering subject to a full representation of the hurricane hazard. An innovative wind-tunnel informed POD-based non-stationary/-straight/-Gaussian wind pressure stochastic simulation model is introduced to support the full hurricane event simulation. Through the development of a conditional stochastic simulation framework, efficient estimation of probabilistic metrics associated with the performance of the envelope system in rare events is made possible. The framework was illustrated through a case study consisting in a 45-story archetype building located in downtown Miami, FL. Performance metrics associated with the total number of damaged envelope components, monetary loss, and total water ingress were evaluated. The comparison of the performance metrics with those estimated for a classic nominal representation of the hurricane hazard showed that performance assessments made with the nominal hurricane representation will generate similar amounts of damages and losses for a mean annual rate greater than 10^{-6}. For events with smaller rates than 10^{-6}, the nominal hurricanes significantly overestimated (up to 50%) the damages and losses. In terms of the water ingress, a full hurricane representation will generate a much larger volume of water ingress than seen for simulations using a nominal hurricane representation.

5.10 Acknowledgment

The research effort was supported in part by the National Science Foundation (NSF) under Grant No. CMMI-1562388. This support is gratefully acknowledged.

CHAPTER VI

Summary and Conclusions

6.1 Summary

This research was focused on developing computational frameworks to assess the performance of structural and envelope systems subject to wind and concurrent rainfall hazards. In this dissertation, coupled envelope damage mechanisms were studied and integrated into performance-based assessment frameworks where uncertainties in the wind and rain hazards were propagated through a set of computational models. Housed in novel stochastic simulation environments, the frameworks developed in this research allow for the probabilistic assessment of performance metrics associated with structural and envelope systems at both component and system-level within the setting of probabilistic nominal hurricane modeling. By integrating the frameworks into a full hurricane setting, higher-fidelity performance assessments of building systems can be also achieved. The following are the main contributions of this research to the rapidly growing field of performance-based wind engineering (PBWE).

6.1.1 High-fidelity modeling of envelope damages

As one of the most vulnerable parts of an engineered building system, the envelope can sustain a significant amount of damages and losses due to extreme winds. A high-fidelity estimate of envelope system performance is crucial for the determination of the potential risks associated with wind-excited building systems. To obtain accurate performance evalu-

ation of engineered buildings, a fragility based damage model was introduced in this thesis considering the unavoidable coupling between the demands of dynamic story drift and local dynamic net pressure. By integrating this model with a transient internal pressure model, the progressive nature of envelope damage is captured. This advancement enable far more rigorous evaluations of damage to envelope systems of engineered buildings during extreme wind events.

6.1.2 Holistic risk assessment of engineered building

The performance of structural and envelope systems of engineered buildings depends on various factors related to the hazard environment, system parameters, and component resistances. A holistic assessment must consider all the uncertainties in these factors. Through a data-driven approach, this research has developed frameworks based on integrating hurricane hazard analysis, system analysis, and loss analysis through a set of probabilistic and physics-based computational models. The uncertainties in the local wind and rain hazard, building system parameters, and component capacities are captured through the probabilistic models where databases of hurricane events, component fragility functions, and component loss functions are required for calibration. The developed frameworks have advanced the performance assessment of engineered buildings in PBWE towards more holistic approaches.

6.1.3 A first step towards building interior damage assessment

Most of the losses associated with building damages due to wind hazards are in the form of water ingress-induced building interior losses. Compared with the structural and envelope systems, the building interior systems have more complicated components/compositions and are more challenging to model. As an initial step towards interior damage assessment, this research has developed a water ingress framework for generating stochastic water ingress processes conditioned on the local wind/rain hazard climate and the damage evaluation of the cladding system. Based on this work, computational models to estimate risks of building

interior damages can be developed with the inputs of water ingress generated through the proposed framework under regional wind and rain hazards. Through this research, these models have also been extended to low-rise buildings subject to hurricanes (*Abdelhady et al.*, 2021).

6.2 Conclusions

The high fidelity modeling of envelope damages is a complex phenomena to model as they depend on the interdependent dynamic structural and external/internal pressure responses. This challenge can be overcome through the computational-based approaches proposed in this thesis.

As a consequence of the envelope damages and wind-driven rain, the water ingress into the building can be simulated through the proposed CFD-based computational framework. This framework provides detailed information on the time evaluation of water ingress into each damaged component. The inclusion of high fidelity nonlinear structural models have shown that nonlinear structural responses will in general increase the envelope damages, but not in a dramatic way. Due to the relative insensitivity of envelope damages to structural damage, the adoption of linear modal dynamic analysis instead of high-fidelity nonlinear structural analysis in estimating story drift demands is justifiable if computational efficiency is required.

Separate frameworks based on nominal hurricane (winds schematized as stationary and straight with 1-hour duration) and full hurricane (winds that follow the full non-stationary/-straight evolution of the storm) representations are developed, where a carefully calibrated case study has shown that nominal hurricanes give a less conservative estimation of component damages and losses for mean recurrence intervals (MRIs) under 10^6 years. However, over conservative estimates of damages and losses were predicted by the nominal hurricanes for MRIs greater than 10^6 years. Due to the dependency on hurricane duration, the total amount of water ingress estimated using nominal hurricanes is generally over an order of

magnitude smaller than that estimated using full hurricanes. To make the water ingress estimated from nominal hurricanes acceptable as the input for further building interior risk assessment, modification factors, dependent on the target MRI, need to be developed so that the estimates of water ingress are consistent with those of full hurricanes.

6.3 Future work

With the aim of defining a fully holistic assessment of engineered buildings subject to wind hazards, several extensions to the frameworks proposed in this research would be necessary. These extensions would require the following research directions to be pursued.

6.3.1 Performance-based assessment of building envelopes subjected to debris hazards

Debris missiles can be an important source of risks for envelope damage. Since three-dimensional modeling of debris trajectories is computationally challenging, efficient numerical models capable of generating thousands of debris objects require development. Unlike existing debris models, these new models need to be developed for urban environments as opposed to residential setting. Through this future research, performance-based frameworks encompassing risks from dynamic structural response, turbulent wind flow, and wind-borne debris in estimating building envelope damages and losses will be enabled.

6.3.2 Calibration of correction models for water ingress estimated from nominal hurricanes

The nominal hurricane setting is computationally efficient for estimating structural and envelope performance. It generally provides estimates of performance metrics associated with damages and losses with acceptable accuracy for typical design hurricane events, as demonstrated in Chapter 5. However, estimates of water ingress are significantly less conservative due to the much shorter event duration compared to full hurricanes. To improve frameworks

based on nominal hurricanes, appropriate correction models must be developed, which are capable of amplifying the amounts of water ingress to match those generated by full hurricanes. This research is important for ensuring the practicality of the proposed water ingress framework since the computational cost of simulating full hurricane events is around 10-50 times higher than that associated with nominal hurricane events.

6.3.3 Performance-based assessment of interior building systems subject to hurricanes

With frameworks for risk assessment of the structural and envelope systems developed, the next step of the research for the performance-based assessment of engineered buildings should be towards estimating the performance of the building interiors. As a significant portion of the losses incurred from hurricane hazards are associated with building interior systems, the development of models to estimate interior damages by water ingress is an indispensable part of a complete performance analysis of engineered buildings. To enable research in this direction, water drainage models and fragility databases for interior components should first be developed. This would allow damage risks associated with various types of interior components to be estimated based on the simulated demand of rainwater deposition depth. Through research of this type, the total losses sustained by the entire building system when subject to hurricane hazards would be evaluated.

BIBLIOGRAPHY

Abdelhady, A. U., D. Xu, Z. Ouyang, S. M. J. Spence, J. McCormick, and V. Y. Ivanov (2021), A framework for the estimation of water ingress due to hurricane rainfall, *Draft manuscript prepared for submission*.

American Institute of Steel Construction (2010), *Specification for Structural Steel Buildings*, Chicago, IL.

American Society of Civil Engineers (2016), *Minimum design loads and associated criteria for buildings and other structures (ASCE 7-16)*, Reston, VA.

American Society of Civil Engineers (2019), *Prestandard for Performance-Based Wind Design*, Reston, VA.

Arabzadeh, H., and K. Galal (2017), Seismic collapse risk assessment and FRP retrofitting of RC coupled C-shaped core walls using the FEMAP695 methodology, *Journal of Structural Engineering*, *143*(9).

ASCE 7-16 (2016), *Minimum Design Loads for Buildings and Other Structures*, American Society of Civil Engineers (ASCE), Reston, VA.

ASTM E1300-16 (2016), *Standard Practice for Determining Load Resistance of Glass in Buildings*, ASTM International, 100 Barr Harbor Drive, West Conshohocken, PA 19428-2959 USA.

Au, S. K., and J. L. Beck (2001), Estimation of small failure probabilities in high dimensions by subset simulation, *Probabilistic engineering mechanics*, *16*(4), 263–277.

Baheru, T., A. G. Chowdhury, G. Bitsuamlak, F. J. Masters, and A. Tokay (2014a), Simulation of wind-driven rain associated with tropical storms and hurricanes using the 12-fan wall of wind, *Building and Environment*, *76*, 18–29.

Baheru, T., A. G. Chowdhury, J. Pinelli, and G. Bitsuamlak (2014b), Distribution of wind-driven rain deposition on low-rise buildings: Direct impinging rain drops versus surface runoff, *Journal of Wind and Engineering and Industrial Aerodynamics*, *133*, 27–38.

Baheru, T., A. G. Chowdhury, and J. Pinelli (2015), Estimation of wind-driven rain intrusion through building envelope defects and breaches during tropical cyclones, *Natural Hazards Review*, *16*(2), 04014,023.

Barbato, M., F. Petrini, V. U. Unnikrishnan, and M. Ciampoli (2013), Performance-based hurricane engineering (PBHE) framework, *Structural Safety*, *45*, 24–35.

Bartlett, F. M., R. J. Dexter, M. D. Graeser, J. J. Jelinek, B. J. Schmidt, and T. V. Galambos (2003), Updating standard shape material properties database for design and reliability, *Engineering Journal, American Institute of Steel Construction*, *40*(1), 2–14.

Bashor, R., T. Kijewski-Correa, and A. Kareem (2005), On the wind-induced response of tall buildings: the effect of uncertainties in dynamic properties and human comfort thresholds, in *Proceedings of Americas Conference on Wind Engineering, Baton Rouge, LA*, vol. 31.

Bazzurro, P., C. A. Cornell, N. Shome, and J. E. Carballo (1998), Three proposals for characterizing MDOF non-linear seismic response, *Journal of Structural Engineering*, *124*(11), 1281–1289.

Beason, W., and J. Morgan (1984), Glass failure prediction model, *Journal of Structural Engineering*, *110*(2), 197–212, doi:10.1061/(ASCE)0733-9445(1984)110:2(197).

Beers, P. E. (2011), Wind risk assessments for cladding and glazing in critical facilities, in *Structures Congress 2011*, edited by D. Ames, T. L. Droessler, and M. Hoit, pp. 1606–1617, April 14-16, Las Vegas, Nevada, United States.

Behr, R. A., and J. E. Minor (1994), A survey of glazing system behavior in multi-story buildings during hurricane andrew, *The Structural Design of Tall Buildings*, *3*(3), 143–161.

Behr, R. A., M. J. Karson, and J. E. Minor (1991), Reliability analysis of window glass failure pressure data, *Structural Safety*, *11*(1), 43 –58.

Bernardini, E., S. M. J. Spence, and A. Kareem (2013), A probabilistic approach for the full response estimation of tall buildings with 3D modes using the HFFB, *Structural Safety*, *44*, 91–101.

Bernardini, E., S. M. J. Spence, D.-K. Kwon, and A. Kareem (2015), Performance-based design of high-rise buildings for occupant comfort, *Journal of Structural Engineering*, *141*(10).

Best, A. C. (1950), The size distribution of raindrops, *Quarterly Journal of the Royal Meteorological Society*, *76*(327), 16–36.

Blocken, B., and J. Carmeliet (2002), Spatial and temporal distribution of driving rain on a low-rise building, *Wind and Structures*, *5*, 441–462.

Blocken, B., and J. Carmeliet (2007), Validation of CFD simulations of wind-driven rain on a low-rise building facade, *Building and Environment*, *42*(7), 2530–2548.

Blocken, B., and J. Carmeliet (2012), A simplified numerical model for rainwater runoff on building facades: Possibilities and limitations, *Building and Environment*, *53*, 59–73.

Blocken, B., D. Derome, and J. Carmeliet (2013), Rainwater runoff from building facades: A review, *Building and Environment*, *60*, 339–361.

Brackins, J. T., and A. J. Kalyanapu (2020), Evaluation of parametric precipitation models in reproducing tropical cyclone rainfall patterns, *Journal of Hydrology*, *580*, 124,255.

Brown, W. G. (1974), *A practicable formulation for the strength of glass and its special application to large plates*, National Research Council Canada.

Bureau, U. W. (1957-1960), Rainfall intensity-frequency regime, part 2, *Tech. rep.*, Washington, D.C.

Calderone, I., and W. H. Melbourne (1993), The behaviour of glass under wind loading, *Journal of Wind Engineering and Industrial Aerodynamics*, *48*(1), 81–94.

Caracoglia, L. (2014), A stochastic model for examining along-wind loading uncertainty and intervention costs due to wind-induced damage on tall buildings, *Engineering Structures*, *78*, 121–132.

Chen, L., and C. W. Letchford (2005), Simulation of multivariate stationary gaussian stochastic processes: Hybrid spectral representation and proper orthogonal decomposition approach, *Journal of Engineering Mechanics*, *131*(8), 801–808.

Chen, X., and A. Kareem (2005), Proper orthogonal decomposition-based modeling, analysis, and simulation of dynamic wind load effects on structures, *Journal of Engineering Mechanics*, *131*(4), 325–339.

Choi, E. (1993), Simulation of wind-driven-rain around a building, *Journal of Wind Engineering and Industrial Aerodynamics*, *46*, 721–729.

Choi, E. C. C. (1994), Determination of wind-driven-rain intensity on building faces, *Journal of Wind Engineering and Industrial Aerodynamics*, *51*(1), 55–69.

Chuang, W., and S. M. J. Spence (2017), A performance-based design framework for the integrated collapse and non-collapse assessment of wind excited buildings, *Engineering Structures*, *150*, 746 – 758.

Ciampoli, M., F. Petrini, and G. Augusti (2011), Performance-based wind engineering: Towards a general procedure, *Structural Safety*, *33*(6), 367–378.

Cornell, C. A., and H. Krawinkler (2000), Progress and challenges in seismic performance assessment, *PEER Center News*, *3*(2).

Cui, W., and L. Caracoglia (2018), A unified framework for performance-based wind engineering of tall buildings in hurricane-prone regions based on lifetime intervention-cost estimation, *Structural Safety*, *73*, 75–86.

Cui, W., and L. Caracoglia (2020), Performance-based wind engineering of tall buildings examining life-cycle downtime and multisource wind damage, *Journal of Structural Engineering*, *146*(1).

Cui, W., L. Zhao, S. Cao, and Y. Ge (2021), Bayesian optimization of typhoon full-track simulation on the northwestern pacific segmented by quadtree decomposition, *Journal of Wind Engineering and Industrial Aerodynamics*, *208*, 104,428.

De Souza, R. (2000), Force-based finite element for large displacement inelastic analysis of frames, Ph.D. thesis, University of California, Berkerly.

Deodatis, G. (1996), Simulation of ergodic multivariate stochastic processes, *Journal of Engineering Mechanics*, *122*(8), 778–787.

Ding, Q., L. Zhu, and H. Xiang (2006), Simulation of stationary gaussian stochastic wind velocity field, *Wind and Structures*, *9*(3), 231–243.

Diniz, S. M. C., F. Sadek, and E. Simiu (2004), Wind speed estimation uncertainties: Effects of climatological and micrometeorological parameters, *Probabilistic Engineering Mechanics*, *19*(4), 361–371.

Dong, S., C. Jiao, and S. Tao (2017), Joint return probability analysis of wind speed and rainfall intensity in typhoon-affected sea area, *Natural Hazards*, *86*(3), 1193–1205.

Ellingwood, B. R., and P. B. Tekie (1999), Wind load statistics for probability-based structural design, *Journal of Structural Engineering*, *125*(4), 453–463.

Federal Emergency Management Agency (FEMA) (2009), *Effects of strength and stiffness degradation on seismic response*, Washington, DC.

Federal Emergency Management Agency (FEMA) (2012a), *Seismic performance assessment of buildings, Volume 1 Methodology (FEMA Publication P-58-1)*, Washington, DC.

Federal Emergency Management Agency (FEMA) (2012b), *Seismic Performance Assessment of Buildings, Volume 2 - Implementation (FEMA Publication P-58-2)*, Washington, D.C.

Federal Emergency Management Agency (FEMA) (2012b), *Seismic Performance Assessment of Buildings, Volume 1 - Methodology (FEMA Publication P-58-2)*, Washington, D.C.

Feng, C., and X. Chen (2017), Crosswind response of tall buildings with nonlinear aerodynamic damping and hysteretic restoring force character, *Journal of Wind Engineering and Industrial Aerodynamics*, *167*, 62–74.

Feng, C., and X. Chen (2018), Inelastic responses of wind-excited tall buildings: Improved estimation and understanding by statistical linearization approaches, *Engineering Structures*, *159*, 141–154.

Gavanski, E., and G. A. Kopp (2011), Storm and gust duration effects on design wind loads for glass, *Journal of Structural Engineering*, *137*(12), 1603–1610.

Geoghegan, K. M., P. Fitzpatrick, R. L. Kolar, and K. M. Dresback (2018), Evaluation of a synthetic rainfall model, p-cliper, for use in coastal flood modeling, *Natural Hazards*, *92*(2), 699–726.

Ghosn, M., L. Dueñas-Osorio, D. M. Frangopol, T. McAllister, P. Bocchini, L. Manuel, F. Biondini, S. Hernandez, and G. Tsiatas (2016), Performance indicators for structural systems and infrastructure networks, *Journal of Structural Engineering*, *142*.

Gioffrè, M., and V. Gusella (2007), Peak response of a nonlinear beam, *Journal of Engineering Mechanics*, *133*(7), 963–969.

Gioffrè, M., V. Gusella, and M. Grigoriu (2001), Non-gaussian wind pressure on prismatic buildings. I: Stochastic field, *Journal of Structural Engineering*, *127*(9), 981–989.

Grieser, J., and S. Jewson (2012), The rms tc-rain model, *Meteorologische Zeitschrift*, *21*(1), 79.

Guha, T. K., R. N. Sharma, and P. J. Richards (2011), Internal pressure dynamics of a leaky building with a dominant opening, *Journal of Wind Engineering and Industrial Aerodynamics*, *99*(11), 1151–1161.

Gunn, R., and G. D. Kinzer (1949), The terminal velocity of fall for water droplets in stagnant air, *Journal of Meteorology*, *6*(4), 243–248.

Haselton, C. B., A. B. Liel, S. T. Lange, and G. G. Deierlein (2008), Beam-column element model calibrated for predicting flexural response leading to global collapse of RC frame buildings, *Tech. Rep. 152*, Pacific Earthquake Engineering Research Center (PEER), Berkeley, CA.

Haselton, C. B., A. B. Liel, S. T. Lange, and G. G. Deierlein (2020), Calibration of model to simulate response of reinforced concrete beam-columns to collapse, *ACI Structural Journal*, *113*(6), 1141–1152.

Holmes, J. D. (2001), *Wind Loading of Structures*, 2nd ed ed., Spon Press, New York, NY.

Huang, S., and Q. Li (2010), Numerical simulations of wind-driven rain on building envelopes based on Eulerian multiphase model, *Journal of Wind Engineering and Industrial Aerodynamics*, *98*(12), 843 –857.

Huang, S. H., and Q. S. Li (2012), Large eddy simulations of wind-driven rain on tall building facades, *Journal of Structural Engineering*, *138*(8), 967–983.

Ierimonti, L., L. Caracoglia, and A. L. Materazzi (2019), Cost-based design of nonstructural elements for tall buildings under extreme wind environments, *Journal of Aerospace Engineering*, *32*(3).

Jain, A., M. Srinivasan, and G. C. Hart (2001), Performance based design extreme wind loads on a tall building, *The Structural Design of Tall Buildings*, *10*(1), 9–26.

Jakobsen, F., and H. Madsen (2004), Comparison and further development of parametric tropical cyclone models for storm surge modelling, *Journal of Wind Engineering and Industrial Aerodynamics*, *92*(5), 375–391.

Johnson, T., J. P. Pinelli, T. Baheru, A. G. Chowdhury, J. Weekes, and K. Gurley (2018), Simulation of rain penetration and associated damage in buildings within a hurricane vulnerability model, *Natrual Hazards Review*, *19*(2).

Judd, J., and F. Charney (2015), Inelastic behavior and collapse risk for buildings subjected to wind loads, in *Structures Congress 2015*, edited by N. Ingraffea and M. Libby, pp. 2483–2496, April 23-25, Portland, Oregon, USA.

Judd, J. P. (2018), Windstorm resilience of a 10-story steel frame office building, *ASCE-ASME Journal of Risk and Uncertainty in Engineering Systems, Part A: Civil Engineering*, *4*(3).

Kareem, A. (1986), Performance of cladding in hurricane alicia, *Journal of Structural Engineering*, *112*(12), 2679–2693.

Kareem, A. (2008), Numerical simulation of wind effects: A probabilistic perspective, *Journal of Wind Engineering and Industrial Aerodynamics*, *96*, 1472–1497.

Kareem, A., and R. E. Bashor (2006), Performance of glass/cladding of high-rise buildings in hurricane Katrina, *Tech. rep.*, NatHaz Modeling Laboratory, University of Notre Dame.

Kie, J. G., J. Matthiopoulos, J. Fieberg, R. A. Powell, F. Cagnacci, M. S. Mitchell, J. M. Gaillard, and P. R. Moorcroft (2010), The home-range concept: Are traditional estimators still relevant with modern telemetry technology?, *Philosophical Transactions of the Royal Society B*, *365*(1550), 2221–2231.

Kubilay, A., D. Derome, B. Blocken, and J. Carmeliet (2013), CFD simulation and validation of wind-driven rain on a building facade with an eulerian multiphase model, *Building and Environment*, *61*, 69 – 81.

Kubilay, A., D. Derome, B. Blocken, and J. Carmeliet (2014), Numerical simulations of wind-driven rain on an array of low-rise cubic buildings and validation by field measurements, *Building and Environment*, *81*, 283 –295.

Kubilay, A., D. Derome, B. Blocken, and J. Carmeliet (2015a), Numerical modeling of turbulent dispersion for wind-driven rain on building facades, *Environmental Fluid Mechanics*, *15*(1), 109–133.

Kubilay, A., D. Derome, B. Blocken, and J. Carmeliet (2015b), Wind-driven rain on two parallel wide buildings: Field measurements and CFD simulations, *Journal of Wind and Engineering and Industrial Aerodynamics*, *146*, 11–28.

Kubilay, A., J. Carmeliet, and D. Derome (2017), Computational fluid dynamics simulations of wind-driven rain on a mid-rise residential building with various types of facade details, *Journal of Building Performance Simulation*, *10*(2), 125–143.

Lin, N., J. D. Holmes, and C. W. Letchford (2007), Trajectories of wind-borne debris in horizontal winds and applications to impact testing, *Journal of Structural Engineering*, *133*(2), 274–282.

Liu, M., X. Chen, and Y. Yang (2017), Estimation of peak factor of non-gaussian wind pressures by improved moment-based hermite model, *Journal of Engineering Mechanics*, *143*(7).

Lonfat, M., F. D. Marks, and S. Chen (2004), Precipitation distribution in tropical cyclones using the tropical rainfall measuring mission (trmm) microwave imager: A global perspective, *Monthly Weather Review*, *132*(7), 1645–1660.

Lonfat, M., R. Rogers, T. Marchok, and F. D. Marks Jr (2007), A parametric model for predicting hurricane rainfall, *Monthly Weather Review*, *135*(9), 3086–3097.

McKenna, F., G. Fenves, and M. Scott (2013), Computer program OpenSees: Open system for earthquake engineering simulation, *Tech. rep.*, Pacific Earthquake Engineering Center, University of California Berkeley.

Minciarelli, F., M. Gioffrè, M. Grigoriu, and E. Simiu (2001), Estimates of extreme wind effects and wind load factors: Influence of knowledge uncertainties, *Probabilistic Engineering Mechanics*, *16*, 331–340.

Minor, J. E. (1994), Windborne debris and the building envelope, *Journal of Wind Engineering and Industrial Aerodynamics*, *53*(1-2), 207–227.

Minor, J. E. (2005), Lessons learned from failures of the building envelope in windstorms, *Journal of Architectural Engineering*, *11*(1), 10–13.

Moehle, J., and G. G. Deierlein (2004), A framework methodology for performance-based earthquake engineering, in *13th world conference on earthquake engineering*, vol. 679.

Mohammadi, A., A. Azizinamini, L. Griffis, and P. Irwin (2019), Performance assessment of an existing 47-story high-rise building under extreme wind loads, *Journal of Structural Engineering*, *145*(1).

Nagler, T. (2017), kdecopula: An r package for the kernel estimateion of bivariate copula densities.

National Institute of Standards and Technology (1980), Extreme wind speed data sets: Hurricane wind speed.

Neuenhofer, A., and F. Filippou (1998), Geometrically nonlinear flexibility-based frame finite element, *Journal of Structural Engineering*, *124*(6), 704–711.

Neuenhofer, A., and F. C. Filippou (1997), Evaluation of nonlinear frame finite-element models, *Journal of Structural Engineering*, *123*(7), 958–966.

NOAA National Centers for Environmental Information (NCEI) (2020), U.S. billion-dollar weather and climate disasters, doi:10.25921/stkw-7w73.

Ouyang, Z., and S. M. J. Spence (2019), A performance-based damage estimation framework for the building envelope of wind-excited engineered structures, *Journal of Wind Engineering and Industrial Aerodynamics*, *186*, 139–154.

Ouyang, Z., and S. M. J. Spence (2020), A performance-based wind engineering framework for envelope systems of engineered buildings subject to directional wind and rain hazards, *Journal of Structural Engineering*, *146*(5), 04020,049.

Ouyang, Z., and S. M. J. Spence (2021), Performance-based wind-induced structural and envelope damage assessment of engineered buildings through nonlinear dynamic analysis, *Journal of Wind Engineering and Industrial Aerodynamics*, *208*, 104,452.

Peng, L., G. Huang, X. Chen, and A. Kareem (2017), Simulation of multivariate nonstationary random processes: Hybrid stochastic wave and proper orthogonal decomposition approach, *Journal of Engineering Mechanics*, *143*(9).

Peng, X., D. B. Roueche, D. O. Prevatt, and K. R. Gurley (2016), An engineering-based approach to predict tornado-induced damage, in *Multi-hazard approaches to civil infrastructure engineering*, pp. 311–335, Springer.

Pereira, J. C. R., A. M. P. Jesus, J. Xavier, and A. A. Fernandes (2014), Ultra low-cycle fatigue behaviour of a structural steel, *Engineering Structures*, *60*, 214–222.

Petrini, F., A. Giaralis, and Z. Wang (2020), Optimal tuned mass-damper-inerter (TMDI) design in wind-excited tall buildings for occupants' comfort serviceability performance and energy harvesting, *Engineering Structures*, *204*(109904).

Petrini, F. and Ciampoli, M. (2012), Performance-based wind design of tall buildings, *Structure and Infrastructure Engineering*, *8*(10), 954–966.

Pita, G., J. P. Pinelli, K. Gurley, C. Subramanian, and S. Hamid (2016), Hurricane vulnerability model for mid/high-rise residential buildings, *Wind and Structures*, *23*(5), 449–464.

Pita, P. T., J. P. Pinelli, C. S., K. Gurley, J. Mitrani-Reiser, J. Weekes, and S. Hamid (2012), Assessment of hurricane-induced internal damage to low-rise buildings in the florida public hurricane loss model, *Journal of Wind Engineering and Industrial Aerodynamics*, *104-106*, 76–87.

Porter, K. A. (2003), An Overview of PEER's Performance-Based Earthquake Engineering Methodology, *Proc. Ninth International Conference on Applications of Statistics and Probability in Civil Engineering (ICASP9)*.

Quirouette, R., and B. Arch (2004), *Air pressure and the building envelope*, Citeseer.

Rappaport, E. N. (1999), Atlantic hurricane season of 1997, *Monthly Weather Review*, *127*(9), 2012–2026.

Rosowsky, D. V., and B. R. Ellingwood (2002), Performance-based engineering of wood frame housing: Fragility analysis methodology, *Journal of Structural Engineering*, *128*(1), 32–38.

Satake, N., K. Suda, T. Arakawa, A. Sasaki, and Y. Tamura (2003), Damping evaluation using full-scale data of buildings in Japan, *Journal of Structural Engineering*, *129*(4), 470–477.

Seo, D. W., and L. Caracoglia (2013), Estimating life-cycle monetary losses due to wind hazards: Fragility analysis of long-span bridges, *Engineering Structures*, *56*, 593–1606.

Shih, T. H., W. W. Liou, A. Shabbir, Z. Yang, and J. Zhu (1995), A new k-ϵ eddy viscosity model for high reynolds number turbulent flows, *Computational Fluids*, *24*, 227–238.

Shirolkar, J. S., C. F. M. Coimbra, and M. Q. McQuay (1996), Fundamental aspects of modeling turbulent particle dispersion in dilute flows, *Progress in Energy and Combustion Science*, *22*(4), 363–399.

Simiu, E., and R. H. Scanlan (1986), *Wind effects on structures : an introduction to wind engineering*, 2nd ed ed., 64 - 65 pp., New York : Wiley.

Smith, M. A., and L. Caracoglia (2011), A Monte Carlo based method for the dynamic "fragility analysis" of tall buildings under turbulent wind loading, *Engineering Structures*, *33*(2), 410–420.

Snaiki, R., and T. Wu (2018), An analytical framework for rapid estimate of rain rate during tropical cyclones, *Journal of Wind Engineering and Industrial Aerodynamics*, *174*, 50–60.

Spence, S. M. J., and A. Kareem (2013), Data-enabled design and optimization (DEDOpt): Tall steel buildings frameworks, *Computers and Structures*, *134*(12), 134–147.

Spence, S. M. J., and A. Kareem (2014a), Performance-based design and optimization of uncertain wind-excited dynamic building systems, *Engineering Structures*, *78*, 133 –144.

Spence, S. M. J., and A. Kareem (2014b), Tall buildings and damping: a concept-based data-driven model, *Journal of Structural Engineering*, *140*(5), 04014,005–1–15.

Spence, S. M. J., M. Gioffrè, and A. Kareem (2016), An efficient framework for the reliability-based design optimization of large-scale uncertain and stochastic linear systems, *Probabilistic Engineering Mechanics*, *44*, 174–182.

Suzuki, Y., and D. G. Lignos (2020), Development of collapse-consistent loading protocols for experimental testing of steel columns, *Earthquake Engineering & Structural Dynamics*, *49*, 114–131.

Tabbuso, P., S. M. J. Spence, L. Palizzolo, A. Pirrotta, and A. Kareem (2016), An efficient framework for the elasto-plastic reliability assessment of uncertain wind excited systems, *Structural Safety*, *58*, 69–78.

Taylor, H. T., B. Ward, M. Willis, and W. Zaleski (2010), The saffir-simpson hurricane wind scale, *Atmospheric Administration: Washington, DC, USA*.

Tokyo Polytechnic University (2008), TPU Wind Pressure Database.

Unnikrishnan, V. U., and M. Barbato (2016), Performance-based comparison of different storm mitigation techniques for residential buildings, *Journal of Structural Engineering*, *142*(6), https://doi.org/10.1061/(ASCE)ST.1943–541X.0001,469.

Unnikrishnan, V. U., and M. Barbato (2017), Multihazard interaction effects on the performance of low-rise wood-frame housing in hurricane-prone regions, *Journal of Structural Engineering*, *143*(8), 04017,076.

Vega, R., and R. Koke (2008), Wind effects of hurricane Ike on chase tower in downtown Houston, *Newsletter of American association for wind engineering*, pp. 7–9.

Venanzi, I., O. Lavan, L. Ierimonti, and S. Fabrizi (2018), Multihazard loss analysis of tall buildings under wind and seismic loads, *Structure and Infrastructure Engineering*, *14*(10), 1295–1311.

Vickery, B. J., and C. Bloxham (1992), Internal pressure dynamics with a dominant opening, *Journal of Wind Engineering and Industrial Aerodynamics*, *41*(1), 193– 204.

Vickery, P. J., and L. A. Twisdale (1995a), Prediction of hurricane wind speeds in the united states, *Journal of Structural Engineering*, *121*(11), 1691–1699.

Vickery, P. J., and L. A. Twisdale (1995b), Wind-field and filling models for hurricane wind-speed predictions, *Journal of Structural Engineering*, *121*(11), 1700–1709.

Vickery, P. J., P. Skerlj, A. C. Steckley, and L. A. Twisdale (2000a), Hurricane wind field model for use in hurricane simulations, *Journal of Structural Engineering*, *126*(10), 1203–1221.

Vickery, P. J., P. F. Skerlj, and L. A. Twisdale (2000b), Simulation of hurricane risk in the us using empirical track model, *Journal of structural engineering*, *126*(10), 1222–1237.

Weller, H. G., G. Tabor, H. Jasak, and C. Fureby (1998), A tensorial approach to computational continuum mechanics using object-oriented techniques, *Computers and Physics*, *12*(6), 620–631.

Wen, Y. K., and Y. J. Kang (2001), Minimum building life-cycle cost design criteria. II: applications, *Journal of Structural Engineering*, *127*(3).

Williams, T., and A. Kareem (2003), Performance of building cladding in urban environments under extreme winds, in *Proceedings of the 11th international conference on wind engineering, Lubbock*, vol. 7.

Yang, T. Y., J. Moehle, B. Stojadinovic, and A. Der Kiureghian (2009), Seismic performance evaluation of facilities: methodology and implementation, *Journal of Structural Engineering*, *135*(10), 1146–1154.

Yu, S., W. Lou, and B. Sun (2008), Wind-induced internal pressure response for structure with single windward opening and background leakage, *Journal of Zhejiang University-SCIENCE A*, *9*(3), 313–321.

Zhao, H., M. Grigoriu, and K. R. Gurley (2019), Translation processes for wind pressures on low-rise buildings, *Journal of Wind Engineering and Industrial Aerodynamics*, *184*, 405–416.

Zheng, X. W., H. N. Li, and C. Li (2019), Damage probability analysis of a high-rise building against wind excitation with recorded field data and direction effect, *Journal of Wind Engineering and Industrial Aerodynamics*, *184*, 10–22.

Zheng, X. W., H. N. Li, Y. B. Yang, G. Li, L. S. Huo, and Y. Liu (2020), Damage risk assessment of a high-rise building against multihazard of earthquake and strong wind with recorded data, *Engineering Structures*, *200*(109697).